ALMA MATER STUDIORUM
UNIVERSITÀ DEGLI STUDI DI BOLOGNA
Facoltà di Scienze Matematiche Fisiche e Naturali

Dottorato di Ricerca in Geofisica
XX Ciclo
Settore scientifico disciplinare: GEO/10

JOINT INVERSION OF GPS AND STRONG MOTION DATA FOR EARTHQUAKE RUPTURE MODELS

Ph.D. Thesis of:
Antonella Cirella

Tutor:
Dr. Alessio Piatanesi

Supervisor:
Prof.ssa Maria Elina Belardinelli

Coordinator:
Prof. Michele Dragoni

2008

a nonna Maria

Contents

Introduction

1. Kinematic modeling of seismic source
1.1. Introduction 1
1.2. Seismic source representation theory 2
1.2.1. Kinematic source model 5
1.3. Inversion methods 6
1.3.1. Simulated Annealing algorithm 9
1.4. Single-window and multi-window approaches 11
1.5. Model uncertainty 13
1.6. A new nonlinear inversion technique 14
1.6.1. Finite fault parameterization 15
1.6.2. Implementation: Source time function 16
1.6.3. Inversion procedure 19

2. Sensitivity and resolution analysis
2.1. Introduction 25
2.2. Sensitivity to velocity structure 27
2.2.1 Noise-free data 29
2.2.2 Uncertainty of the velocity structure 33
2.3. Importance of source time function 37
2.3.1 Results: Kinematic parameters 39
2.3.2 Results: *Trade-off* 43
2.3.3 Results: *Bias* 47
2.4. Discussion 50

3. Application to real earthquakes
3.1. Introduction 53
3.2. The 2000 western Tottori earthquake 55
3.2.1 Data: Processing and weighting 57
3.2.2 Fault plane geometry and crustal structure 58
3.2.3 Inversion results 59
3.3. The 2007 Niigata-ken Chuetsu-oki earthquake 64
3.3.1 Data and fault model 66
3.3.2 Synthetic test 67
3.3.3 Rupture process of the 2007 Niigata earthquake 70
3.4. Discussion 73

4. Dynamic consistency of kinematic modeling
4.1. Introduction 77
4.2. Sensitivity to parametric uncertainty 80
4.2.1 Synthetic test I: Target Model 81
4.2.2 Synthetic test I: Kinematic parameters comparison 83
4.2.3 Synthetic test I: Resolution analysis 86

4.3. Dynamically consistent source time function 89
4.3.1 Synthetic test II: Target model 90
4.3.2 Synthetic test II: Results 91
4.4. Proposals 93
4.5. Dynamically constrained kinematic inversion 94
4.5.1 Methodology 96
4.5.2 Kinematic inversion: Applications to the 2000 western Tottori earthquake 97
4.5.3 Results: Kinematic parameters and data fit 98
4.5.4 Results: Appraisal of the ensemble 101
4.6. Dynamic Modeling 103
4.7. Discussion 107

5. Ground motion modeling and radiated seismic energy
5.1. Introduction 111
5.2. Ground motion forward modeling 111
5.2.1 Computation strategy 112
5.2.2 Results: Waveforms and spectra comparison 114
5.3. Radiated seismic energy 116
5.3.1 Methodology 117
5.3.2 Results 119
5.4. Discussion 120

6. Variability of kinematic source parameters: Implications on shaking scenario
6.1. Introduction 121
6.2. Shaking scenario and kinematic source parameters 124
6.2.1 Variability of kinematic parameters 124
6.3. Strategy to predict shaking scenarios 126
6.3.1 Computation method 127
6.3.2 Geometrical setting and fault parameters 128
6.3.3 Shaking scenarios 131
6.4. Scenario selection 137
6.4.1 One ground motion parameter at one site 138
6.4.2 More ground motion parameters at one site 139
6.4.3 One ground motion parameter at more sites 140
6.5. Discussion 142

Conclusions 145

Appendix 151

References 159

Introduction

One of the principal goals of seismology is to infer the nature of earthquake source from observations of seismic ground motion.

Earthquakes occur when the rocks on opposite sides of a surface (fault plane) slip suddenly, producing a displacement discontinuity (dislocation) across the fault surface. The earthquake source can be modeled by shear rupture propagating on a pre-existing or newly created fault embedded in the Earth's crust or upper mantle. The rupture initiates quasi-statically on a small nucleation zone and then, when the friction at the rupture front drops from static to dynamic levels, it develops into an unstable phase over the fault plane. Consequently, seismic radiation is triggered after the passing of the front and the characteristics of ground motions that result from this instability are strongly affected by the geometrical and mechanic features of the faulting. The geometrical characteristics include the size, shape, depth, and orientation of the fault area that slips during the earthquake and the amount, direction, and complexity of slip. The mechanical parameters include the hypocenter (where the rupture initiates on the fault), the rupture velocity (how rapidly the rupture spreads over the fault), the rise time (how quickly the slip takes place at each point on the fault), and the slip direction (how coherently adjacent points on the fault are slipping). These parameters are function of stress (due to long-term tectonic processes) acting on the fault, physical properties of the rock surrounding the fault and strength of the fault itself. The storage and release of stress, in terms of crustal deformation, govern the different phases of the seismic cycle: the pre-seismic, co-seismic, post-seismic and inter-seismic phases. The co-seismic phase describes the rapid slip evolution on the fault plane and the associated seismic radiation, during an earthquake. Dynamic modeling of earthquake source provides a description of slip evolution related to constitutive properties and initial conditions on the fault plane. In contrast, kinematic models of seismic source (e.g., *Haskell*, 1969) describe the resulting motion (slip history) without investigating the causes of the rupture process. This means that if the displacement discontinuity across a fault is known as a time-dependent function

of position on the fault, then motions throughout the medium are completely determined (*Aki and Richards*, 1980).

The kinematic approach allows us to interpret the observable motions that radiate from the source region in terms of particle motions on a fault plane (slip history).

In the framework of elastodynamic, the ground motion resulting from an earthquake source is expressed mathematically using a representation theorem, which relates the observable motions with the dislocation occurring across the fault plane. To evaluate this basic relationship a source model that describes the slip is necessary. Direct observations are impossible, since slip takes place at depths from the surface to about 15 km or more for shallow crustal earthquakes. For this reason, much of the available information about the space-time behavior of the seismic source rupture process comes from inverting ground motion data.

With the development of the seismic observational networks and the improvement of contemporary computational tools, seismologists show a growing interest on the inversion of seismic and geodetic records for the earthquake source rupture process. Actually, many ground motion records have been inverted to image the rupture characteristic of almost all disastrous earthquakes that have occurred during the past two decades.

The inferred rupture history is the solution of an inverse geophysical problem, which is inherently no unique. This means that the source rupture model cannot be uniquely determined by observations, i.e. there are many models which explain the data equally well. Another cause of complexity is that real data contain noise (either random or systematic) which affects the information contained on the model. As well, our knowledge of the physical processes relating a model to data is often imperfect and uncertain (*Sambridge*, 2001).

Earthquake kinematic models are used as input data to some seismological applications aimed to infer the dynamic properties of the seismic sources.

Furthermore, kinematic models of the earthquakes source are also used to estimate seismically radiated energy and to predict ground motion shaking scenarios for engineering design purpose. Consequently, a robust kinematic inversion input is important for the reliability of such studies. While much efforts have been

devoted to improve the computational efficiency of different inversion algorithms, the main drawback of the kinematic inversion approach is the intrinsic difficulty to assess the resolution and to analyze the physical consistency of the obtained models. Actually, this issue is still unresolved and many authors, from different fields of geophysics and seismology, have addressed this difficult matter and have formulated partial or approximated answers.

The present work aims to contribute to this discussion, with the main objective to propose some answers to these open questions.
The core issue of this study concerns the understanding and the kinematic modeling of the coseismic rupture process of an earthquake on a finite fault, through the joint inversion of seismic and geodetic data.
Particular attention will be devoted to assess the robustness of the solutions, by focusing on the influence of some representative sources of uncertainty, characterizing the kinematic inversion modeling.
For this purpose, we will dwell on the nonuniqueness, sensitivity and resolution issues, as well as discuss the dynamic consistency of the kinematic source models. We study the reliability of the retrieved slip histories and we investigate possible dynamic constraints to apply during a kinematic inversion, in order to obtain a realistic description of the source processes.
The current work has been realized in collaboration with other researchers of Istituto Nazionale di Geofisica e Vulcanologia, Rome, Italy.

In the first chapter we give a brief review of the seismic source representation theory, devoting major attention to the kinematic source modeling. We describe the seismic source through the definition of the slip-velocity source time function (STF), which prescribes the slip-velocity evolution during rupture propagation on a fault plane, focusing on its relationships to the data. Then, we present an overview of the inversion theory, providing a synopsis of different approaches used to image the kinematic slip histories. In particular, we concentrate our interest on the assessment of the model uncertainty. Indeed, we propose a new nonlinear inversion technique to jointly invert strong motion records and geodetic

data to retrieve the rupture history of an earthquake on a finite fault. This procedure, based on a global search optimization algorithm, allows us to generate an ensemble of models that efficiently sample the good data-fitting regions of the parameter space and provides a method to extract the stable features of the inferred rupture models (appraisal of the ensemble). Further, our technique allows for the use of different slip velocity source time functions.

In the second chapter we check the resolution and robustness of our procedure by showing two different sensitivity studies, which are based on several synthetic tests. In the first study, we emphasize the effect of the uncertainty induced by the choice of crustal velocity structure on synthetic strong ground motion and GPS measurements, assuming the geometry of the 2000 western Tottori earthquake dataset. In the second study we investigate the uncertainty due to the inaccurate knowledge of the source time function. In both cases the appraisal of the model ensemble allows us to give a quantitative measure of the effects of these two important sources of uncertainty on the retrieved rupture models.

In the third chapter we stress the reliability of our inversion technique, in order to test and show its effectiveness. To this goal, we apply our method to recent earthquakes, such as the 2000 western Tottori (Mw 6.6), and the 2007 Niigata-ken Chuestu-oki (Mw 6.6), Japan, earthquakes. For these events we derive the complete rupture history by jointly inverting strong-motion seismic data and GPS records. Besides, the a posteriori ensemble inference, provides us a method to indicate which areas of the fault are well-resolved and to give an estimate of the variability of each model parameter. We compare our results with published models.

In the fourth chapter we focus our attention on the importance of adopting source time functions (STFs) compatible with earthquake dynamics to image the kinematic rupture history on a finite fault. The main objective of this study relies on the possibility to obtain kinematic inversion schemes dynamically constrained. To this purpose, first we present several synthetic tests to analyze the uncertainty due to the parameterization of kinematic source models. Then, to assess how the choice of the source time function can bias the retrieved kinematic rupture histories of real earthquakes, we perform several inversions of strong motion and

GPS data recorded during the 2000 western Tottori earthquake, by assuming different STFs. Earthquake kinematic models are often used to retrieve the main parameters of the causative dynamic rupture process. Different papers in the recent literature have emphasized that the calculation of these quantities can be biased by the kinematic parameterization. We focus our attention on the a priori assumption of the source time function. We use the inverted rupture histories as boundary conditions in dynamic rupture modeling to infer some important dynamic parameters.

In the fifth chapter we investigate the effect of the source time function on the ground motion prediction and on the estimates of the radiated seismic energy (E_r). By adopting different kinematic source models, we compute synthetic waveforms through forward modeling in the frequency band commonly used in kinematic inversion and we estimate the far field contribution to the radiated energy. We show the differences on the synthetic velocity waveforms and spectra as well as on the total E_r and on the E_r contribution at different frequencies.

In the sixth chapter we analyze the variability of kinematic source parameters and its implication on the design of shaking scenarios in area of strategic and/or priority interest. In particular we focus on the variability analysis of the ground motion, due to the variation of the seismic source, through the massive use of synthetic scenario computations. The shaking scenarios are predicted by using a single fault plane with the focal mechanism similar to the 1980 Irpinia, Italy, earthquake (M_w 6.9). We study the variability generated by four different types of source parameters: the slip distribution, the rupture velocity, the nucleation point and the slip velocity source time function. This analysis allows in a second step to combine the information in more complex situations where are involved different stations and/or different ground motion parameters in order to select the most representative scenarios.

The results presented in the current Ph.D. thesis have been discussed in the following papers:

Piatanesi, A., A. Cirella, P. Spudich and M. Cocco, 2007, A global search inversion for earthquake kinematic rupture history: Application to the 2000 western Tottori, Japan earthquake, J. Geophys. Res., 112, B07314, doi:10.1029/2006JB004821.

Cirella, A., A. Piatanesi, E. Tinti and M. Cocco, Rupture process of the 2007 Niigata-ken Chuestu-oki, Japan earthquake, by nonlinear joint inversion of strong motion and GPS data, submitted to Geophys. Res. Lett.

Cirella, A., A. Piatanesi, E. Tinti and M. Cocco, Dynamically consistent source time function to invert kinematic rupture histories. PartI: Sensitivity and resolution analysis, submitted to Geophys. J. Int.

Cirella, A., A. Piatanesi, E. Tinti and M. Cocco, Dynamically consistent source time function to invert kinematic rupture histories. PartII: Application to the 2000 western Tottori, Japan earthquake, submitted to Geophys. J. Int.

Cultrera, G., A. Cirella, A. Herrero., E. Spagnuolo and E. Tinti, Variability of kinematic source parameters: Implication on design scenario, in preparation for Tectonophysics.

Chapter 1

Kinematic modeling of seismic source

1.1 Introduction

The practical goal of earthquake seismology is to prevent or reduce losses due to earthquakes by estimating the seismic hazard at a given site or by forecasting the occurrence of the next strong event. The prevailing approach to these problems is to extrapolate data from the record of past events and apply that information to the future. This approach risks to be unreliable, due mainly to the lack of representative data. Fortunately, recurrence times of strong earthquakes are very long, namely, hundreds or thousands of years, whereas the subject of seismology is only centennial. Obviously, an understanding of the earthquake generation process can partly fill the gaps in the available data, thereby making the practical conclusions more reliable.

This is the purpose of earthquake source studies.

The problem of determining the source parameters of an earthquake has always been a main topic of investigation for earth scientist, extending from hypocenter location to magnitude estimation, moment tensor solution and finite-fault kinematic and dynamic imaging of rupture history. In particular, kinematic parameters of the rupture process form the basis of our inferences about the nature of earthquakes and provide a stepping stone for understanding the earthquake physics.

The spatial and temporal distribution of source parameters is critical in forward modeling of ground motion that can be used for engineering design purposes and to study the effects of complex earth structure. Kinematic parameters have been used to infer scaling properties and as input in dynamic modeling in an attempt to determine some frictional parameters.

The characteristics of the earthquake source can be inferred from observations of the recorded ground motion. Kinematic source models are usually obtained by inverting seismic data, collected during a seismic event.

However, even using a simplified kinematic description of the rupture process, the problem of inverting ground motion data to retrieve the rupture history on a finite fault is strongly affected by the inherent nonuniqueness of the problem and by the nonlinearity existing between the observables and the source kinematic parameters.

In order to formulate a physically meaningful slip-inversion problem, one has to take into account several important aspects, such as the quality of available recorded datasets, the consistency of the assumptions made to represent the source process, the stability and reliability of the obtained rupture models, and the assessment of model uncertainty.

These key features represent the main tasks of the current scientific research.

1.2 Seismic source representation theory

An earthquake is the manifestation of sudden slip along a fault plane and it is due to the release of stress accumulated during tectonic deformation. The fact that earthquakes occur suddenly implies local instability of tectonic deformation associated with stress release and with the formation of fractures (fault planes, dislocations) inside the earth.

In the characterization of the earthquake source the earth' material outside the fracture is assumed as an elastic and continuum medium. This implies that the stress in the medium depends only on strain (*Hooke's law*) and that small-scale inhomogeneities can be neglected (*Kostrov and Das*, 1988). Hence, an earthquake source can be defined as a displacement discontinuity in the earth's material due to elastic (shear) stress accumulated during the process of tectonic deformation.

A fracture represents an earthquake source only during its dynamic propagation, characterized by three phases: the onset of dynamic propagation (initiation of fracture), the propagation of fracture itself, and the fracture's arrest.

The processes describing the earthquake in progress represent the coseismic stage of the seismic cycle.

The theory of elasticity constitutes the theoretical basis of seismic source mechanics. The solution of the elasto-dynamic equation gives us the opportunity to relate forces in the medium to measurable displacements.
This fundamental equation is inferred from the equations of motions:

$$\rho \ddot{u}_n = f_n + \tau_{nj,j} \tag{1.1}$$

$$T_n = \tau_{nj} n_j \tag{1.2}$$

where ρ is the density of the body, $\ddot{u}_n$ is the second time derivative of the displacement field that describes the deformation of the body, f_n is the nth component of the external body force density acting per unit volume, and T_n is the traction component related to the stress tensor $\tau_{nj,j}$ by the Eq.(1.2).
For an homogeneous, isotropic and elastic medium the reology is specified by the following constitutive linear relation:

$$\tau_{nj} = \lambda \varepsilon_{kk} \delta_{nj} + 2\mu \varepsilon_{nj} \tag{1.3}$$

where λ and μ are the Lame-constant, δ_{nj} is the Kronecker function and ε_{nj} is the component of the elasticity strain tensor. In order to parameterize the seismic source we need to solve the Eq.(1.1) coupled with Eq.(1.3).

The representation theorem expresses the elastic displacement as a function of space and time resulting from a displacement discontinuity in a general elastic medium and relates an observable quantity, such as ground motion, to the parameters of an idealized model of seismic source.

Aki and Richards (2002) give a representation theorem valid for a source distributed in a volume V with surface S, in which the displacement field u is composed of three terms: the contributions from the body forces acting in the volume, the contributions due to tractions and the contributions from the displacement itself (see equation 2.41 of *Aki and Richards*, 2002).

Each contribution involves a point-force Green's function *G*, defined as the solution of the equation of motion caused by a unidirectional instantaneous unit impulse, precisely located in space and time (the *Delta*-function).

This theory is based on volume sources.

Here we will focus on displacement discontinuities, as this seems to be the most intuitive choice after Reid (1910) stated that the 1906 San Francisco earthquake was due to spontaneous slip on an active geological fault.

A fault can be mathematically represented by a surface Σ embedded in *S* and characterized by two internal surfaces, Σ^- and Σ^+. If slip on Σ occurs, the displacement field is discontinuous but the equation of motion is still satisfied throughout the "interior" of $S + \Sigma^- + \Sigma^+$ (*Aki and Richards*, 2002) and the previously described representation theorem can be applied. In this approach the surface *S* is no longer of interest (could be the Earth surface) and hence we can assume that both *u* and *G* satisfy the homogeneous boundary conditions on *S*. Under these assumptions, the *n*-th component of elastic displacement, caused by the dislocation on the fault, at observation position **x** and time *t* is given by the following integral equation:

$$u_n(\mathbf{x},t) = \int_{-\infty}^{+\infty} dt' \int_V G_{np}(\xi, t-t'; \mathbf{x}, 0) f_n dV + \\ + \int_{-\infty}^{+\infty} dt' \iint_S C_{pqkl} n_k s_l \partial_{\xi_q} G_{np}(\mathbf{x}, \xi, t-t'; \xi, 0) dS - \int_{-\infty}^{+\infty} dt' \int_S \left[G_{np}(\mathbf{x}, \xi, t-t'; \xi, 0) T_n \right] dS \tag{1.4}$$

where $G_{np}(\mathbf{x}, \xi, t-t'; \xi, 0)$ is the *n*-th component of displacement at position **x** and time $t-t'$ caused by an instantaneous force of unit impulse applied in the *p* direction at position **x** and time $t = 0$; $\hat{n}$ is a unit vector normal to *S* pointing into the positive side of *S*, C_{pqkl} is the moduli tensor of elastic deformation and the displacement discontinuity **s** is the difference in displacement (dislocation) between the positive and negative sides of the fault, $\mathbf{s}(\xi, t) = u(\xi^+, t) - u(\xi^-, t)$, where ξ is a point on surface *S*.

1.2.1 Kinematic source model

The first term of Eq.(1.4) accounts for the body forces and its effect is negligible during the short time interval of the coseismic phase. Considering as boundary conditions the discontinuity of displacement and the continuity of traction on the fault surface, the Eq.(1.4) becomes:

$$u_n(\mathbf{x},t) = \int_{-\infty}^{+\infty} dt' \iint_S C_{pqkl} n_k s_l \partial_{\xi_q} G_{pn}(\boldsymbol{\xi}, t-t'; \mathbf{x}, 0) dS \tag{1.5}$$

Eq.(1.5) is called Volterra's Theorem and provides us an extremely useful representation theorem for dislocation sources.

The traction associated with the Green's function in Eq.(1.5) is given by $T_{ln} = C_{pqkl} n_k \partial_{\xi_q} G_{pn}$. Hence the Eq.(1.5) can be written (*Spudich*, 1980) as:

$$u_n(\mathbf{x},t) = \int_{-\infty}^{+\infty} dt' \iint_S s_l(\boldsymbol{\xi}, t') \cdot T_{ln}(\boldsymbol{\xi}, t-t'; \mathbf{x}, 0) dS \tag{1.6}$$

This representation defines a *kinematic source model*, in which the deformations on the Earth are derived from a slip vector $\mathbf{s}(\boldsymbol{\xi}, t')$ that represents the dislocation on the fault plane, as a function of the time and position on the fault.

The slip rate vector $\dot{\mathbf{s}}(\boldsymbol{\xi}, t')$, defined as the derivative of the displacement field, is the central element of a kinematic faulting model.

The slip rate vector represents one's understanding of the behavior of the earthquake rupture. Following Spudich and Frazer (1984), an extended finite fault can be described by a slip rate distribution *S* such that:

$$\mathbf{S}(\boldsymbol{\xi}, t) = \dot{\mathbf{s}}(\boldsymbol{\xi}, t) = \dot{f}(t - t_r(\boldsymbol{\xi})) \cdot g(\boldsymbol{\xi}) \tag{1.7}$$

where $\dot{f}(t)$ is the source time function (STF) and it prescribes the slip-velocity evolution during rupture propagation on the fault; $t_r(\boldsymbol{\xi})$ is the rupture time and $g(\boldsymbol{\xi})$ is the scalar value of the total slip or peak slip velocity spatial distribution on the fault plane, depending on the normalization of the source time function $\dot{f}(t)$.

Using this representation framework, the rupture process is entirely specified by the spatio-temporal distribution of the slip vector, the rise time (slip duration), and how the rupture propagates over the fault plane (rupture velocity). This variables represent the suit of kinematic parameters describing a seismic source.

1.3 Inversion methods

An earthquake can be considered a source of information, the acquisition of which is the subject of seismology. The information conveyed by the observational data consists of two fundamentally different parts: the first is created during the excitation of waves at the source of the earthquake; the second is produced by the conditions of wave propagation from the source to the station, that is, by the structure of the medium. Consequently, the interpretation of seismic observations requires the solution of two fundamentals problems: the determination of the velocity structure of the medium (earth's structure), and the determination of the earthquake source parameters. These problems, typical of the analysis of geophysical data, are essentially problems of data inversion: observed geophysical data usually collected on the Earth's surface, and which have been affected by the variation in properties of the earth material, are used to infer physical parameterization of the Earth's interior.

In particular, the inverse problem for the earthquake source has been formulated as one of reconstructing the spatio-temporal evolution of the dislocation on the fault plane. As it is usual in geophysics, one can neither experiment with nor directly observe the earthquake focal region; one can only investigate its manifestation at the earth's surface. To convert this manifestation into information on the earthquake source process, one must have some general theoretical model that can then be fit to observational data. This task is achieved by first constructing a mathematical model, necessary to generate synthetic data, in which the physical parameters are unknowns. Inverse problems are then solved to determining model(s) that minimize the misfit between observed and synthetic data (*optimization* process). The misfit function (also called the objective function, cost function, error function, energy function, etc.,) is usually given by a

suitable defined norm, to represent a measure of acceptability of a model. Question of uniqueness aside, these optimization problems can be broadly classified into two types: those that contain only one minimum of the misfit function, and those that contain more than one minimum.

The commonly accepted definition, given by Tarantola (1987), classifies inverse problems into linear, weakly nonlinear, quasi-linear and highly nonlinear problems. The case with one minimum is called linear inversion, because the solution may be obtained (approximately) solving a set of linear equations. When there are many minima, no such set of linear equation exists unless important additional assumptions are made. The lack of these assumptions requires nonlinear inversion (location of the global minimum in the presence of many local minima). Nonlinear inverse problems are usually solved with linearized techniques (direct, linear and iterative-linear inverse methods) that depend strongly on the accuracy of initial estimates of the model parameters. With linearization, objective functions can be minimized efficiently, but the risk of local rather than global optimization can be severe (*Rothman,* 1985); the existence, uniqueness and stability of the solution can be strongly compromised. Excellent texts on inverse theory as applied to geophysics are those by Menke (1989), Tarantola (1987) and Sen and Stoffa (1995).

The seismic finite-fault inversion problem involves finding a rupture model (specified by a combination of kinematic parameters on a fault) that minimizes the misfit function between the recorded data and their theoretical predictions.

It is faced with three features: (1) the model space is very large, typically of the order of 50^{50} (*Sen and Stoffa*, 1991); (2) the misfit function is multimodal; (3) the basic nature of the kinematic parameters (slip amplitude, slip direction or rake, rupture velocity and rise time (duration of slip) on the fault) and their relationships to the data (expressed by the representation theorem) may present important complexities to solve.

Eq.(1.7) describes the seismic source by a slip rate function, given as the product of a spatially varying slip intensity with a time dependence of slip after rupture, that varies as a function of position on the fault. The time dependence is governed by the variation in the slip duration as well as by the heterogeneities of the rupture

velocity on the fault plane. These two aspects are implicitly contained in the functional form of the source time function $\dot{f}(t)$ and introduce a strong nonlinearity between the observed ground motion and the temporal quantities describing the rupture process.

Adopting an impulsive source time function, such as a *delta* function, this problem does not appear; but it is well known that real faults could be characterized by very complex source time functions. The seismic waves radiated by a finite source are not impulsive; different points on the fault plane broken on different times, depending on the rupture velocity distribution on the fault and on the distance between each point and the nucleation point. Besides, on each point of the fault plane, the dislocation does not occur instantaneously, but it takes a certain time to reach its final value; this time is the rise time. This means that the spatio-temporal evolution of the slip on the fault shows a linear relation between the ground motion and the distribution of slip amplitude $g(\xi)$ but a strong nonlinearity with the source time function $\dot{f}(t)$, (i.e. with the temporal quantities (rupture time and rise time) of rupture process).

Consequently, determining these temporal variables along with the slip is a nonlinear problem.

Thanks to contemporary computational tools, most seismologists are facing the finite-fault inversion in its full non-linear formulation, rather in a linearized form solved through matrix inversion. Nevertheless, some investigators still prefer to use a linear (or linearized iterative) approaches (*Graves and Wald*, 2001; *Semmane et al*., 2005); when non-linear inversions are performed, all parameters are inverted simultaneously using global search method (e.g. *Emolo and Zollo*, 2005; *Ji et. al.*, 2002; *Liu and Archuleta*, 2004).

Global search techniques belong to the Monte Carlo optimization methods and are powerful tools when searching for globally optimal solutions amongst numerous local optima (*Mosegaard and Sambridge*, 2002).

In general a Monte Carlo technique can be defined as a method that use *pseudorandom* sampling to search a parameter space to retrieve Earth models or other information about the unknowns of interest (*Sambridge and Mosegaard*, 2002). The important feature is that random sampling from highly nonuniform

multidimensional distribution is possible. Monte Carlo techniques include Simulated Annealing, Genetic Algorithms, and other important sampling approaches.

We will focus our attention on the Simulated Annealing algorithm.

1.3.1 Simulated Annealing algorithm

Simulated Annealing is a Monte Carlo optimization technique that mimics the physical process by which a crystal is grown from a melt.

When crystalline material is slowly cooled through its melting point, highly ordered, low-energy crystals are formed. The slower the cooling, the lower the final lattice energy. This physical process is a natural optimization method where the lattice energy E is the objective function to be minimized and the state space variables are identified with parameters of the system. Thermal fluctuations in the system are simulated by randomly perturbing its parameters, and the size of the fluctuations are controlled by a temperature parameter.

Since the work of Kirkpatrick et al. (1983), the simulated annealing method has been used in many parameter optimization problems (*Rothman,* 1985, 1986). The simulated annealing algorithm is a specialization and modification of the Metropolis algorithm (*Metropolis et al*., 1953). Metropolis et al.(1953) addressed the problem of random sampling from a Gibbs-Boltzmann distribution at constant temperature T, thereby simulating the average behavior of a physical system in thermal equilibrium.

The Metropolis algorithm involves taking a random walk (random perturbation) in the model space. At each step the change in the energy ΔE is then calculated.

The model is accepted if $\Delta E < 0$. However if $\Delta E > 0$, then the new model is accepted with the probability $P(\Delta E) = \exp(-\Delta E/T)$.

Simulation of chemical annealing is now performed by gradually lowering the temperature T (by means of a given *cooling schedule*) from a high value to just below T_c, the critical temperature at which a phase change occurs. Close to T_c the Gibbs-Boltzmann distribution approximates a delta function at the global minimum for E, the system reaches equilibrium (a state of minimum energy) , in

which configurations of parameters are realized with a Gibbs probability distribution. Because each step of the algorithm is dependent only on the present and not on the past, the algorithm can be formally studied using Markov chain theory (*Hammersley and Handscomb*, 1964). A proof of convergence of the algorithm can be found in Geman and Geman (1984).

An equivalent (and faster) alternative to this algorithm is the single-step heat-bath method (*Rothman*, 1986) which computes the relative probability of acceptance for each possible move before any random choice is made, i.e., it produces weighted selections that are always accepted. The conditional acceptance P(ΔE) is easily implemented by choosing a random number α uniformly distributed between 0 and 1. If $\alpha \leq$ P(ΔE), then the perturbation is accepted; otherwise the existing value of the parameter is retained.

In the heat-bath algorithm (see scheme in Figure1.1) each value of the model parameter is visited sequentially for all possible values of one model parameter while keeping the values of all other parameter fixed.

Heat Bath Algorithm

start at a random location $\mathbf{m}_0$ with energy $E(\mathbf{m}_0)$
loop over temperature (T)
- loop over number of iterations/temperature
  - loop over number of model parameters ($i = 1, \ldots, N$)
    - loop over model values $j, j=1, \ldots, M$
      - evaluate $E(\mathbf{m} \mid m_i = m_{ij})$ and calculate

$$\hat{P}_{ij} \propto \exp\left(-\frac{E\left(\mathbf{m} \mid m_i = m_{ij}\right)}{T}\right)$$

    - end loop
    - draw a j from the above distribution
  - end loop
- end loop

end loop

Figure1.1 A pseudo Fortran code for heat bath simulated annealing algorithm

The following Gibbs probability distribution is then evaluated:

$$P(m_{ij}) = \frac{\exp(-E(m_{ij})/T)}{\sum_{j=1}^{M} \exp(-E(m_{ij})/T)} \tag{1.8}$$

where the subscript i (from 1 to N) refers to the model parameters and the subscript j (from 1 to M) refers to the values the model parameters can take. Thus, there are M^N possible models. A random value is drawn from the above distribution and is always retained. Let our model vector **m**, where each m_i represents a model parameter, that can take M different values (in general, M can be different for different model parameters). The algorithm starts from any point in the model space and holds all the model parameters fixed except the first.

Now, with fixed value of m_2 through m_N and M possible values of m_1 (m_{11} through m_{1M}), the algorithm generates the energy function $E(m_{ij})$ and evaluates the distribution given in Eq.(1.8). A value is drawn from the distribution and the new value of m_1 is retained. Next, all the model parameters are kept fixed, except m_2, and the same process is repeated for all N model parameters.

We refer to this entire process as "one iteration" and note that $M \cdot N$ forward calculations are performed in each iteration. Several iterations are performed at a fixed temperature; then the temperature is lowered and the procedure is repeated until 'crystallization' occurs, i.e., the system reaches a low energy (near the global minimum) state.

This is the algorithm we implement in our new nonlinear inversion technique (presented in Section 1.6).

1.4 Single-window and multi-window approaches

Inversion for the kinematic slip history on a finite-fault plane can be traced back to Trifunac (1974). The pioneering finite-fault inversion methods have been proposed during the early 1980s, mainly to study the 1979 Imperial Valley earthquake (e.g. *Olson and Aspel*, 1982; *Hartzell and Heaton*, 1983 among several others). During the past two decades, many different methods have been

developed to invert for the earthquake rupture process from geophysics data. Distinctions among inversion methods depend on the different adopted inversion schemes and on different assumptions and constraints. If we focus the interest on the definition of the temporal evolution of the kinematic source parameter on the fault plane, we can divide the different procedures into two groups: those belonging to the single-time window approach and those belonging to the multi-time window approach.

In the single-window approach each point on the fault can slip only once, when the rupture front passes. Variations in the slip amplitude are allowed and variations in rupture velocity are accommodated by allowing the rupture time to vary. The main advantage of this approach is that both the slip and rupture front time distribution on the fault can be determined simultaneously (*Beroza and Spudich*, 1988, *Olson and Anderson* 1988, *Fukuyama and Irikura,* 1986; *Zeng and Anderson,* 1996; *Hartzell and Liu,* 1995; *Ji et al,*. 2002).

The other main approach is the multiple-time window inversion (*Olson and Aspel*, 1982; *Sekiguchi et al*., 2000; *Zhou et al*., 2004), in which each point on the fault is allowed to rupture multiple times. This allows flexibility in the rupture time and hence the rupture velocity. Variations in the slip-velocity are accommodated by variations in the slip amplitude in each time-window. Because the multi-window method allows greater flexibility, it has the potential to describe a wider range of faulting behavior; however, with the increased flexibility, an increase of unknown parameters in the inversion comes and the solutions are less stable. Cohee and Beroza (1994) have investigated the differences in source inversions that use this two approaches and found that single-time window technique does a better job of recovering the true seismic moment and the average rupture velocity, allowing larger variations in rupture time with fewer model parameters. Moreover, in single-time window inversion procedures the temporal evolution of slip velocity (see Eq.(1.7)) is prescribed by assuming an analytical expression of source time function; while, the source time functions adopted in multiple-time window methods are rather crude, and the final source time function is given by a superposition of several functions (a simple triangular function in most cases) appropriately shifted on time.

1.5 Model uncertainty

The inverse problem of estimating earth model parameters from observations of geophysical data often suffers from the fundamental limitation that several models may explain the data equally well. This phenomenon, which has been called "nonuniqueness", may be caused by several factors. The most well recognized is that the real earth properties vary continuously in all spatial directions and we are facing with the problem of constructing an earth model from a finite set of measurements. Thus the inverse problem is highly under-determined and will result in many non-unique solutions (e.g., *Menke*, 1989). Since in many cases the earth may be modeled with a discrete set of layers based on independent information (parameterization of the earth), this type of nonuniqueness can be greatly reduced.

Another cause of nonuniqueness is related to the problem of the model's definition and to the sensitivity of the model to the data. Indeed, any noise (either random or systematic) present in the data or use of inexact theory to predict a model from the data may also cause a large degree of uncertainty in the results. Thus any performer is faced with several choices for the earth model and often the number of choices can be reduced based on the prior knowledge of the earth models. Several attempts have been made to reduce uncertainty by imposing constrains such as regularization or solving for smooth models. Of course, what kind of smoothing is appropriate is highly debatable.

Although much attention has been devoted to developing methods which efficiently search a parameter space, much less effort has been devoted to the problem of analyzing the resulting ensemble in a quantitative manner (*Sambridge*, 1999b). Only in the past few years, geophysicists have begun to develop techniques for ensemble inference. The earliest use of Monte Carlo methods was for probabilistic, or randomized, searching of a parameter space; their role is to explore a multidimensional parameter space and collect models which fit the observed data to some satisfactory level. With these derivative-free search methods one is forced to solve the forward problem many times; that is, to calculate predictions based on a earth model, and compare them to the observations. This results in a large ensemble of models, and the task is to try and

use their collective sampling to draw inferences. The question remains of how to extract robust information from an ensemble of models with a range of fits to the data. In principle, the entire ensemble may provide useful information from which to draw inferences; also models which fit the data poorly may tell us just as much as those which fit the data well (*Sambridge*, 1999b). A useful thing to do is to find an ensemble of models that sample the good data-fitting regions of parameter space, rather then seeking a single optimal model, as done by Press (1968, 1970a). Several authors have suggested methods for describing an ensemble of data acceptable models. A useful review is given by *Sen and Stoffa* (1995). The earliest approach was simply to compare models directly, by plotting (*graphical methods*) them on top of one another (*Nolte and Frazer*, 1994; *Shibutani et al.* 1996; *Kennett,* 1998). An alternative to graphical methods is the cluster analysis method proposed by Vasco et al. (1993). They used statistical techniques to characterize the acceptable ensemble and make inferences about properties shared by models. *Sambridge* (1999a; 1999b) has proposed an approach to estimate Bayesian information measures from an arbitrarily distributed ensemble.

The underlying idea of the developed techniques for ensemble inference, is that basing inferences on an ensemble of potential solutions is more useful than considering just the features present in only the best data-fitting model. Since, in almost all cases, this is insufficient because of nonuniqueness in the problem and noise in the data (*Sambridge and Mosegaard*, 2002).

1.6 A new nonlinear inversion technique

In this section we propose a new global nonlinear inversion procedure to retrieve complete kinematic rupture histories on a finite fault.

The representation theorem for earthquake rupture (see Section 1.2) forms the basis for computing synthetic seismograms, which are necessary both to predict ground motions and to develop a formalized slip inversion (*Olson and Aspel*, 1982). To resolve the representation theorem integrals on a fault surface we use the Compsyn package (*Spudich and Xu*, 2003) based on the numerical techniques of Spudich and Archuleta (1987). The Compsyn applications allow us to obtain

ground displacements through a compact form of the representation theorem given by Spudich (1980):

$$\mathbf{u}_k(\mathbf{x},\omega) = \int_S \mathbf{S}(\xi,\omega)\cdot\mathbf{T}_k(\xi,\omega;\mathbf{x})d\xi \tag{1.9}$$

which is the frequency domain version of Eq.(1.6); where **x** is the position of the observer, $\boldsymbol{\xi}$ is the local coordinate system on the fault plane *S*, *k* denotes the x, y or z direction, $\mathbf{u}_k(\mathbf{x},\omega)$ is the Fourier transform of the *k*-component of ground velocity at observer location **x** and angular frequency ω, $\mathbf{S}(\xi,\omega)$ is the Fourier spectrum of $\mathbf{S}(\boldsymbol{\xi},t)$, which is the slip rate distribution at point $\boldsymbol{\xi}$ on the fault; $\mathbf{T}_k(\xi,\omega;\mathbf{x})$ is the Fourier transform of the traction vector at a point $\boldsymbol{\xi}$ on the fault caused by a point impulsive force in the *k*-direction at observer location **x.**

This form of the representation theorem uses Green's function reciprocity. We calculate the traction Green's functions on the fault plane using a Discrete Wave-number/Finite Element (DWFE) integration technique that allows for the complete response in a vertically varying medium (*Olson et al.,* 1984*; Spudich and Archuleta,* 1987).

1.6.1 Finite fault parameterization

In performing the integrals of Eq.(1.9), an assumption frequently made in seismology is that a large earthquake can be simulated by a grid of point dislocations (*Heaton and Helmberger,* 1979; *Bouchon*, 1982; *Heaton,* 1982, *Hartzell and Helmberger,* 1982; *Campillo and Bouchon,* 1983; *Liu and Helmberger,* 1983). Under this assumption the response of a finite fault at a station can be approached by summing the contributions of a regular grid work of subfaults (e.g., *Hartzell and Heaton*, 1983):

$$u(\mathbf{x},t) = \sum_{i=1}^{n}\sum_{j=1}^{m} g_{ij}\left[\cos(\lambda_{ij})Y_{ij}^{1}(V_{ij},t) + \sin(\lambda_{ij})Y_{ij}^{2}(V_{ij},t)\right]\dot{f}_{ij}(t) \tag{1.10}$$

Here, $u(\mathbf{x},t)$ is the ground velocity at an arbitrary station, i is the ith subfault along strike, and j is the jth subfault down dip. g_{ij} and $\dot{f}_{ij}(t)$ are the dislocation (or the peak slip velocity) amplitude and the slip velocity source time function described by Eq.(1.7). λ_{ij} and V_{ij} are the rake and the rupture velocity, respectively. The terms $Y_{ij}^{1}(V_{ij},t)$ and $Y_{ij}^{2}(V_{ij},t)$ are the subfault Green's functions for the unit slip in the strike and down-dip direction, respectively. Each of such function is obtained by summing the responses of point sources uniformly distributed over it.

On the basis of the described conventional finite fault parameterization, we can assign the kinematic source parameters at the corners of each subfaults. However, the value of a parameter is not constant inside a subfault. Rather, it is allowed to vary through a bilinear interpolation of the nodal values, in a way similar to that used by *Liu and Archuleta* (2004) (see also *Beroza and Spudich*, 1988; *Ide and Takeo*, 1997). At each node we give the time of rupture onset, the rise time, the peak slip velocity (we can also invert for the slip displacement) and the rake angle; which are spatially variable to account for the actual rupture complexity. Here the rupture velocity of a node is defined as the average speed of rupture from the hypocenter to this node. The local rupture velocity at a node may be significantly greater or less than the corresponding average velocity. In the present implementation of our method, each point on the fault can slip only once, as opposed to multiple time windows approaches in which STFs consist of a sequence of triangles. With a single window-time approach we can determine the portion of the data that can be fit with a simple source time function as opposed to a complicated and possibly over-parameterized STF.

1.6.2 Implementation: Source time function

From Eq.(1.9) it follows that the spectral properties of the source time function contribute in controlling the spectra of ground motion. We implement in the original Compsyn-code, proposed by Spudich and Xu (2003), different functional forms of source time function proposed in the recent literature. The slip velocity is

defined by Eq.(1.7), where $\dot{f}(t)$ (whose unit is s^{-1}) is the source time function for a given distribution of final slip $D_{max}(\xi)$ or for a given distribution of peak slip velocity $V_{peak}(\xi)$, depending on the adopted normalization. $\boldsymbol{\xi}$ =(ξ_1, ξ_2) represents the local coordinate on the fault plane, t is time and $t_R(\xi)$ the rupture time.

We assume three distinct source time functions $\dot{f}_i(t)$ characterizing slip velocity:

$$\dot{f}_1(t') = H(t' - \tau_R(\xi))H(\tau_R(\xi) - t'); \tag{1.11a}$$

$$\dot{f}_2(t') = \frac{1-\cos(2\pi t' / \tau_R(\xi))}{\tau_R(\xi)}; \qquad 0 < t' < \tau_R(\xi) \tag{1.11b}$$

$$\dot{f}_3(t') = \int_{-\infty}^{+\infty} \mathrm{W}(t' - \mathrm{T})\mathrm{Y}(\mathrm{T})\mathrm{dT}\ ; \tag{1.11c}$$

where $t' = t - t_R(\boldsymbol{\xi})$ and $\tau_R(\xi)$ is the rise time.

In the latter equation $H(t)$ is the Heavside function, $W(t)$ and $Y(t)$ are defined below. These relations define source time functions already known in the literature: (1.11a) is a boxcar, (1.11b) is a modified cosine function used by Ji et al. (2002) while (1.11c) is a regularized Yoffe function proposed by Tinti et al. (2005a). The latter function is given by equation (1.11c), where $Y(t)$ and $W(t)$ are the original Yoffe function (*Yoffe*, 1951) and a triangular function, respectively, and can be expressed as follow:

$$\mathrm{Y(t)} = \frac{2}{\pi\tau_R(\xi)} H(t)H(\tau_R(\xi) - t)\sqrt{\frac{\tau_R(\xi) - t}{t}}; \tag{1.12a}$$

$$W(t) = \frac{1}{{\tau_S}^2}\left[\mathrm{tH(t)H}(\tau_\mathrm{S} - \mathrm{t}) + (2\tau_\mathrm{S} - \mathrm{t})\mathrm{H}(\mathrm{t} - \tau_\mathrm{S})\mathrm{H}(2\tau_\mathrm{S} - \mathrm{t})\right]; \tag{1.12b}$$

where τ_S is the half-duration of triangular function by which the original Yoffe is convolved in order to remove it's singularity at the rupture front.

The regularized Yoffe function is a flexible source time function defined by three independent parameters: the final slip, the slip duration and the duration of the positive slip acceleration T_{acc}. This new source time function is consistent with dynamic '*pulse-like*' earthquake ruptures and makes feasible the dynamic

interpretation of kinematic slip models (*Nielsen and Madariaga*, 2003; *Piatanesi et al.*, 2004). Figure1.2 shows the slip (upper panel) and slip velocity (bottom panel) functions defined above.

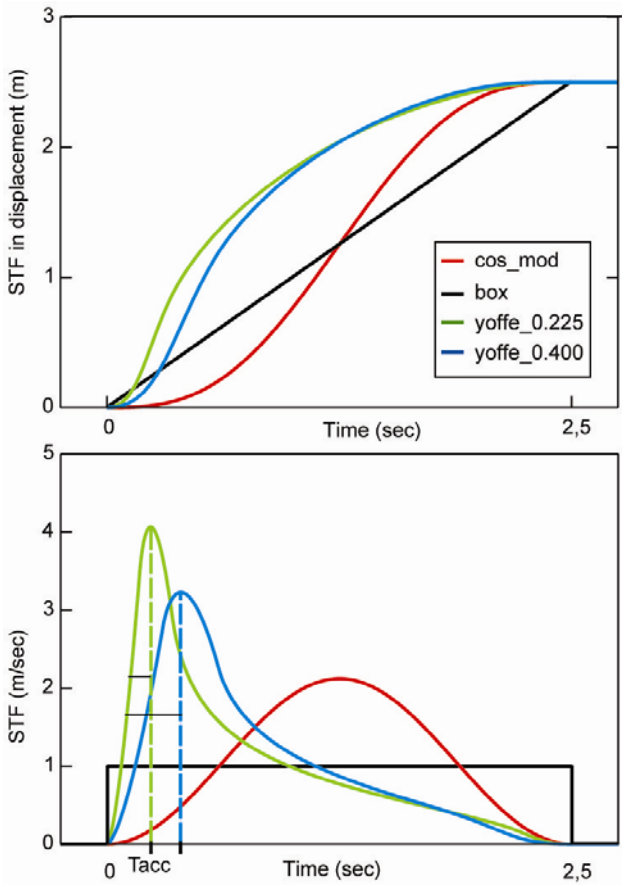

Figure1.2. Slip velocity (bottom panel) and slip (upper panel) functions of a boxcar (black line), a modified cosine (red line), and two regularized Yoffe, with different values of T_{acc} (green and blue lines) source time functions.

In particular, Figure1.2 shows two different examples of f_3, that vary only for T_{acc} value (0.4 sec and 0.225 sec for the blue and green curve, respectively); it is evident how the variation in T_{acc} affects the peak of slip velocity. All the functions in Figure1.2 have the same total slip.

As we have told in the previous section, our procedure allows to invert for the peak slip velocity as well as for the total slip.

When we invert for the peak slip velocity we use the following formulation:

$$\mathbf{S}(\xi,t) = \dot{\mathbf{s}}(\xi,t) = \dot{f}(t - t_r(\xi)) \cdot V_{peak}(\xi) \qquad (1.13)$$

where the source time function is normalized to have a unit peak slip velocity value:

$$\dot{f}(t) = \frac{\dot{f}_i(t)}{\max\left|\dot{f}_i(t)\right|} \tag{1.14}$$

When we invert for the total slip we use the following formulation:

$$\mathbf{S}(\xi,t) = \dot{\mathbf{s}}(\xi,t) = \dot{f}(t - t_r(\xi)) \cdot D_{\max}(\xi) \tag{1.15}$$

where the source time function is normalized to have a unit integral over time:

$$\dot{f}(t) = \frac{\dot{f}_i(t)}{\int \dot{f}_i(t)dt} \tag{1.16}$$

The subscript *i* identifies the different source time functions given by Eq.(1.11a, 1.11b, 1.11c).

The implemented STFs can be used both in forward modeling and in kinematic inversion on finite fault. In particular, we include the implementation of these different STFs in our kinematic inversion procedure (*Piatanesi et al*., 2007), described in the next section.

1.6.3 Inversion procedure

The relationship between the observed ground motion and the variables characterizing the spatio-temporal evolution of the rupture process on the fault is critical because of its non-linearity (see Eq. (1.7)). Solving for the distribution of slip or peak slip velocity amplitude is a linear problem whereas the temporal quantities, like rupture time and rise time, are strongly not linearly related to the data (*Archuleta*, 1984).

Instead of linearizing the problem and applying linear inverse theory we use a new two-stage nonlinear technique to jointly invert strong motions records and geodetic data (*Piatanesi et al*., 2007). We use a global optimization method to search for the source parameters (e.g. *Hartzell and Liu*, 1995; *Ji et al*., 2002; *Liu and Archuleta*, 2004).

In particular we implement a special flavor of the Simulated Annealing technique (see Section 1.3.1), called the "heat-bath" algorithm (*Rothman*, 1986),

which is very efficient for exploring high dimensional model spaces (*Sen and Stoffa,* 1995). The algorithm works by perturbing the model parameters one by one; for this reason, as indicated by *Ji et al.* (2002) and *Liu and Archuleta* (2004), synthetic seismograms from only those subfaults sharing the current nodal parameter need to be updated at each perturbation, thus reducing the computational time.

Since the forward modeling is relatively fast for computing waveform spectra, recorded and synthetic seismograms are compared in the frequency domain, using both real and imaginary parts of the signal's spectra. A main point in inverse problems is the choice of a suitable cost function to represent the goodness of a model. For waveform spectra, we use an objective function that is a hybrid representation between L1 and L2 norm (*Spudich and Miller*, 1990; *Sen and Stoffa*, 1991):

$$E^S(\mathbf{m}) = \frac{1}{N_S}\sum_{i=1}^{N_s} w_i \left[1 - \frac{\sum_{k=1}^{N_f} v_r(\omega_k) v_s^*(\omega_k) + v_r^*(\omega_k) v_s(\omega_k)}{\sum_{k=1}^{N_f} v_r(\omega_k) v_r^*(\omega_k) + \sum_{k=1}^{N_f} v_s(\omega_k) v_s^*(\omega_k)} \right]_i \qquad (1.17)$$

Here $E^S(\mathbf{m})$ is the cost function corresponding to model $\mathbf{m}$, N_s the number of seismograms, N_f the number of frequencies, v_r and v_s are respectively the recorded and synthetic ground velocity spectra, $*$ symbol stands for complex conjugates, ω_k is the k-th frequency of a ground velocity spectrum and w is a relative weight to be assigned to each record. This cost function takes information from both the shape and the amplitude of a waveform and it turns out that it is more robust than standard least squares (*Liu and Archuleta,* 2004; *Ji et al.*, 2002).

The cost function E^G, related to near-field GPS measurements, is a sum-squared of the residuals between synthetic and observed static displacements (*Hudnut et al,* 1996), normalized to the observed data:

$$E^G = \frac{1}{N_G} \frac{\sum_{i=1}^{N_G} \left(\frac{d_i^r - d_i^s}{\sigma_i} \right)^2}{\sum_{i=1}^{N_G} \left(\frac{d_i^r}{\sigma_i} \right)^2} \qquad (1.18)$$

Here N^G is the number of GPS measurements, d^r and d^s are recorded and synthetic displacements respectively and σ is the error associated to the measured data. When we invert simultaneously seismic and GPS data, the total cost function is computed from the summation of the weighted cost function of the two datasets:

$$E = (p_s E^S + p_G E^G)/(p_s + p_G) \tag{1.19}$$

In order to avoid that an improvement in one cost function can be achieved producing a simultaneous degradation in the other one, it is possible to verify different weighting combinations of the dataset cost functions within the joint inversion. To this purpose, for every application we must previously perform several *trial-and-error* runs, giving different weights to the GPS (p_G) and strong motion (p_s) data. In the applications we will present, the results obtained from the *trial-and-error* runs have showed that the right combination, to avoid a degrade of one dataset with respect to the other one, is obtained by setting the weights of the different datasets equals. Furthermore we do not add special constraints, such as smoothing or moment minimization.

The algorithm we propose consists of two stages: a first stage (*Stage I*) in which the algorithm builds up the model ensemble and a second stage (*Stage II*) in which the algorithm appraises the model ensemble.

Stage I: Build up model ensemble

During the first stage, the heat-bath simulated annealing algorithm explores extensively the model space to generate an ensemble of models that efficiently sample the good data-fitting regions. The simulated annealing technique follows the analogy with annealing in thermodynamics, consisting in slowly cooling the system toward the minimum energy state (see Section 1.3.1).

Ideally, large sampling of the model space is achieved by starting the algorithm at relatively high temperature and slowly cooling the system towards the critical temperature, at which the system is expected to reach the minimum energy state (i.e. minimum of the cost function). Since we deal with very large dimension of the model space (typically more than 200 parameters are to be inverted) a true

simulated annealing cannot be realized, because the ideal cooling would require an excessive CPU time and a simulated quenching is performed instead. In the latter case, the cooling is faster than in the ideal annealing and the sampling of the model space may be slightly dependent on the choice of the starting model; for this reason the algorithm is conceived to perform several restarts with different random trial models, in order to make the model ensemble independent from a particular choice of the initial model. During the search, all models that are visited and the corresponding values of the cost function E(m) are saved to build up the model ensemble Ω.

Stage II: Appraisal of the ensemble

The second stage of our algorithm consists of the ensemble inference. The underlying idea is that basing inferences on an ensemble of potential solutions conveys more information than considering just the best. In fact, limiting the analysis to the features present in only the best fitting model is often insufficient because of nonuniqueness in the problem and noise in the data (e.g. *Sen and Stoffa*, 1995; *Sambridge*, 2001; *Kennett*, 2004).

Following the work of *Shibutani et al.* (1996), we compute an averaged model parameter and the associated standard deviation by weighting all models of the ensemble by the inverse of their cost function values. Let m_{ij} be the i-th parameter of the j-th model belonging to the ensemble Ω and E_j the cost function corresponding to the model $\mathbf{m}_j$. The averaged model parameter $<m_i>$ and the corresponding standard deviation $<\sigma_i>$ can be written as:

$$\langle m_i \rangle = \frac{\sum_{j \in \Omega} m_{ij} / E_j}{\sum_{j \in \Omega} 1 / E_j} \tag{1.20}$$

$$\langle \sigma_i \rangle^2 = \frac{\sum_{j \in \Omega} \left[m_{ij} - \langle m_i \rangle \right]^2 / E_j}{\sum_{j \in \Omega} 1 / E_j} \tag{1.21}$$

The estimates $<m_i>$ and $<\sigma_i>$ represent the ensemble properties and are the actual solution of our nonlinear inverse problem. This model assessment is different from those proposed in previous work. *Peyrat and Olsen* (2004) computed the standard deviation from the 19 models with the smallest misfit; *Liu et al.* (2006a) performed 10 inversions that use different seeds for random generation of the starting model and computed the average and standard deviation among the 10 best models.

The novelty of our approach is the use of a very large model ensemble, built up by means of multiple restarts of the annealing algorithm, to take advantage from the whole search process instead of looking only at the best models.

Moreover, our technique allows us to jointly invert for strong motion and GPS data. This feature represents a real improvement in the inversion resolution, since the combination of seismic and geodetic data can offer a more broadband frequency range of observations than the individual seismic datasets (*Ji et al.*, 2002) . Besides, the static data (static component of the seismic data or GPS geodetic data) are particularly helpful for reducing the trade-off between timing and slip distribution and to constrain the co-seismic slip distribution.

Finally, the implementation of different functional forms of source time function provides us the opportunity to investigate the importance of adopting source time function compatible with earthquake physics; in order to better represent the real seismogenetic processes.

Chapter 2

Sensitivity and resolution analysis

2.1 Introduction

Inversion of seismic data has become an effective tool for the reconstruction of faulting processes during large earthquakes and for the understanding of the earthquake source. The rupture process for almost all of the disastrous earthquakes that have occurred during the past two decades, have been studied by different authors with different data and different inversion algorithms. Reading these papers carefully we find that, for the same earthquake, the results of inversions by different authors are usually different and show discrepancies among the retrieved rupture models (*Cohee and Beroza*, 1994).

Examples of recent earthquakes for which different authors have found dissimilar solutions include: the 1979 Imperial Valley earthquake (*Olson and Aspel*, 1982; *Hartzell and Heaton*, 1983), the 1984 Morgan Hill earthquake (*Hartzell and Heaton*, 1986; *Beroza and Spudich*, 1988), the 1987 Superstition earthquake (*Frankel and Wennerberg*, 1989; *Wald et al*., 1990), the 1989 Loma Prieta earthquake (*Steidl et al*., 1991; *Beroza*, 1996), the 1992 Landers earthquake (*Cohee and Beroza*, 1994; *Wald and Heaton*, 1994), the 1995 Kobe earthquake (*Ide et al.*, 1996; *Song and Beroza*, 2004), the 1999 Turkey earthquake (*Bouchon et al*., 2002; *Delouis et al*., 2002), the 1999 Chi-Chi earthquake (*Zeng et al*., 2001; *Thio et al*., 2004).

This leads to a question: on what basis can one judge the reliability of the inversion results?

There are two distinct levels of uncertainty in a formalized slip inversion that may influence the reliability of the results: the method and the parametric uncertainty (*Beresnev*, 2002). The method uncertainty lies at the most fundamental level: it stems from the fact that there is no unique way of constructing an inversion scheme that would satisfy reasonable constraints imposed by both numerical stability and physics. Once the method has been defined, the parametric

uncertainty begins to affect the results; it is defined as the sensitivity of the results to a particular choice of the parameters fixed in the inversion (parameterization scheme).

The reliability of finite-fault inversion for the earthquake source rupture process has been investigated only in some works. Hartzell (1989) discussed the influence on the inversion results of the inversion algorithms and the initial models. Beroza and Spudich (1988) discussed the influence of noise in the data. Several authors pointed out that inaccurate knowledge of the velocity structure represents a main source of error in finite-fault inversion (*Graves and Wald*, 2001; *Wald and Graves*, 2001; *Ji et al.*, 2002; *Liu and Archuleta*, 2004).

For the most part, past studies have concentrated on deriving a model that fits the observed data, without much emphasis on assessing the solution accuracy. It is not difficult to obtain a solution that matches the data acceptably well. The greater challenge lies in estimating the reliability and in answering to the question: how close then could an inverted slip image be to the true one?

It has always been difficult to evaluate the resolution and accurateness of the recovered source rupture process in practical cases because we generally do not know the true source history for natural earthquakes (*Hartzell*, 1989, *Wald and Heaton*, 1994).

In the absence of a possibility to compare the inversion to the true solution, the only way would be to design a known earthquake faulting model and use a set of synthetic data excited by this ‘earthquake’ to recover its original rupture process. The consistency between the inverted and the pre-designed faulting models can help to test the inversion algorithm and indicate the reliability and resolution of the inversion results. The likeness of the inversion and the known solution would support the reliability of inversions of real earthquake data.

The purpose of this chapter is to specifically concentrate on the problem of the uncertainties characterizing the inversion of seismic data for slip distribution on finite faults. In particular we will dwell on the non-uniqueness, sensitivity and resolution issues, as well as analyze two main uncertainty sources, namely the inaccurate knowledge of crustal structure and the not exact knowledge of the source time function.

The basic procedure we use is supported by synthetic test, which consists of: (1) prescribe a source model, observational network; (2) use a forward simulation (*Spudich and Xu*, 2003) with the prescribed source model and observational stations to calculate a set of synthetic 'data'; (3) use different velocity structure and various source parameterizations to invert for the source rupture process and analyze their influence by comparing the resulting rupture process with the prescribed source model. Furthermore, we address the problem of finding the stable characteristics of the earthquake rupture models that are consistent with the data and of giving an estimate of the variability of each model parameter.

These sensitivity studies allow us to check the resolution and robustness of the nonlinear inversion technique we propose.

2.2 Sensitivity to velocity structure

In this section we study the effects of uncertainty caused by choice of local velocity structure on source resolution, by performing two different synthetic tests.

In order to generate an ensemble of models that efficiently sample the good data-fitting regions of parameter space we use our nonlinear technique, described in previous chapter (see Section1.6). Moreover, we show a method to extract the stable features of the rupture model from the previously generated model ensemble.

We take the fault geometry and station distribution of the 2000 western Tottori earthquake (see Figure2.1) and we construct a fairly complicated target rupture model to generate the synthetic dataset.

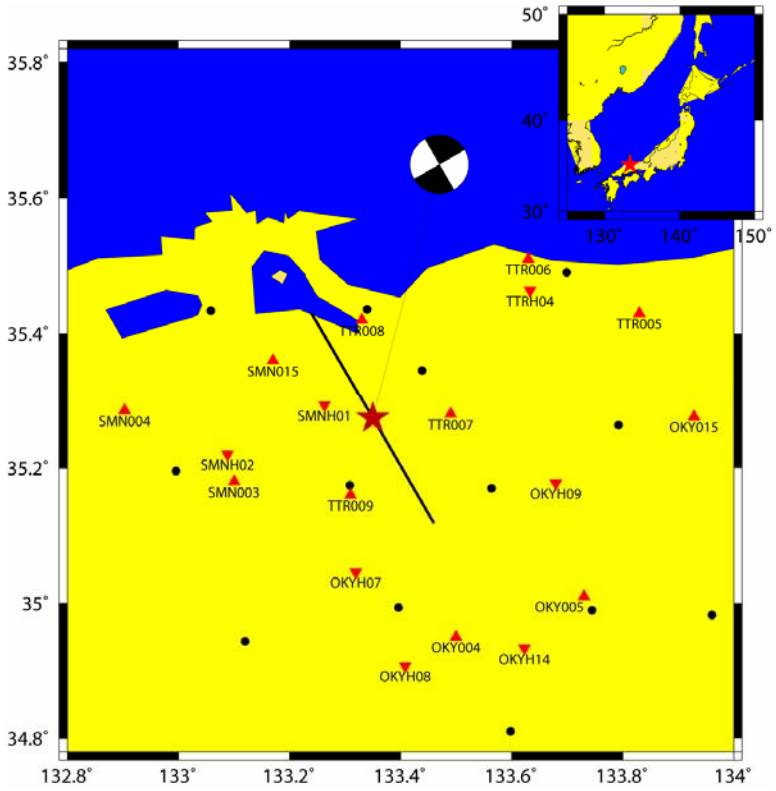

Figure2.1 Map of the fault geometry of the 2000 western Tottori, Japan earthquake. The black solid line represents the fault trace of the plane adopted in this study. Red star indicates the epicenter. Red triangles and inverted triangles represent K-Net (surface sensor) and Kik-Net (borehole sensor) strong motion stations respectively. Black dots represent GPS stations.

The fault has the following geometrical parameters: strike is 150°, dip is 90°, length and width are 40 km and 20 km, respectively; the top of the fault is 0.5 km below the free surface. Slip is concentrated only on two main asperities, A and B (see Figure2.2). Asperity A has a peak slip velocity of 1.45 m/s, rake angle of 45° and a rise time of 3.0 s; asperity B is narrower and extends deeper than A, has 1.5 m/s of peak slip velocity, rake angle of 0° and a rise time of 3.0 s. The rupture front propagates at 2.5 km/s, except in the upper left part of the fault, where it is propagating at nearly 3.5 km/s. We invert simultaneously all parameters at nodal points equally spaced along strike and dip every 4 km. During the inversion, bounds of 0 to 2.5 m/s with 0.25 m/s interval are allowed for the peak slip velocity; the rise time varies from 1 to 4 sec at 0.5 sec interval; the rake angle goes from -45° to 45° by steps of 5°; the rupture time of each grid node is bounded by the times for a rupture to reach the node traveling at 2 and 4 km/s from the hypocenter.

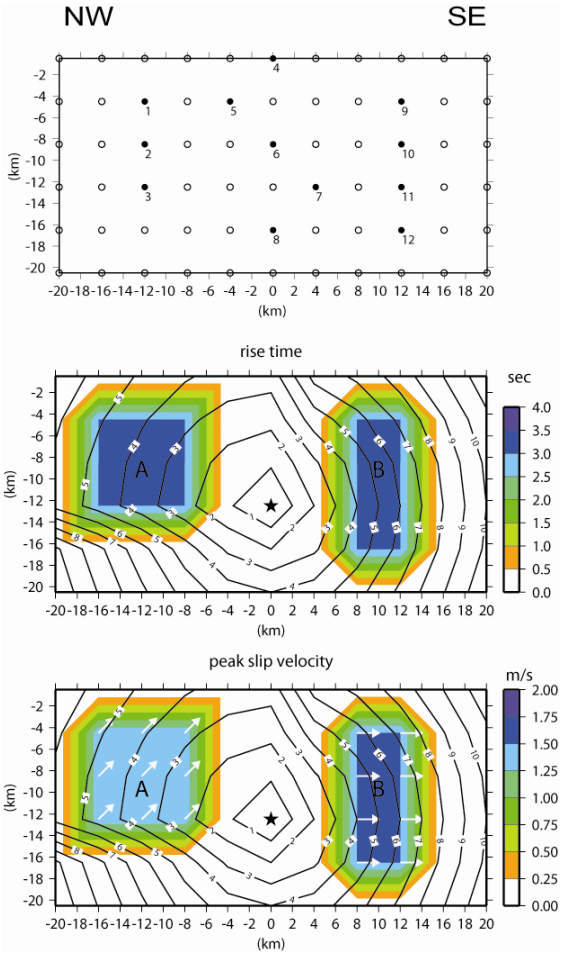

Figure2.2. Target rupture model used for synthetic tests. Horizontal axis is along-strike distance measured from the epicenter. Vertical axis is down-dip distance measured from the ground surface. Top panel shows the grid nodes (open circles) together with the control points used to draw Figure2.6 (solid circles with numbers). Middle panel shows the rise time; rupture time shown by contour lines (in seconds). Bottom panel shows peak slip velocity; rupture time shown by contour lines (in seconds). White arrows represent the slip vector. The slip patches are denoted by capital letters A and B (see text for details).

We perform different inversions adopting different initial random models (multiple restart) . We show the results of noise-free data test (see Section 2.2.1) and of the test obtained by introducing a perturbed velocity structure (see Section 2.2.2).

2.2.1 Noise-free data

Adopting the crustal model listed in Table2.1, we compute synthetic ground velocities in the frequency band 0.05÷0.7 Hz (see Figure2.4a), and we compute horizontal components of static displacement (see Figure2.5a) and use these as

our datasets. During the first stage of the inversion, we generate a model ensemble by exploring about one million rupture models; then, through Eq.(1.20) (see Section 1.6), we compute the average rupture model (Figure2.3a).

Table2.1. Velocity Structure of the Tottori region (DPRI model)*

H (km)	**Vp (km/s)**	**Vs (km/s)**	**d (kg/m^3)**
0	5.50	3.179	2600
2	6.05	3.497	2700
16	6.60	3.815	2800
38	8.03	4.624	3100

* Material properties interpolated linearly between given depths

The inverted model is very similar to the target one; the positions of the two asperities are correctly imaged and the peak slip velocity well estimated.
The rise time is also precisely retrieved and the faster propagation of the rupture front, on the upper left side, is caught fairly well.
Finally, the rake angle of asperity A is very well constrained, whereas we notice some discrepancies in asperity B.
Although similar, the target and inverted models are not identical. Nevertheless the cost function of the inverted model is very low (E=0.007 and E=0.009 for the best and the average model respectively) and the comparison of the waveforms and horizontal displacements reveals (as expected) an almost perfect match between data and synthetics (Figure2.4a and Figure2.5a, respectively).

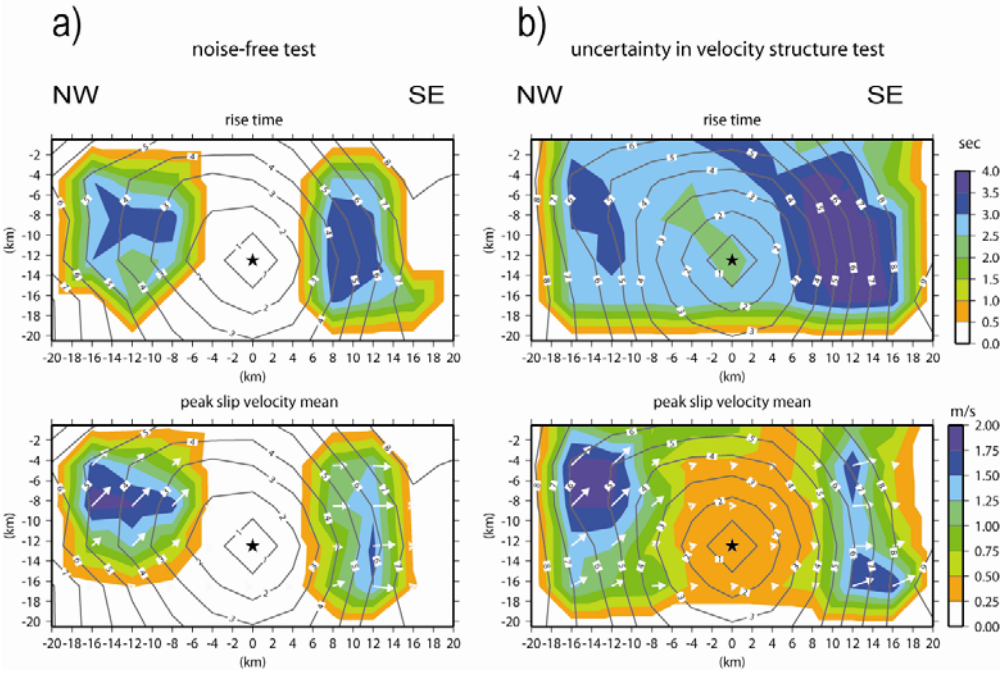

Figure2.3. Inverted rupture model (average model from ensemble inference) from the synthetic tests. a) inversion with noise-free data; b) inversion with crustal structure uncertainty. Top panels show the rise time; rupture time shown by contour lines (in seconds). Bottom panels show peak slip velocity; rupture time shown by contour lines (in seconds).White arrows represent the slip vector .

Considering that the data are noise free, this indicates that the inverse problem is intrinsically non unique. By means of Eq.(1.21) (see Section1.6) we also calculate the standard deviation $<\sigma_i>$ for each parameter of the averaged rupture model.

We take advantage of the perfect knowledge of the target model to assess to what extent the computed standard deviations are good estimates of the true errors; in Figure2.6a we show the value of the parameters of the target and inverted model as well as its standard deviation, taken at some control points (black dots in Figure2.2). We may see that the target model lies within one standard deviation, thus indicating that the standard deviations are slightly large proxies for the true errors.

In Figure2.7a we show the standard deviations on the whole fault plane: in general, the smaller the value of $<\sigma_i>$, relatively to $<m_i>$, the smaller the error.

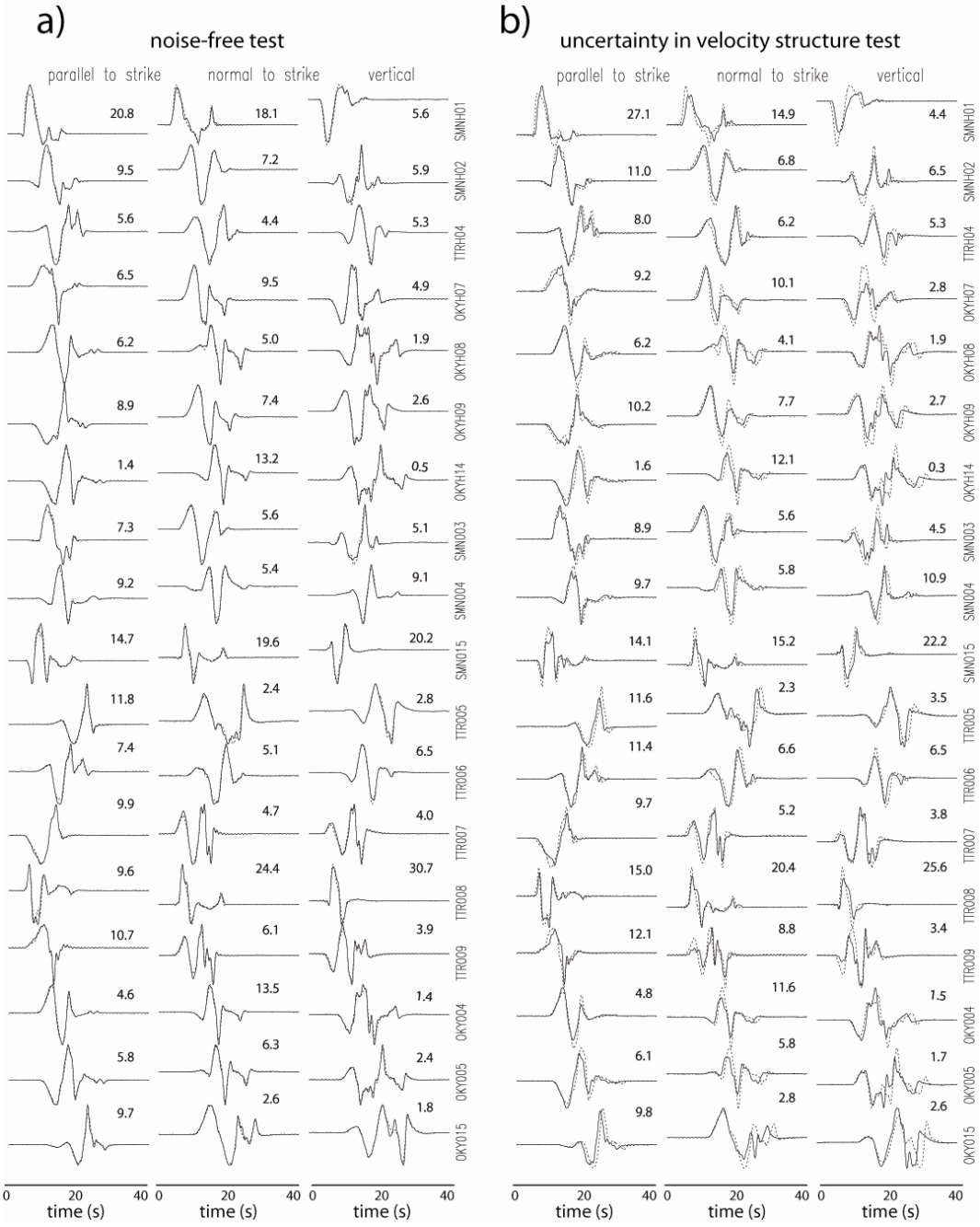

Figure2.4. Comparison of synthetic ground velocities from the target rupture model (solid lines) with the inverted rupture model (dotted lines). Numbers with each trace are peak velocity of the synthetic line (in cm/s). Waveforms are computed in the frequency band 0.05÷0.7 Hz. a) inversion of noise-free data; b) inversion with crustal structure uncertainty.

For this synthetic test, the standard deviations corresponding to the two asperities are very small, thus indicating small error in the model. It should be noted that large standard deviations correlate to zones of the fault with low or no slip; this is not surprising, since those parts of the fault do not contribute to the ground motion and cannot be constrained by the data inversion.

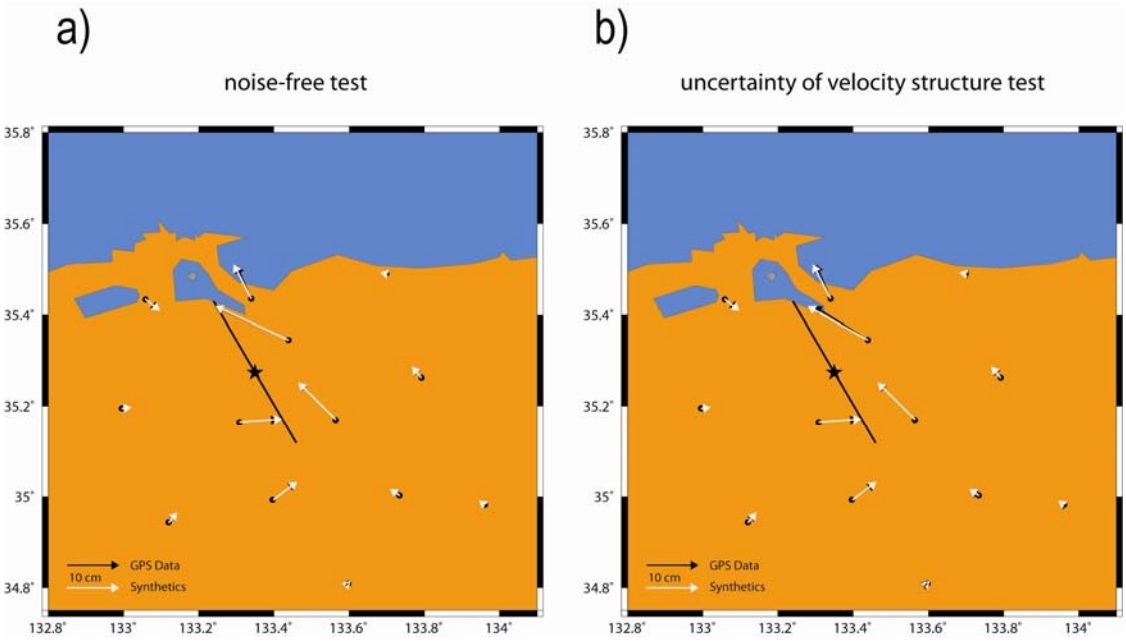

Figure2.5. Comparison of synthetic horizontal displacements from the target rupture model (black arrows) with the inverted rupture model (white arrows).a) inversion of noise-free data; b) inversion with crustal structure uncertainty.

2.2.2 Uncertainty of the velocity structure

Incomplete knowledge of crustal structure could ruin the image of retrieved kinematic rupture models (*Das and Suhadolc*, 1996; *Saraò et al.*, 1998).

In fact the crustal model directly affects the calculation of the Green's functions that are used to compute the ground motion. Here we study the robustness of our method to a reasonable uncertainty in the velocity structure. To this goal we consider two different velocity structures that are listed in Table2.1 (DPRI model) and Table2.2 (PK model). The first is the crustal model used for the hypocenter determination by the Research Center for Earthquake Prediction – Disaster Prevention Research Institute, Kyoto. The second is a modified version, proposed by *Pulido and Kubo* (2004) on the basis of P and S waves velocities measured at shallow depth at several boreholes sites of Kik-Net strong motion network. The two velocity structures differ in the number of layers and in the velocities of both P and S waves, the PK model being about 10% slower than DPRI model. We use the PK model and the target rupture model described in the previous section to compute the synthetic seismograms in the frequency band 0.05÷0.7 Hz and the horizontal component of static displacements representing our virtual dataset.

Table2.2. Velocity Structure of the Tottori region (PK model, *Pulido and Kubo, 2*004)*

H (km)	**Vp (km/s)**	**Vs (km/s)**	**d (kg/m^3)**
0	5.20	3.002	2600
3	5.70	3.290	2700
7	6.00	3.464	2750
16	6.60	3.815	2800
38	6.80	3.926	3100

* Material properties interpolated linearly between given depths

The DPRI model is then used to calculate the Green's functions to be used in the inversion. Throughout the search stage, the inversion algorithm explores about 3 millions rupture models to build up the model ensemble; then, as in the previous test, we make statistical inferences on this ensemble by computing the average rupture model $<m_i>$ and the corresponding standard deviation $<\sigma_i>$. The cost function for the best and the average model is E=0.1 and E=0.14 respectively. The inverted model (Figure2.3b) still shows two distinct patches, with peak slip velocity and rise time respectively of the order of 1.5 m/s and 2.5 s. The rake angle seems to be robustly inverted, especially over asperity A and the rupture times still show a faster propagation in the upper left side of the fault, though it is less evident than in the previous test. However, both asperities are smeared, and in particular the slip is significantly increased at very shallow depth. This confirms some of the results proposed by *Ji et al.* (2002), who find that the near-surface slip estimate is strongly affected by the velocity structure. Furthermore we note that the two slip patches are somewhat mislocated; this feature is more evident for asperity B, which is shifted to the right by about 2 km.

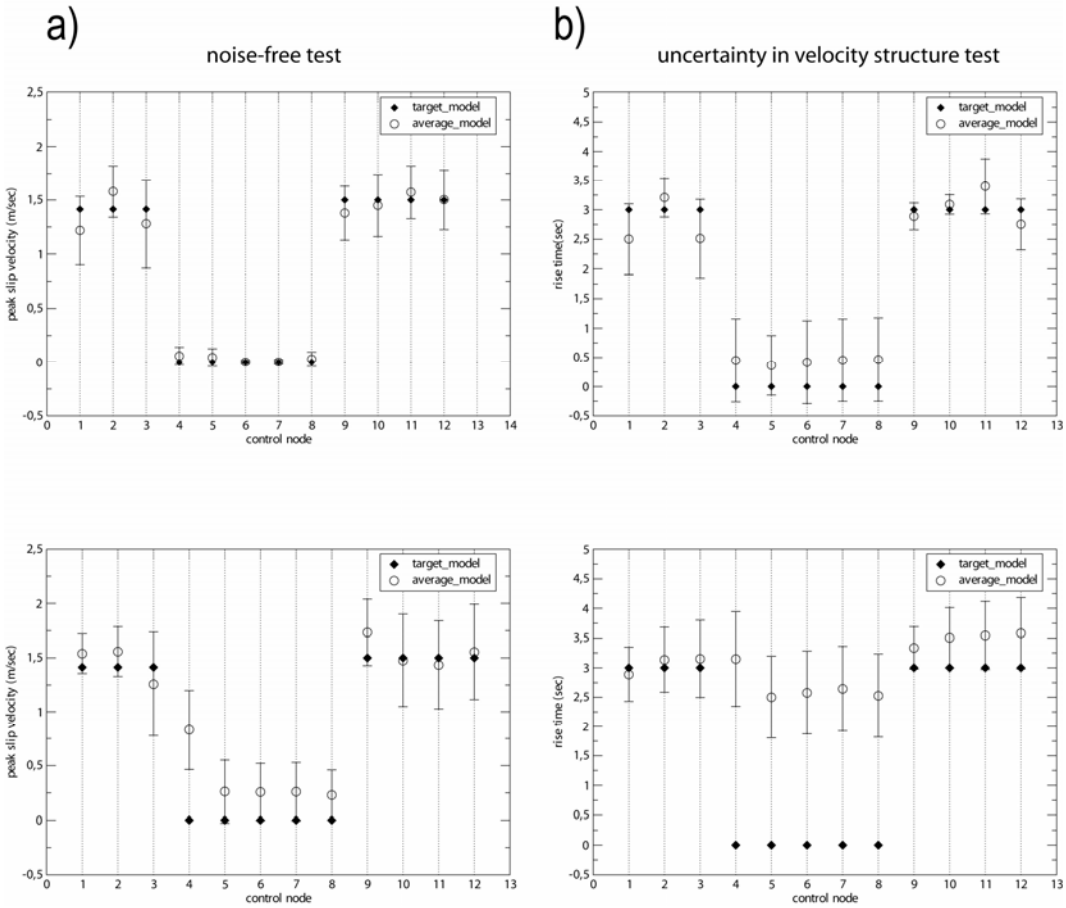

Figure2.6. Comparison of peak slip velocity (upper panels) and rise time (lower panels) for the target and inverted rupture models. Numbers along the abscissa indicate the control points shown in Figure2.2. Vertical bars represent ± one standard deviation. a) inversion with noise-free data; b) inversion with crustal structure uncertainty.

The uncertainty in the velocity structure increases the nonuniqueness of the inverse problem, i.e. instead of only one solution we have many rupture models that are consistent with the data. This reflects on the averaged rupture model of Figure2.3b for instance, differently from what we have found in the previous noise-free test, now the model solution shows a low to intermediate amount of slip distributed between the two patches. This means that many models, with a diffused slip on the fault plane, are still consistent with the data (Figure2.4b and Figure2.5b). Errors in the velocity structure also increase the standard deviation of the averaged model (Figure2.6b); in this case the target model lies between one standard deviation only in those regions characterized by large slip. From Figure2.7b we may also see a global decrease of the resolution with respect to the noise-free case study.

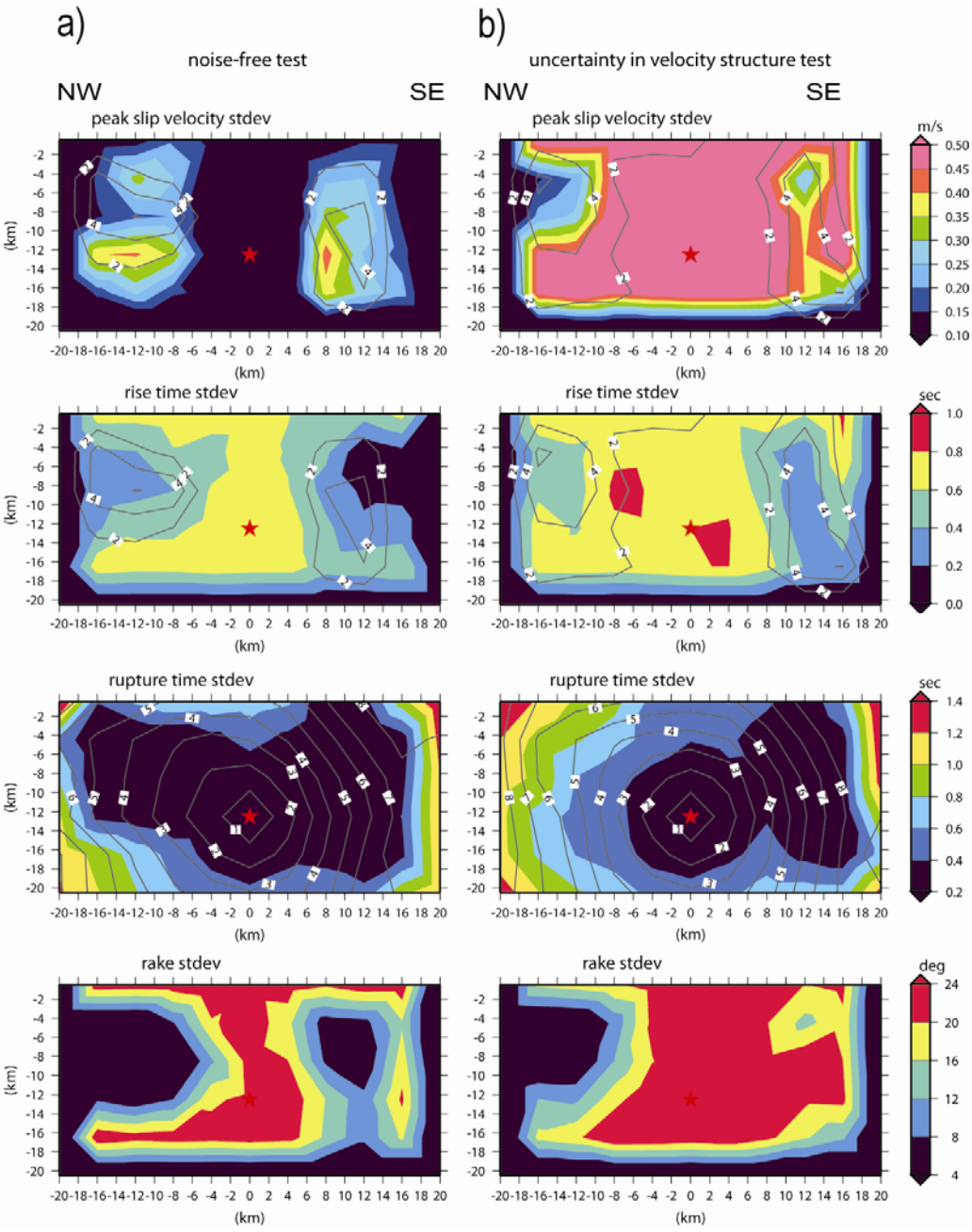

Figure2.7. Standard deviations of average model, computed through ensemble inference; contour lines represent total slip displacement in meters, but in third row panels where rupture times (in seconds) are plotted instead; a) inversion with noise-free data; b) inversion with crustal structure uncertainty.

It seems that the computed standard deviations are good estimates of actual error when the Green's functions are sufficiently accurate, and that the computed standard deviations will underestimate the true error when inaccurate Green's functions are used. The standard deviations may be seen as bounds that delineate a consistency region of the rupture model.

2.3 Importance of source time function

In an inversion scheme the temporal evolution of slip on the fault plane is obtained either by adopting an *a priori* analytical expression for the source time function (single window approach) or by assuming that each fault point can slip more than once (multi window approach). The single window approach permits the adoption of different functional forms of source time function (STF) to image the rupture history on a finite fault.

In this section we study the importance of the source time function to retrieve kinematic source models on a finite fault. In order to discuss how the choice of the source time function can bias the retrieved kinematic rupture histories, we present the results of four different inversion synthetic tests. As in the previous study**,** we consider the fault geometry and station distribution of the 2000 western Tottori, Japan, earthquake (Mw 6.6). We select 18 accelerometric stations and 13 GPS locations (shown in Figure2.1). To obtain a more realistic source characterization we construct a fairly complicated target rupture model (see Figure2.8). The fault has the following geometrical parameters: strike is 150°, dip is 90°, length and width are 40 km and 20 km, respectively; the top of the fault is 0.5 km below the free surface. Slip is concentrated only on two main asperities, A and B. Asperity A has a slip of 0.8 m and a rise time of 2.5 s; asperity B has a displacement of 1 m and a rise time of 2.5 s. The rupture front propagates at 2.5 km/s, except in the upper left part of the fault, where it is propagating at nearly 3.5 km/s.

We adopt the crustal model, listed in Table2.2, obtained by overlapping the velocity structure of the Tottori region (DPRI, 2000) with the KiK-Net borehole information (*Pulido and Kubo*, 2004).

We assume the same basic form of the slip velocity time-function in all subfaults, that is a regularized Yoffe (see Eq.(1.11c) in Section 1.6) characterized by a T_{acc} equal to 0.225 s (see Figure2.9). The resulting peak slip velocity distribution is shown in Figure2.8 (bottom panel): asperity A has a peak slip velocity of 1.45 m/s and a rake angle of 45°; while asperity B has 1.5 m/s of peak slip velocity and rake angle of 0°.

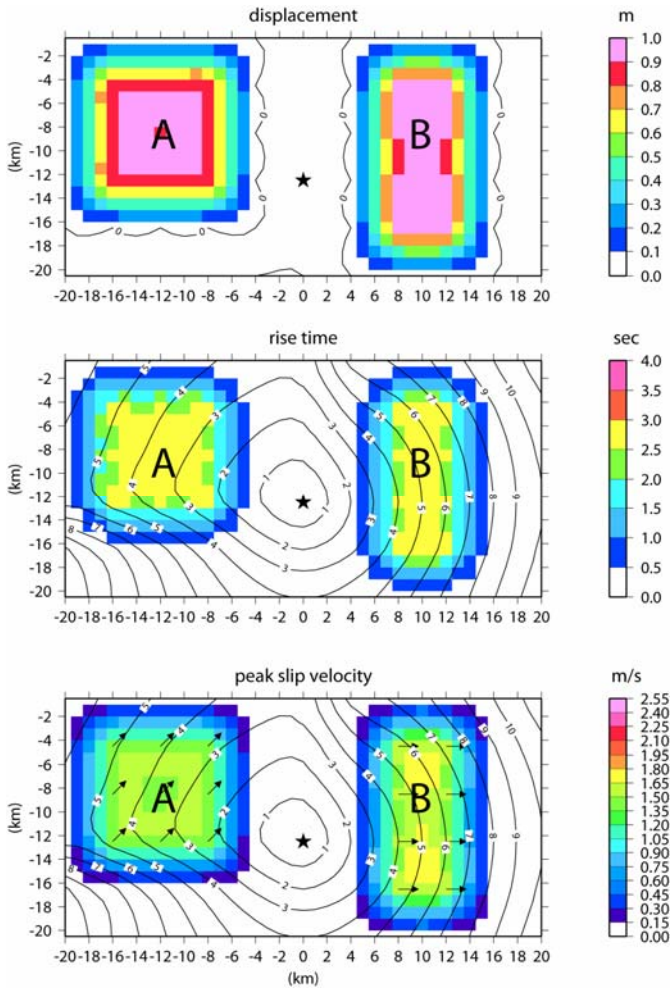

Figure2.8. Target rupture model. Horizontal axis is along-strike distance measured from the epicenter. Vertical axis is down-dip distance measured from the ground surface. Top panel shows the total slip; rupture time shown by contour lines (in seconds). Middle panel shows rise time; bottom panel displays peak slip velocity. The slip patches are denoted by capital letters A and B (see text for details).

We generate synthetic seismograms in the frequency band 0.05÷0.7 Hz and we associate the horizontal component of static displacements to synthetic GPS data and use these as our virtual dataset. To assess how the selection of a given functional form of source time function affects the imaged rupture process, we perform four different kinematic inversions, adopting four different STFs: a boxcar (we call this *Test Y_B*), a modified cosine (we call this *Test Y_C*), and two regularized Yoffe functions with T_{acc} of 0.225 s (we call this *Test Y_Y*) and 0.400 s (we call this *Test Y_Y0.4*), respectively (see Figure2.9). All the adopted source time functions are described in Section 1.6 (see Eq. (1.11a)-(1.11b)-(1.11c)). We invert simultaneously for peak slip velocity, rupture time, rise time and rake angle.

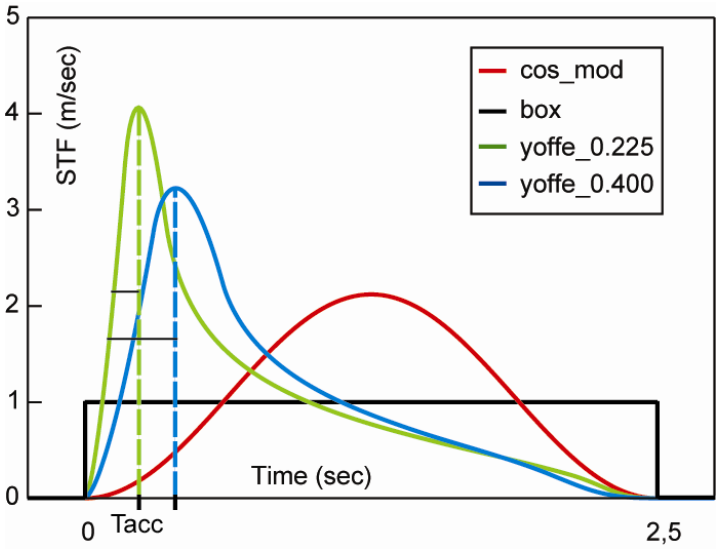

Figure2.9. Slip velocity functions used in this study. See legend for the different adopted STFs.

2.3.1 Results: Kinematic parameters

For each inversion, the algorithm explores about one million rupture models, finds the best fitting model and calculates the weighted average model $< m_i >$ (see Eq.(1.20)) and the corresponding standard deviation $< \sigma_i >$ (see Eq.(1.21)). In Figure2.10 we compare the kinematic source parameters inferred from the four different inversions. The slip distribution is not directly retrieved from the inversion, but it is computed through the inferred peak slip velocity and rise time values. Looking at the slip on the fault plane (upper panel), we observe that the different STFs tend to retrieve a slip distribution similar to the target one, especially in terms of maximum slip values rather then in shape. These results are confirmed by the retrieved total seismic moment, constrained through the inversion of geodetic data, which is very close to the target seismic moment (M_t = 0.696×10^{19}Nm) for all the STFs (Figure2.11). However, even if all the inverted models have slip distribution similar to the target one, some of them are characterized by very different rise time and peak slip velocity distributions (middle and bottom panel of Figure2.10).

For all four inversions the weighted average model shows two asperities of slip velocity, whose shape and dimensions strongly depend on the adopted STF.

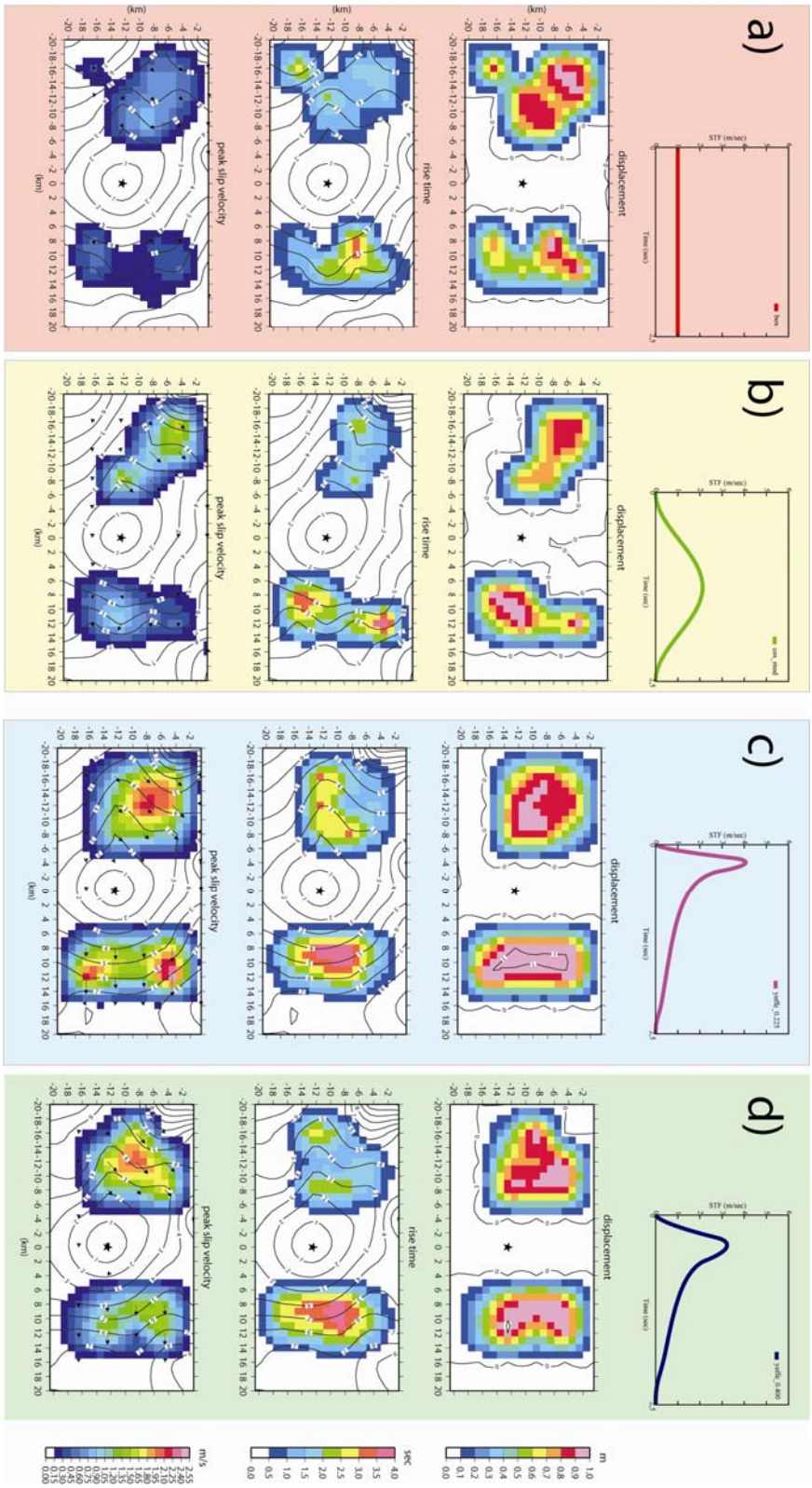

Figure2.10. Inverted rupture models (average model from ensemble inference) from the four synthetic tests performed with: a) a boxcar; b) a modified cosine; c) a regularized Yoffe with T_{acc} =0.225s; d) a regularized Yoffe with Tacc=0.400s. For each STF: top panels show the displacement on the fault; middle panels show the rise time; bottom panels show the peak slip velocity. Rupture time is shown by contour lines. Arrows represent the slip vector.

Besides, the amplitudes of the peak slip velocity and the rise time on the fault drastically vary with STFs.

When the adopted STF differs from that used to generate the synthetic datasets (see Figure2.10a, 2.10b, 2.10d) both asperities are smeared, in particular for the boxcar (Figure2.10a).

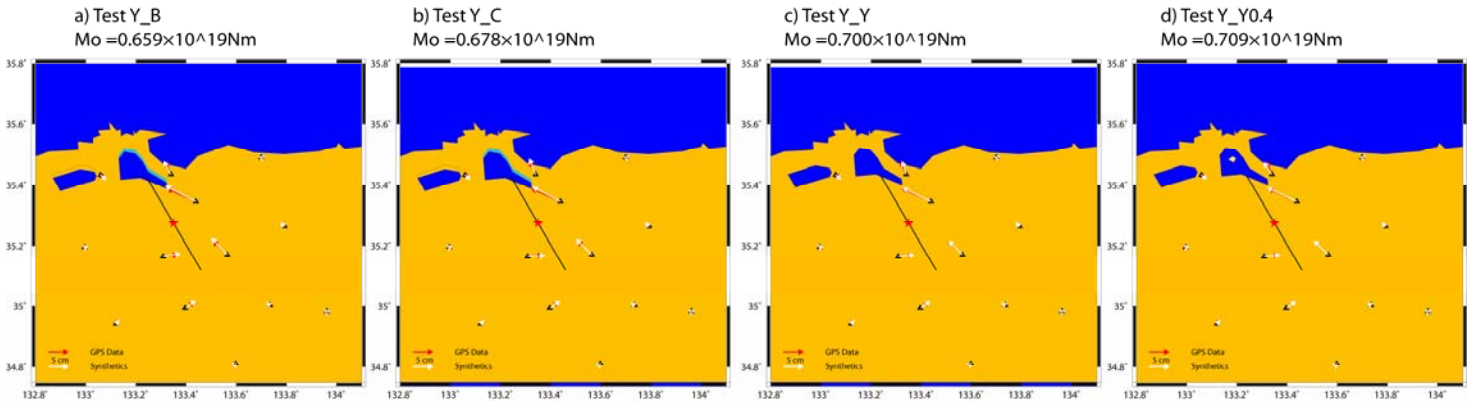

Figure2.11. Comparison of synthetic horizontal displacements from the target rupture model (red arrows) with inverted rupture model (white arrows) for each test performed with: a) a boxcar; b) a modified cosine; c) a regularized Yoffe (T_{acc} =0.225s); d) a regularized Yoffe (Tacc=0.400s). For each inversion it is displayed the recovered seismic moment value.

The comparison of the waveforms, for the nearest and furthest station, reveals an almost perfect match between data and synthetic for inversion with the same source time function used to generate the synthetic dataset (Figure2.12c), while the match get slightly worse when we introduce an inaccurate knowledge of the source time function in the inversion.

These behaviors show the intrinsic non uniqueness of the inverse problem that increases due to an inadequate choice or, in general, to an inaccurate knowledge of the source time function, i.e. instead of only one solution we could have many rupture models that are consistent with the data.

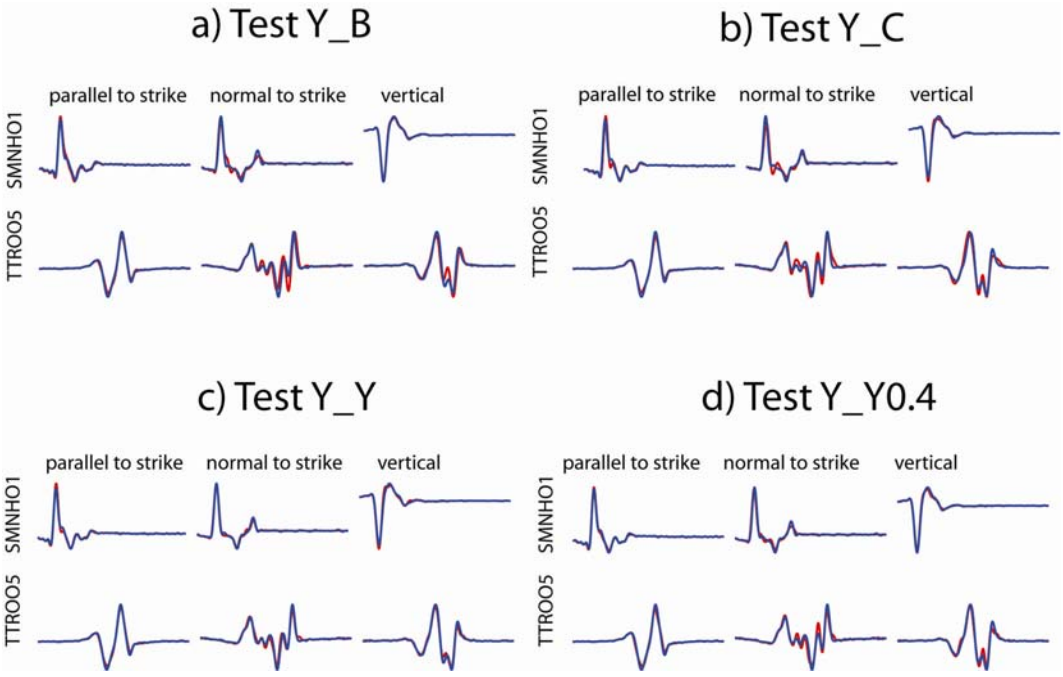

Figure2.12. Comparison of synthetic ground velocities from the target rupture model (blue lines) with inverted rupture model (red lines) for each test performed with: a) a boxcar; b) a modified cosine; c) a regularized Yoffe with T_{acc} =0.225s; d) a regularized Yoffe with T_{acc} =0.400s. Comparison it's showed for two strong motions stations located at different epicentral distance d=8 km (SMNH01) and d=47 km (TTRO05).

In Figure2.13 are shown the distributions of the coefficient of variation for the peak slip velocity (bottom panels) and rise time (top panels). The coefficient of variation is computed as the ratio between the standard deviation of the parameter's distribution and its mean (*Ventsel*, 1983). The coefficient of variation allows us to give a measure of the relative dispersion of each single parameter around its mean distribution, on the whole fault plane (*Liu et al.*, 2006a). Moreover it is a useful statistic parameter for comparing the degree of variation from one parameter series to another, even if the means are drastically different from each other (*Taylor et al*., 1999).

The four rupture models show significantly different mean values of rise time and peak slip velocity (see Figure2.10, middle and bottom panel, respectively), while the corresponding distributions of coefficient of variation (see Figure2.13) give a quite similar variability.

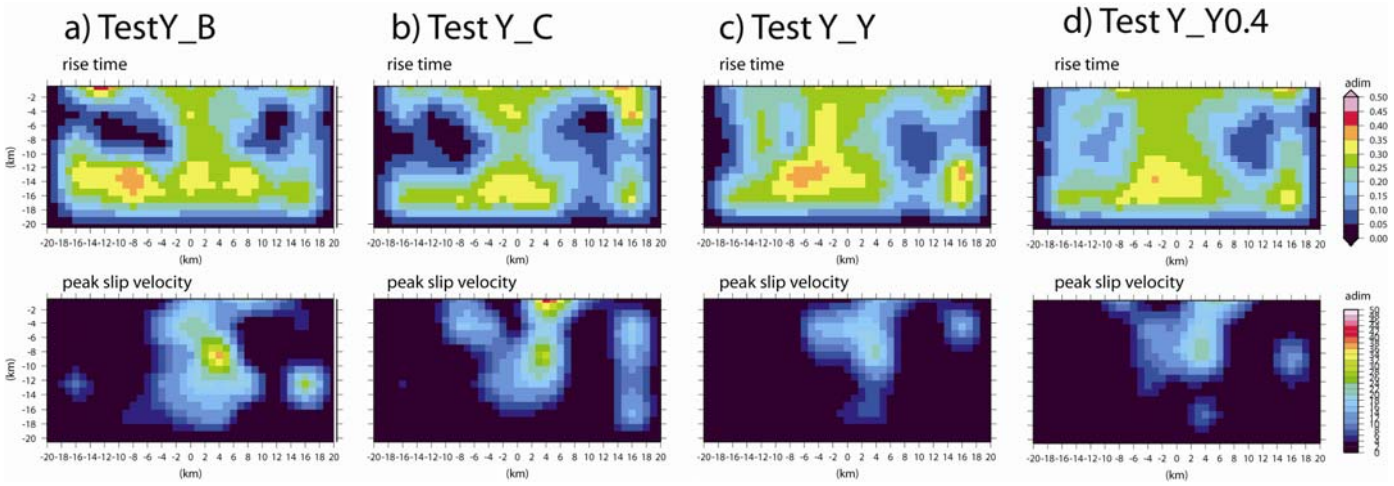

Figure2.13. Coefficient of Variation of average models, computed through ensemble inference. For each synthetic test performed with: a) a boxcar; b) a modified cosine; c) a regularized Yoffe with T_{acc} =0.225s; d) a regularized Yoffe with T_{acc} =0.400s, top panels show the coefficient of variation of rise time; bottom panels show the coefficient of variation of peak slip velocity.

For each case it should be noted that large coefficients of variation are correlated to regions of the fault with a small amount of slip; this is obvious, since those areas do not contribute to the ground motion and cannot be constrained by the inversion.

This approach allows us to assess the spatial resolution and reliability of a solution and it indicates which are the well resolved areas of the fault where the distinct parameters are well constrained.

2.3.2 Results: *Trade-off*

In a finite-fault slip inversion scheme, any study that attempts to investigate the effects of model parameters one at a time, inevitably leaves out the question of their complex interaction (*Beresnev*, 2003). Guatteri and Spudich (2000) proposed a study on the resolution of dynamic parameters (strength excess and slip-weakening distance), underlining the importance to address issues of parameter interactions and unknown trade-offs in an inversion approach. From our study it comes out that the choice of STF strongly affects the inverted rupture model, especially in terms of peak slip velocity and rise time. It is worthy of noting that different models (Figure2.10) have a similar slip distribution, but they have very different peak slip velocity and rise time distributions, probably due to the

existence of a *trade-off* between these two parameters in controlling the rupture process. In order to extract a quantitative measure of this interaction we calculate, for the entire ensemble of models, the resulting correlation and covariance matrices. These latter indicate how the model parameters affect one another. In particular, the covariance of two variables can be defined as their tendency to vary together and it provides the joint variability of the two parameters around their mean distribution. Following the work of Sen et al. (1993), and Sambridge (1999b), we compute the covariance matrix:

$$\Sigma_M = \frac{\sum_{i=1}^{N_d} \left(\mathbf{m} - <\mathbf{m}>\right)_i \left(\mathbf{m} - <\mathbf{m}>\right)_i^T / E_i(\mathbf{m})}{N_d \sum_i 1/E_i(\mathbf{m})} \tag{2.1}$$

where, **m** is the model vector associated to the *i*-th parameter, $E(\mathbf{m})$ is the energy function associated to the model vector and N_d is equal to $N_g \times N_p$. N_g is the number of grid points, in which we subdivide the fault plane, and N_p is the type of kinematic parameters that we retrieve in our inversion (rupture time t_R, rise time τ_R, peak slip velocity and rake). We indicate with $\left[Cov(\Sigma)\right]_{ij}$ a generic element of the covariance matrix Σ_M. The diagonal of the covariance matrix is formed by the variance of parameters. The off-diagonal elements represent the joint variability (interaction) between two different kind of parameters belonging to the same or to different grid nodes. Since the parameters differ in type and dimension it is complicated to directly show the covariance matrix (*Sambridge*, 1999b*)*. To achieve a more direct indication of how two parameters co-vary, we scale covariance matrix to obtain correlation matrix whose elements are given by:

$$C_{ij} = \left[Cor(\Sigma)\right]_{ij} = \frac{\left[Cov(\Sigma)\right]_{ij}}{\left[Cov(\Sigma)\right]_{ii}^{1/2} \left[Cov(\Sigma)\right]_{jj}^{1/2}} \tag{2.2}$$

where the subscript *i*-th and *j*-th refer to a couple of parameters.

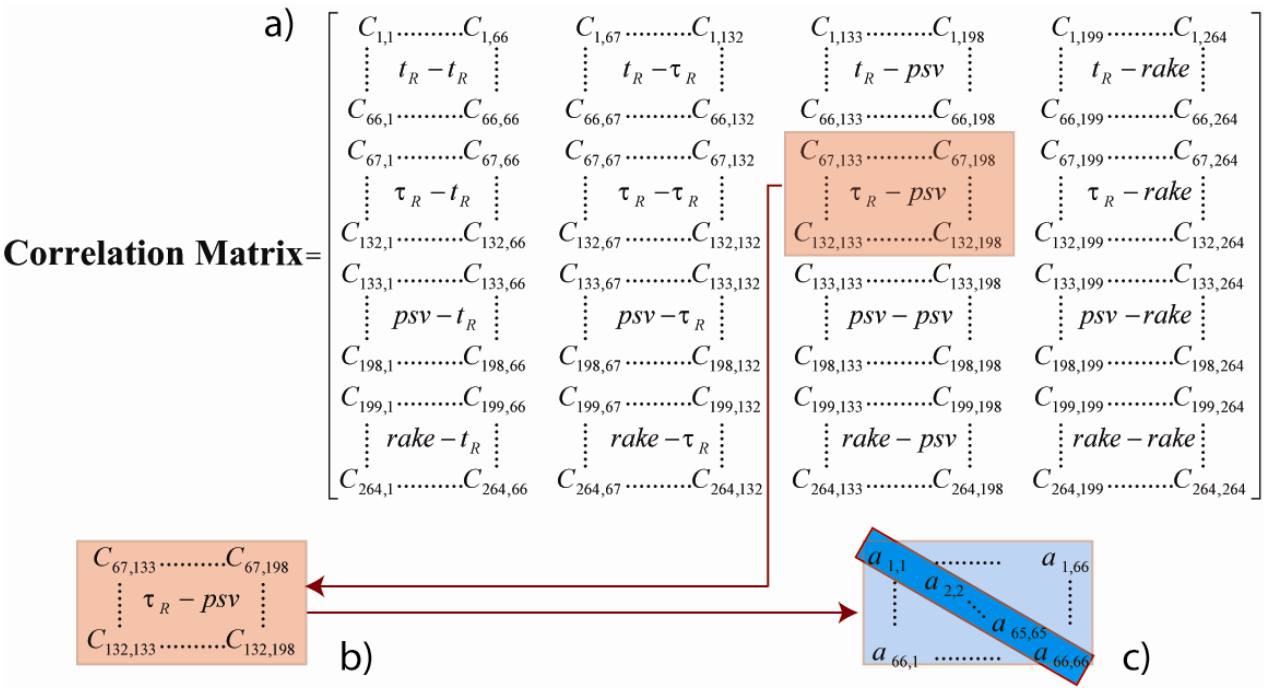

Figure2.14. Correlation matrix scheme: a) entire 264×264 correlation matrix, formed by 16 sub-matrices (all possible couple's parameter combination); b) extraction of the 66×66 sub-matrix corresponding to the peak slip velocity and rise time couple; c) diagonal elements of the extracted sub-matrix (representing the trade-off between peak slip velocity and rise time belonging to the same grid node on the fault plane).

How we can see in Figure2.14a, we obtain a 264×264 symmetrical model correlation matrix, formed by 16 sub-matrices (all possible couple's combination of parameters); each of them is a matrix of size 66×66. For a given sub-matrix associated to a given couple of parameters (i.e. peak slip velocity-rise time), each element C_{ij} represents the correlation between all possible couple's values those parameters can assume on every grid node (tot 66). Many features characterize the entire matrix, too numerous to consider in detail. We focus our attention on the interaction between peak slip velocity and rise time. For this purpose, we extract the sub-matrices (66×66) of the selected couple of parameters (Figure2.14b) and we examine its diagonal elements (Figure2.14c); these latter represent the *trade-off* between peak slip velocity and rise time belonging to the same grid node on the fault plane. In Figure2.15 we show the distribution of correlation coefficient between peak slip velocity and rise time on the fault plane, for each performed synthetic test. Leaving out of consideration the choice of STF, we always observe

negative correlations. This trend shows that exists a negative *trade-off* between peak slip velocity and rise time indicating that if one parameter tends to increase the other decreases with respect to its mean.

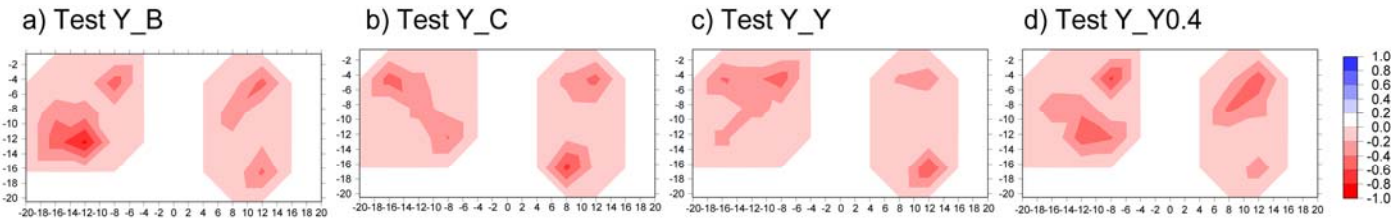

Figure2.15. Distribution of correlation coefficient between peak slip velocity and rise time, on the fault plane, for each synthetic test performed with: a) a boxcar; b) a modified cosine; c) a regularized Yoffe with T_{acc} =0.225s; d) a regularized Yoffe with T_{acc} =0.400s.

This aspect is very important to assess the resolution of retrieved kinematic parameters and it should be taken into account in an inversion scheme. The approach proposed here is only one route by means we would try to address the correlation problem.

Further investigations are needed to better interpret the *trade-off* between model parameters. In general, much effort should be devoted to the problem of analyzing the resulting ensemble of inverted rupture models in a quantitative way.

2.3.3 Results: *Bias*

Finally, in this section, we want to quantitatively study the *bias* on the retrieved models introduced by the a priori assumption of a particular STF.

We use the term '*bias*' to indicate how an erroneous choice or inaccurate knowledge of the source time function can produce a not-well retrieved rupture process with respect to the target model. First, considering all rupture models explored by our algorithm, we evaluate, for each kinematic parameter, the weighted residual between the retrieved model and the corresponding target value, normalized to the target itself. This quantity represents the distribution in percentage of the residual (we call it *res*):

$$res_{jk} = \frac{\frac{1}{E_j}\left(\sum_{i=1}^{N} \frac{m_{ij} - t_i}{t_i}\right)}{\sum_{j=1}^{M} \frac{1}{E_j}} \tag{2.3}$$

where *k* refers to the kinematic parameter (peak slip velocity, total slip, rise time, rupture time and rake). In Eq.(2.3) m_{ij} represents the value of the parameter assumed on the *i*-th grid-node of the *j*-th model belonging to the ensemble Ω, *M* is the number of rupture models explored by the algorithm and *N* is the number of grid nodes on the fault plane. The weight is the same used to compute the average model and its standard deviation and it corresponds to the inverse of the cost function (E_j). In this way, for each inversion, we are able to provide a quantitative measure of parameter's dispersion between the target and the retrieved model. In Figure2.16 are shown the histograms of the residual for each synthetic test (displayed along columns a), b), c), d)) and for all kind of parameter: total slip (Dmax), peak slip velocity (PSV), rise time, rupture time and rake (displayed along rows 1), 2), 3), 4), 5)). To better understand the bias due to the choice of the STF we calculate, for each performed synthetic test, the mean and standard deviation values associated to each parameter's distribution. The mean value of each distributions, shown as a red bar in Figure2.16, tells us to what extent each single retrieved kinematic parameter under/over-estimates the target one.

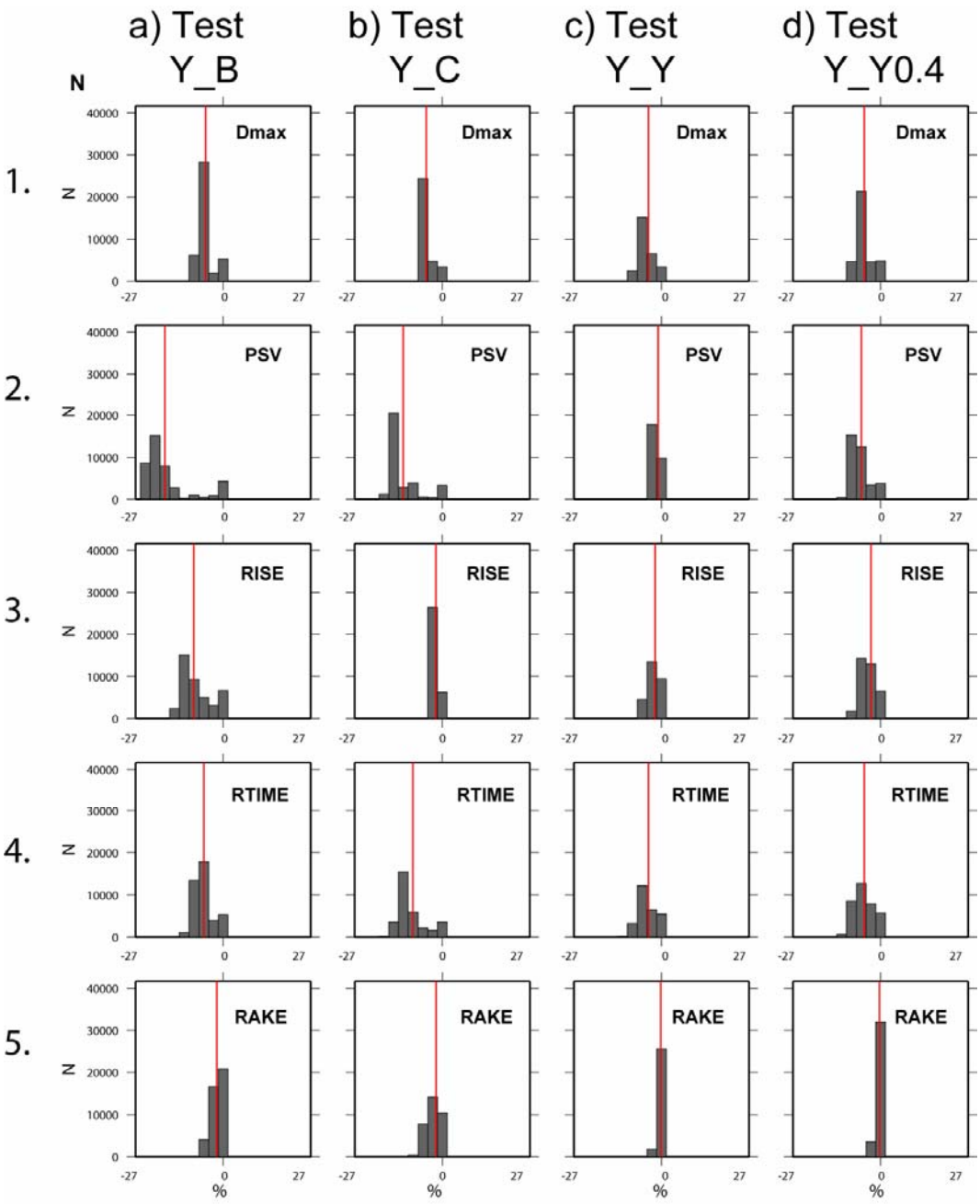

Figure2.16. Residual's distributions for each synthetic test performed with: a) a boxcar; b) a modified cosine; c) a regularized Yoffe (T_{acc} =0.225s); d) a regularized Yoffe (T_{acc} =0.400s), (displayed along columns), and for all kind of parameter; slip, peak slip velocity, rise time, rupture time and rake (displayed along rows 1), 2), 3), 4), 5). The red bar indicates the mean value of each distribution.

Table2.3 collects, for each test performed, the mean value and its corresponding standard deviation computed for all kinematic parameters:

1. the bias clearly decreases as the STF adopted in the inversion approaches to that used to generate the synthetic dataset;
2. in all case, the total slip residual's distribution is centered around values near to zero (see row 1) in Figure2.16 and column I) in Table2.3). This behavior is in agreement with the results discussed in Section 2.3.1 about the computed slip displacement over the fault plane;
3. it is worthy of noting that for similar distributions of slip's residual, different STFs yield very different distributions in terms of peak slip velocity and rise time (row2 and row3 in Figure2.16). Synthetic test in which we have adopted the boxcar STF to invert the dataset, gives peak slip velocity and rise time under-estimated of about 18% and 8%, respectively (see row1), column II) and III) in Table2.3). In the case of the cosine function, peak slip velocity and rise time are under-estimated of about 12% and 2% respectively (see row2), column II) and III) in Table2.3). For the Yoffe with T_{acc} =0.225 s, we have an under-estimate of 1.0 % and 1.5 % for peak slip velocity and rise time, correspondingly (see row3), column II) and III) in Table2.3). Finally, for the Yoffe with T_{acc} =0.400 s, peak slip velocity and rise time are under-estimated of about 6% and 3%, respectively (see row4), column II) and III) in Table2.3);
4. for rupture time (see row 4) in Figure2.16 and column IV) in Table2.3), it is interesting to note that the rupture caused by a cosine function is faster than the rupture generated by a boxcar;
5. the rake's residual distribution shows, in each synthetic test, a quite similar trend (see row 5) in Figure2.16 and column V) in Table2.3).

Table2.3. Mean and standard deviation of the residual's distributions shown in Figure2.16.

	I. Dmax	II. PSV	III. Rise Time	IV. Rupture Time	V. Rake
Test a) Y_B	(-5 ± 2) %	(-18 ± 7) %	(-8.0 ± 4.5) %	(-6.0 ± 3.0) %	(-2.0 ± 1.7) %
Test b) Y_C	(-4 ± 2) %	(-12 ± 4) %	(-2.0 ± 1.5) %	(-9.0 ± 4.3) %	(-2.0 ± 2.1) %
Test c) Y_Y	(-3 ± 2) %	(-1± 1.1) %	(-1.5 ± 1.7) %	(-2.5 ± 3.0) %	(-0.3 ± 0.6) %
Test d) Y_Y0.4	(-4 ± 2) %	(-6± 2.8) %	(-3.0 ± 2.5) %	(-5.0 ± 3.5) %	(-0.4 ± 0.7) %

This approach allows us to assess how the choice of the STF can bias the imaged kinematic rupture histories.

From the obtained results we can argued that the retrieved pattern of kinematic parameters are biased by the representation of the adopted source time functions.

2.4 Discussion

Inverting for source rupture process with a limited knowledge of the Earth structure and of the source time function certainly proves challenging; in these cases the details of the rupture process could remain hard to retrieve.
Incremental improvements in resolving for source complexity will be possible with the extensive deployments of modern geodetic and seismic networks combined with space-based observations, but additional advances in the inversion process will also be helpful.

In this chapter, we have applied an original method to solve the finite-fault nonlinear inverse problem, which consists of retrieval of the complete rupture history on a finite fault using seismic and geodetic data jointly. This problem, owing to azimuthally gaps in the station distribution, limited frequency bandwidth, uncertainty of the crustal structure, site effects and fault parameterization, is known to have non-unique solutions. In their conclusion, *Liu and Archuleta* (2004) state that "a prudent approach is to use each Earth model that is available to deduce the range of possible faulting models and look for the elements that are common to the different Earth models". Our procedure directly implements such a strategy, since the a posteriori ensemble inference is conceived to extract the most stable features of the earthquake rupture that are consistent with the data, rather than simply searching for the best model. In this chapter we have checked the robustness and the resolution' capability of our inverse technique by performing different synthetic tests. In particular we have focused on two main sources of uncertainty in finite-fault inversion, namely the choice of the Earth model to compute the Green's functions and the adoption of the source time function.

First, we have analyzed and discussed the sensitivity of kinematic inversion to crustal model, providing a quantitative measure of the effects of velocity structure on source resolution. We have shown that an inaccurate velocity structure could strongly bias the inversion results.

Then, we have emphasized the effect of uncertainty caused by the choice of source time function on retrieving kinematic source parameters. According to our results, the inferred rupture history could also be biased by the adoption of the source time function.

Therefore, inferences based on incorrect assumptions about velocity structure and source time function could lead to erroneous results, introducing artifacts and biases.

The important conclusion of this chapter is that the effects of uncertainty factors on source resolution are crucial to assess the reliability of an inversion procedure and must be taken into account and carefully analyzed.

The guidelines we propose are based on the model ensemble inference, which allows us to appraise the robustness of the results and to estimate the variability of rupture models that are consistent with the data. In particular we may evaluate lower and upper bounds for some source parameters, such as peak slip velocity and rupture speed. This may have important implications, for instance for ground motion prediction through ground shaking scenarios.

We believe that the appraisal stage in nonlinear inversion is as important as the search for the best model. This appraisal should be further developed and become a common practice in finite-fault nonlinear inversion studies.

Chapter 3

Application to real earthquakes

3.1 Introduction

Detailed mapping of spatial and temporal slip distribution of large earthquakes is one of the principal goals of seismology.

Earthquake source processes are very complex at all scales. In the past two decades, well-recorded earthquakes, such as the 1992 Landers earthquake, the 1995 Kobe earthquake, the 1999 Chi-Chi earthquake, the 2000 Tottori earthquake, the 2004 and 2007 Niigata earthquakes, give seismologists the opportunity to investigate the source process in detail.

The recordings of an earthquake provide us a unique opportunity to construct detailed and physically realistic models of the rupture history and wave propagation for an earthquake. Unfortunately, the study of earthquake physics is constrained by the inability to measure coseismic slip everywhere on the fault during the rupture process. In order to resolve the seismic source in greater details, it is necessary to use data from the near-source region (*Beroza and Spudich*, 1988). Seismic records in the epicentral region are the most reliable source of information on the history of a rupture and on the time function that describes locally the slip on a fault. Indeed, high quality records of ground motions have demonstrated that fault rupture during large earthquakes is nonuniform both in space and time (*Fukuyama and Irikura*, 1986).

The understanding of heterogeneity of the fault rupture process has important consequences not only for the nature of the seismic source but also for the strong ground motion prediction in order to mitigate seismic disaster from future large earthquakes. However, seismograms carry information not only about the rupture process, but also about the material crossed by the waves from the source to the observation point (path effects). In addition, seismograms are contaminated by reverberations and non linear effects close to the surface (site effects).

Isolating the desired information on the source is a nontrivial task.

Therefore, a good quality and dense network of stations recording an earthquake is invaluable.

Today, in several place around the world, the improvement of seismic observational techniques and networks near major faults makes possible the collection of high-quality data near to the source. Extensive portable instrument deployments following the mainshock for recording aftershocks provide calibration data for constraining the regional velocity structure and, ultimately, for better understanding the mainshock strong motions (*Wald et al*., 1996).

Slip distributions on faults have been estimated for several large earthquakes using different datasets and several approaches have been developed to model the spatial and temporal rupture processes of an earthquake source over a finite fault (e.g., *Archuleta*, 1982; *Hartzell and Heaton*, 1983; *Beroza and Spudich*, 1988; *Wald and Heaton*, 1994; *Ide et al*., 1996; *Yoshida et al*., 1996; *Zeng and Anderson*, 1996; *Sekiguchi et al*., 2000; *Dreger and Kaverina*, 2000; *Ji et al*., 2002; *Bouchon et al*., 2002; *Belardinelli et al*., 2003b; *Salichon et al*., 2004; *Piatanesi et al*., 2007).

By taking advantage of recent development in geodetic observation, some of those studies combined Global Positioning System (GPS), teleseismic, and strong motion datasets to better constrain the rupture history through inverse modeling. The GPS data, combined with field observations of the ruptures and aftershocks locations have been extremely useful to determine the spatial distribution of slip on the faults.

Recent studies have shown the benefit of combining geodetic and seismic data in source inversion. Wald and Heaton (1994) found that the addition of the geodetic data to the strong-motion and teleseismic data in the analysis of the 1992 Landers earthquake added important constraints on the rupture evolution. The addition of the geodetic datasets improves the spatial coverage of the near-field region. As geodetic measurements are static displacements, they complement the frequency range provided by the seismic dataset and spatially constrain the rupture process, allowing the seismic data to better resolve the temporal heterogeneity (*Cohee and Beroza*, 1994). In a study of the historic data from the 1923 Kanto, Japan, earthquake, Wald and Sommerville (1995) constrained the

slip on the subducting fault plane with the available geodetic data and placed constraints on the rupture timing with teleseismic body-waveform data.

Different studies have been carried out to assess the spatial slip distribution of the 1999 Hector Mine earthquake with multiple datasets: GPS, InSAR, regional strong motion, teleseismic broadband, and geodetic data sets (*Simons et al*., 2002; *Ji et al*., 2002; *Kaverina et al*., 2002; *Salichon et al*., 2004). Several others large earthquakes have been analyzed using a variety of the above methods (e.g.,1997 Imperial Valley earthquake, *Hartzell and Heaton*, 1983; 1989 Loma Prieta earthquake, *Wald et al*., 1991; 1992 Landers earthquake, *Wald and Heaton*, 1994; 1994 Northridge earthquake, *Wald et al*., 1996; 1995 Kobe earthquake, *Yoshida et al.*, 1996; 1999 Chi-Chi earthquake, *Zeng and Chen*, 2001; 1999 Izmit earthquake, *Bouchon et al*., 2002; 2000 Tottori earthquake, *Piatanesi et al*., 2007), and the complexity and general characteristic of these earthquakes have been used as starting point for several seismological applications.

In this chapter we evaluate the reliability of our nonlinear global search inversion technique, described in Chapter1 (see Section 1.6), by performing a joint inversion of geodetic and seismic data to retrieve the rupture history of two recent Japan earthquakes.

We apply our procedure to study the 2000 western Tottori earthquake and the 2007 Niigata-ken Chuestu-oki earthquake.

3.2 The 2000 western Tottori earthquake

The Tottori, Japan, earthquake (M_w = 6.6) occurred on October 6, 2000 at 04:30:17.75 UTC. The epicenter is located at 35.275°N and 133.350°E (*Fukuyama et al*., 2003).

Within the 15 years before the 2000 western Tottori earthquake, background seismicity covered the whole aftershock region of the 2000 western Tottori earthquake and several *M* 5 earthquakes were observed on the mainshock fault of the 2000 western Tottori earthquake (southern part of the aftershock region) (*Shibutani et al*., 2002). At that time, since the seismic observation network was sparse, they could not obtain the precise geometry of the fault structure in this

region. But from the background seismicity, a very vague image of the fault could be obtained before the mainshock. Their result showed that in the southern part of the aftershock region of the western Tottori earthquake, a fault existed before the mainshock but in the northern part, there was no information about the geometry of the fault before the mainshock. Moreover, Iwata and Sekiguchi (2002) analyzed the rupture process of the 2000 western Tottori earthquake, and they found that slip occurred only in the southern part of the aftershock region. Sagiya et al. (2002) reported from the analysis of Global Positioning System (GPS) data that the postseismic slip occurred in the northern part of the aftershock region where little slip occurred during the mainshock.

In the western Tottori region, northwest–southeast tectonic loading is dominant (*Tsukahara and Kobayashi*, 1991) due to the subduction of both the Pacific and Philippine sea plates beneath the Eurasia plate. This is the typical stress environment in the southwest of Japan (*Ichikawa*, 1971). Due to this driving stress, north–south– or east–west–trending strike-slip faults are commonly observed (Research Group for Active Faults of Japan, 1991). The 2000 western Tottori earthquake and its aftershocks occurred within the recently developed nationwide seismic network. According to the aftershock relocation, the rupture propagated bilaterally, along an almost vertical plane at about 145N (*Fukuyama et al*., 2003).

The 2000 Tottori earthquake was the first important earthquake recorded by the K-Net and KiK-net network (National Research Institute for Earth Science and Disaster Prevention) and thus provides a unique set of near field data (http://www.kik.bosai.go.jp/kik). In particular the KiK-Net accelerometer network, installed after the 1995 Kobe earthquake consists of sensors located both at the surface and at depth (100 m and greater).

This earthquake is an almost pure left lateral strike slip event for which different focal depths and different centroid moment tensor (CMT) solutions have been proposed (*Semmane et al*., 2005). Moreover, since there is no clear surface rupture, it is almost impossible to derive fault geometry from geological observations. Several moderate earthquakes ($M_w = 6 \div 7$) have produced little or no surface trace such as the 1984 Morgan Hill (*Hartzell and Heaton*, 1986), the 1989

Loma Prieta (*Uhrhammer and Bolt*, 1991), the 1992 Joshua Tree, and the northern part of the 1995 Kobe earthquakes (*Sekiguchi et al*., 2000). These recent events show that shallow rupture can occur not only on faults that cut the Earth's surface but also on hidden fault.

The 2000 Tottori earthquake caused relatively moderate damage: 182 people were injured and about 400 buildings destroyed. This low impact is largely due to the fact that the epicenter was located in a mountainous area. Nevertheless earthquakes of this magnitude can be very destructive, like the Kobe earthquake. According to Kagawa et al. (1999), ground motions generated by buried fault are larger than ground motions generated by earthquakes that rupture the surface. It is therefore essential to better constrain the source properties as are required for ground motion simulations for earthquakes scenarios.

In this study we investigate a source rupture model of the 2000 Tottori earthquake, by performing a joint nonlinear inversion of geodetic and strong motion data.

3.2.1 Data: Processing and weighting

To study the general characteristics of the slip history of the 2000 Tottori earthquake, we select 18 accelerometric stations (strong motion data from 7 KiK-net stations and 11 K-net stations (http://www.kik.bosai.go.jp) that do not seem to be strongly contaminated by site effects and that offer a good azimuthal coverage and 13 GPS stations (shown in Figure2.1). The epicentral distance ranges between 7 km and 60 km. We band-pass filter the recorded ground velocities between 0.05 and 0.7 Hz with a two-pole and two-pass Butterworth filter and we carefully verify that no spurious effect of the filter is introduced in the waveforms. The lower bound of the frequency band is determined by instrument capability; we observe that below 0.05 Hz several waveforms reveal some instabilities, such as small linear trends that arise during the strongest motion. The upper frequency limit is controlled by crustal model and fault discretization; with our model parameterization, the frequency content of the synthetic waveforms is negligible above 0.7 Hz. For all other stations, the three waveforms recorded by each

instrument (two horizontal components and one vertical) were used in the inversion; but not all data were weighted equally. In the Tottori area, fault motion is dominantly strike-slip (Research Group for Active Faults of Japan, 1991). Consequently, the horizontal components record the most significant ground motion and display a higher signal-to-noise ratio than the vertical records do. In the inversion, vertical waveforms are down weighted by a factor of 2 relative to the two horizontals. Further, both data and synthetic are normalized by the peak amplitude of the data to avoid giving too much weight in the inversion to the records with the largest amplitudes (*Cotton and Campillo*, 1995). The geodetic data available for the 2000 Tottori earthquake consist of coseismic GPS measurements in the form of displacement vectors for GPS sites and leveling surveys around the focal region (*Sagiya et al.*, 2002). These data were collected by the Japanese nationwide continuous GPS observation network.

Only the coseismic displacement vectors are used for the inversion. The measurements were made by differencing locations measured several weeks prior to the earthquake and about 2 months after the earthquake. The 13 closest stations associated with significant displacement have been selected in the inversion process. Figure2.1 shows the selected GPS stations. We jointly invert strong motion and geodetic data to better constrain the source properties.

3.2.2 Fault plane geometry and crustal structure

We adopt a simplified fault geometry with a rectangular surface of length 40 km, width 20 km and dipping at 90°. The top border of the fault is set at 0.5 km depth (*Semmane et al.*, 2005).

The hypocentral depth is 12.5 km, a value that is between 9.5 km as determined by *Fukuyama et al.* (2003) and 14.5 km as reported in *Semmane et al.* (2005).

As we have seen in previous chapter our procedure can use different STFs, in this application we use a simple rectangle function; and a parametric investigation on the effect of STFs, in finite-fault inversion of real data is discussed in Chapter 4.

In the previous chapter (see Section 2.2) we have shown that two different crustal models exist for the Tottori region. The DPRI model used for the hypocenter

determination by Research Center for Earthquake Prediction-Disaster Prevention Research Institute, Kyoto University, and the PK model, obtained by overlapping the DPRI crustal velocity model of the Tottori region with the KiK-Net borehole information (*Pulido and Kubo*, 2004). Since we have no strong reasons to favor the DPRI or PK velocity structure (see Table2.1 and Table2.2, respectively), we perform a separate search stage for each structure and we generate two model ensembles. Then we merge these ensembles to build up a larger one (about 7 million of models) on which we make statistical inferences. In this way we incorporate some degree of uncertainty of the crustal structure in the inversion procedure.

3.2.3 Inversion results

We invert simultaneously all parameters at nodal points equally spaced along strike and dip every 4 km. During the inversion, bounds of 0 to 2.5 m/s with 0.25 m/s interval are allowed for the peak slip velocity; the rise time varies from 1 to 5 sec at 0.5 sec interval; the rake angle goes from -15° to 15° by steps of 5°; the rupture time of each grid node is bounded by the times for a rupture to reach the node traveling at 2 and 4 km/s from the hypocenter.

Kinematic parameter distributions

The weighted average model (Figure3.1b) shows a patch of high slip velocity of the order of 1.5÷1.75 m/s that extends from the upper border down to a depth of 6 km with a length of about 12÷14 km; this patch is somewhat slightly diffused to the south-east along the down-dip direction.

A smaller region of relatively high slip velocity of about 0.75÷1.0 m/s is located deeper, between 14 and 18 km depth, about 12 km north-west from the hypocenter. Over the hypocenter and its surrounding region, the fault does not seem to have slipped significantly. The seismic moment of the average model is M_0=1.78×10^{19} Nm, that is comparable with M_0=1.6÷1.7×10^{19} found by *Semmane et al.* (2005). The rake angle indicates a basically pure left-lateral strike slip mechanism, with very small fluctuating dip component. The rupture velocity does

not change strongly on the fault plane; we find that the propagation is slightly faster along the strike (v_r = 2.6 km/s, corresponding to 70% of the shear wave velocity) than along the up-dip direction (v_r = 2.2 km/s, corresponding to 63% of the mean shear wave velocity).

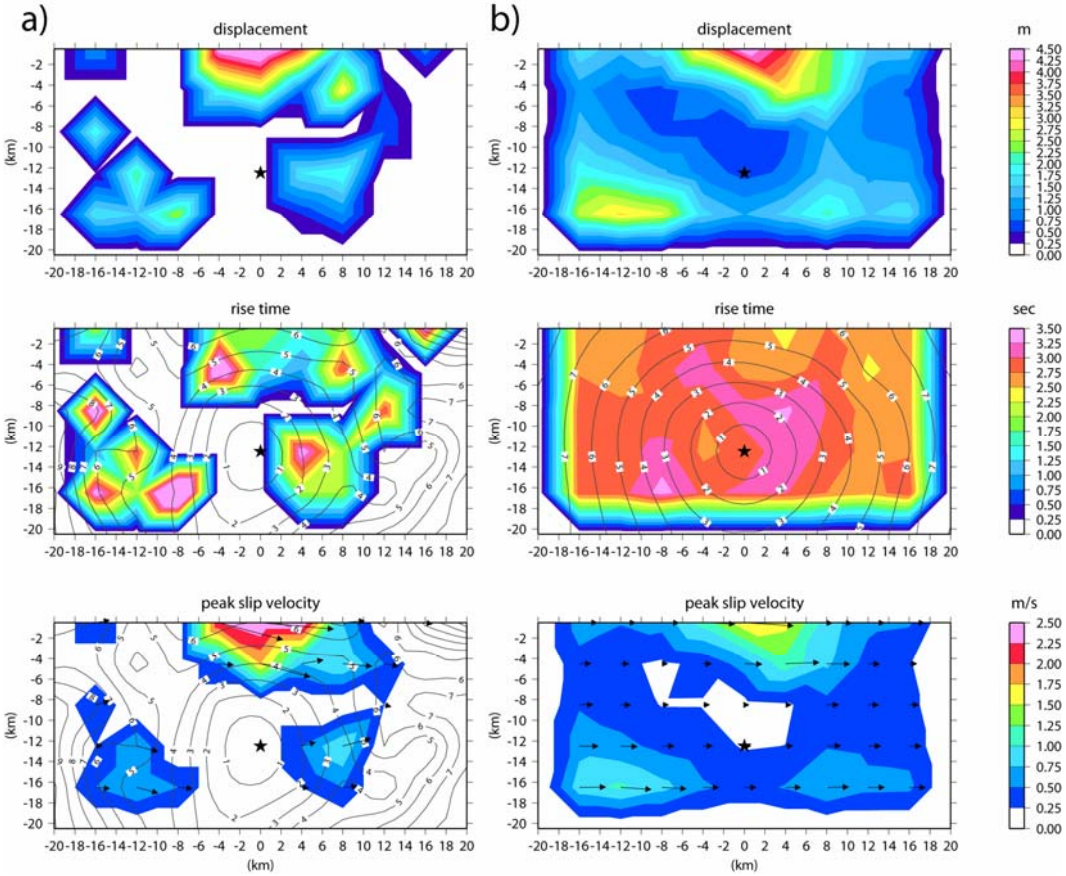

Figure3.1. Inverted rupture models: a) best model; b) average model from ensemble inference of the 2000 western Tottori earthquake. Top panels shows the total slip. Middle panels shows the rise time. Bottom panels shows the peak slip velocity; rupture time shown by contour lines (in seconds); black arrows represent the slip vector.

Note that the lack of variation in the rupture front contours (Figure3.1b) reflects the fact that the final model is an average model over many individual models in which the rupture front may be more irregular. The total duration of the rupture is about 8 sec.

Furthermore, the rupture propagation appears remarkably indifferent to the slip release. Overall, the rupture model appears quite smooth, mainly due to the averaging process on the model ensemble; on the contrary the best model (Figure3.1a) is rougher than the averaged one.

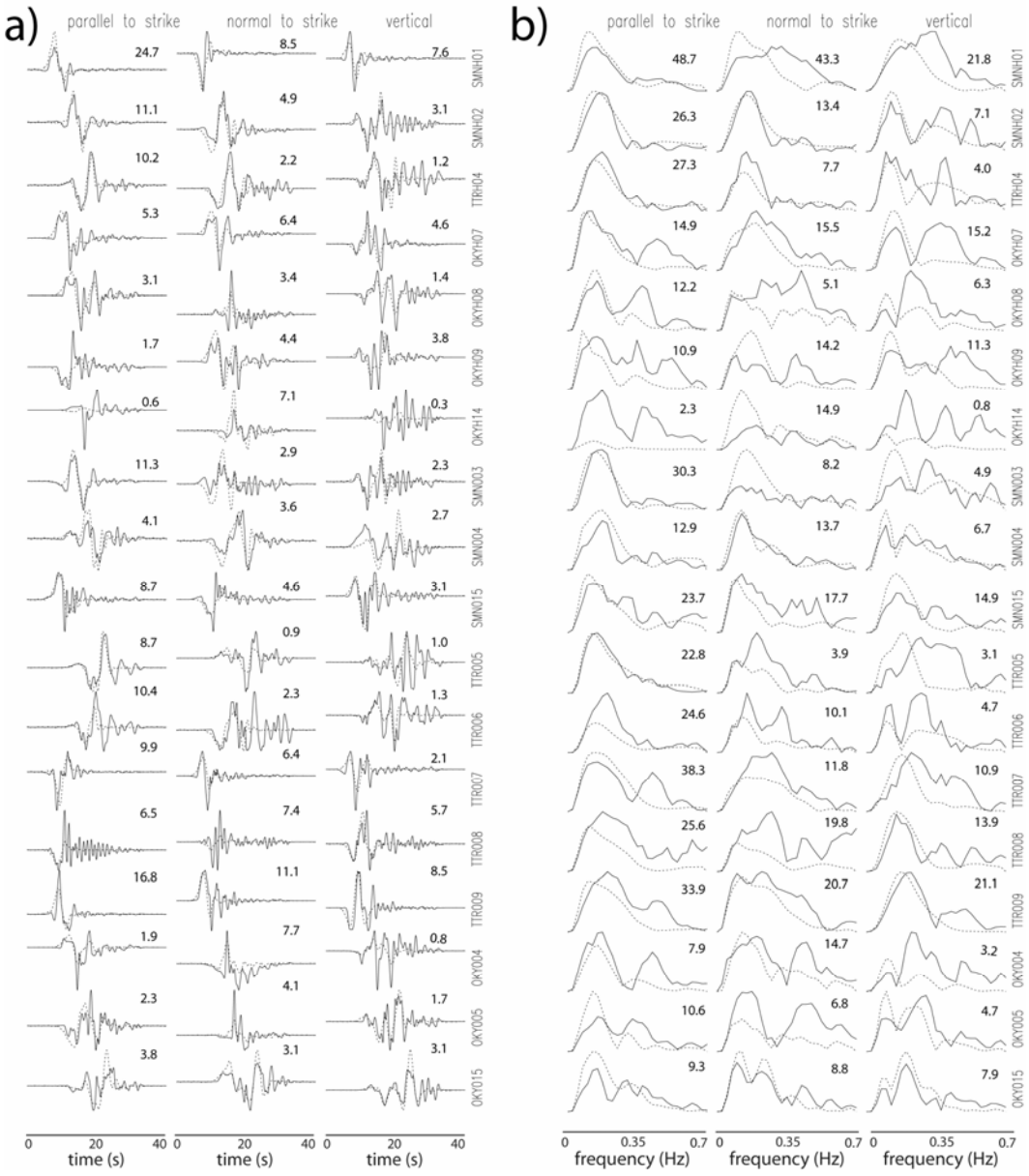

Figure3.2. Comparison of recorded strong motions (solid lines) with synthetic waveforms computed from the inverted average rupture model of Figure3.1b (dotted lines). Both records and synthetics are filtered in the frequency band 0.05÷0.7 Hz. a) comparison in the time domain; b) comparison in the frequency domain. Numbers with each trace are peak amplitude of the synthetic line in cm/s and in cm for the waveforms and the spectra respectively.

The comparison of the recorded and synthetic waveforms (Figure3.2a) shows a satisfactory agreement, though in some stations the high frequencies are not well reproduced (Figure3.2b); this is probably due to site effects that are not modeled in our calculations. Furthermore, the synthetic horizontal displacements match well with GPS vectors both in amplitude and direction (Figure3.3).

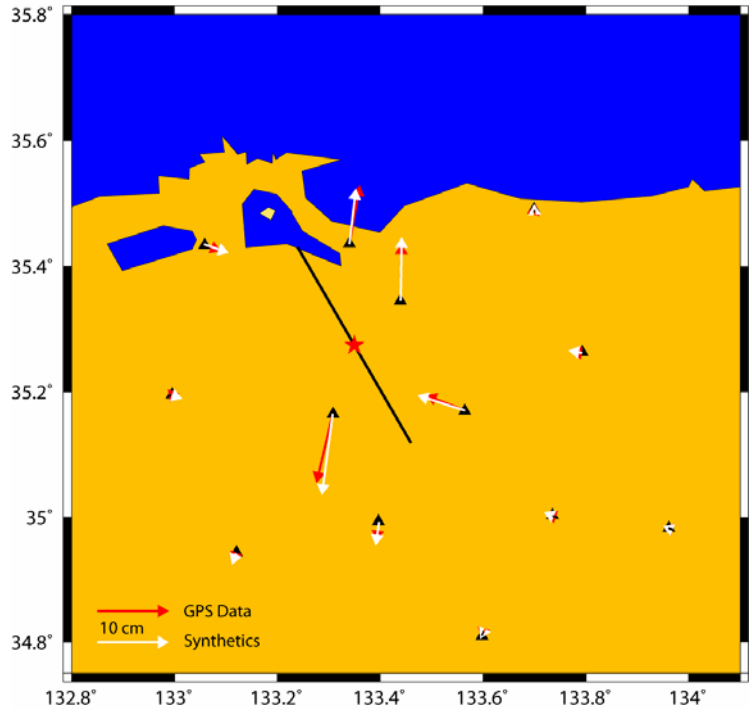

Figure3.3. Comparison of measured (red arrows) with synthetic (white arrows) horizontal displacements.

Appraisal of the ensemble

As we did in the previous chapter dealing with the synthetic tests, we also compute the standard deviations of the model parameters $<\sigma_i>$, that we show in Figure3.4. If we focus our attention on the regions of the fault that are characterized by large slip values, we may appreciate that the rupture model is stably inverted there. In fact, the standard deviations $<\sigma_i>$ are 3 to 5 times smaller than the corresponding averages of model parameters $<m_i>$; this indicates that the inverted model represents the major features of the rupture process quite well. On the other hand, if we look at those regions of the fault that are characterized by low and diffused slip, we may have an estimate of the sensitivity threshold of the data; a slip velocity of about 0.3÷0.4 m/s (the minimum standard deviation of the slip velocity) is allowed anywhere on the fault, defining a class of rupture models still consistent with the data.

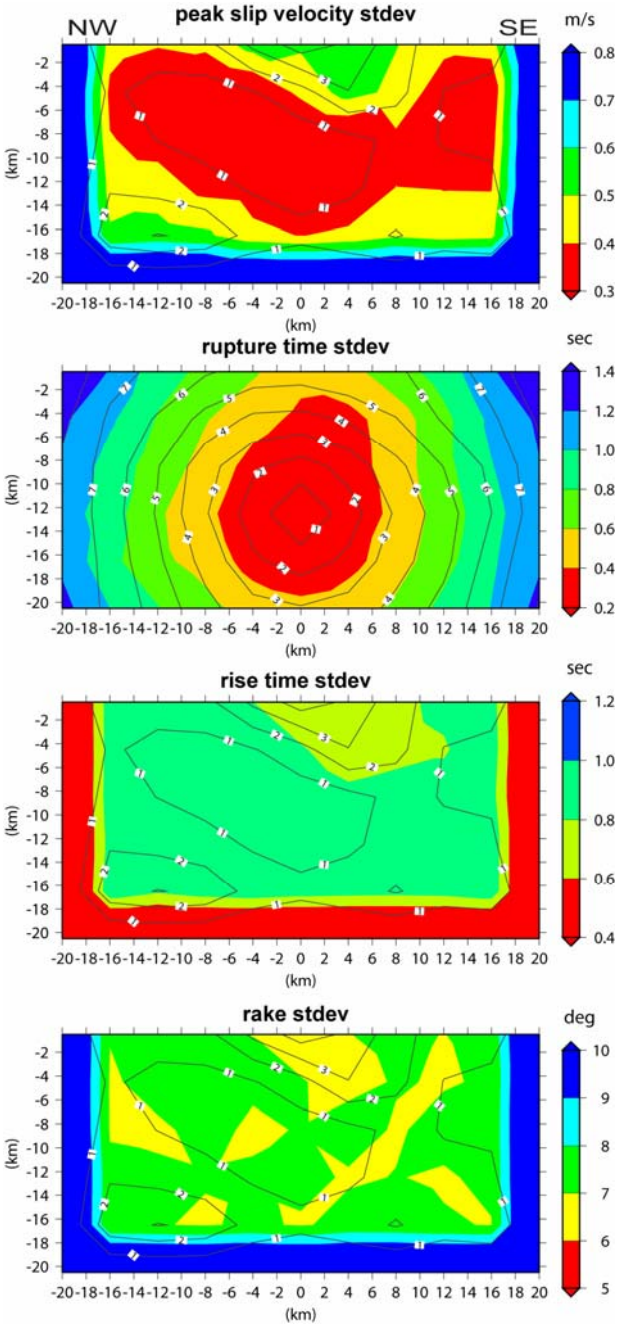

Figure3.4. Standard deviation of the average rupture model of the Tottori earthquake (shown in Figure3.1b), computed through ensemble inference. Contour lines represent total slip displacement in meters, but in second row panels where rupture times (in seconds) are plotted instead.

Remarks

The most striking feature of the inverted rupture model is the large coseismic slip at very shallow depth, in agreement with the results obtained by other investigators *(Iwata and Sekiguchi*, 2002; *Semmane et al*., 2005; *Festa and Zollo*, 2006). Also the slip distribution from the main shallow patch to the south-east and down-dip direction has been observed by the above investigators. However, differently from other studies, we find significant slip north-west of the

hypocenter, between 14 and 18 km depth. This part of the fault is characterized by peak slip velocity and rise time of about 1.0 m/s and 2.5 s respectively, thus yielding a mean slip of 2.5 m. Though this patch contributes less than the shallow one to the ground motion, nevertheless it is a robust feature of the rupture process. Considering the standard deviations of peak slip velocity and rise time corresponding to this patch, respectively of 0.5 m/s and 0.7 s, we may calculate lower (0.9 m) and upper (4.8 m) bounds for the slip amplitude. Intrigued by this characteristic of our rupture model, we analyze in some detail the search process that builds-up the model ensemble. We find that the shallow patch of large slip and its elongation to the south-east and down-dip direction are the features of the rupture model that are grasped first during the search stage; these models are probably located in a wide and local minimum of the cost function ($E \sim 0.5$).
Beyond this, as the algorithm goes on in the search of the model space, it encounters a new cluster of models featuring a second slip concentration at depth and characterized by lower value of the cost function ($E_{best} = 0.31$; $E_{average} = 0.35$). These last models are probably located in a narrow and deep minimum of the cost function, hardly accessible by linear and/or linearized inverse method.

3.3 The 2007 Niigata-ken Chuestu-oki earthquake

The 2007 Niigata-ken Chuestu-oki earthquake (Mw 6.6) occurred near the west coast of Honshu, Japan, on July 16th at 01:13 UTC (Figure3.5). The hypocenter has been located at 37.54°N and 138.61°E with 8 km depth (Japan Meteorological Agency). This earthquake caused severe damage in and around the source region: 11 people died and 1300 people have been injured. In particular, strong ground motions struck the Kashiwazaki-Kariwa nuclear power plant (labeled with KKNP in Figure3.5), situated at the eastern margin of the source area, reaching peak ground acceleration (PGA) value of more then 1200 gals (surface motions).

The 2007 Niigata-ken Chuetsu-oki earthquake is the first large event whose source fault extends beneath a nuclear power plant, thus it is receiving a particular attention of the scientific community. Besides, this region has been previously affected by another deadly earthquake, the 2004 Niigata Prefecture earthquake

(Mw = 6.6), occurred 50 km to the southeast of the recent quake. Because of this high seismic activity, inferences of seismic sources in this area result very important – to investigate the seismicity, the fault structures, and to understand the complex regional stress pattern.

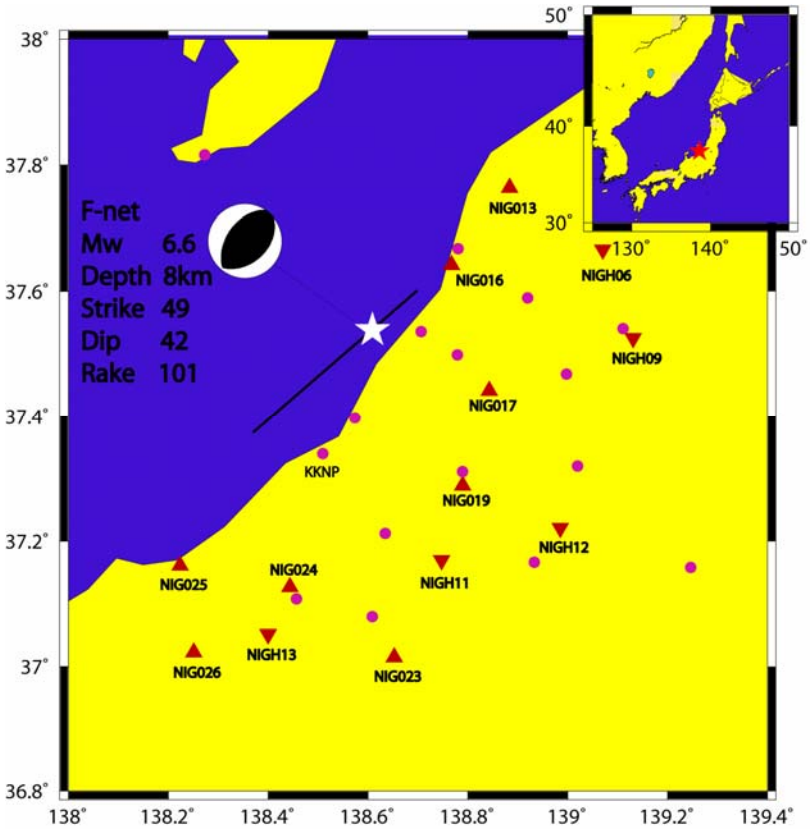

Figure3.5. Map of the fault geometry of the 2007 Niigata-ken Chuestu-oki, Japan earthquake. The black solid line represents the fault trace of the plane adopted in this study. White star indicates the epicenter. Red triangles and inverted triangles represent K-Net (surface sensor) and KiK-Net (borehole sensor) strong motion stations respectively. Violet dots represent GPS stations. KKNP indicates the site of Kashiwazaki - Kariwa nuclear power plant. The focal mechanism estimated by the moment tensor analysis (F-net) is displayed.

This area is characterized by a zone of high compressional deformation, called the Niigata-Kobe Tectonic Zone (NKTZ), that is associated with the boundary between the Amur plate and the Okhotsk plate. This high-strain-rate zone is characterized by shortening tectonics with E-W- to NW-SE trending compressive axis (*Nakajima and Hasegawa*, 2007). Coherently, the focal mechanism of the 2007 Niigata earthquake, estimated by the moment tensor analysis (F-net: http://www.fnet.bosai.go.jp), is a reverse fault type with conjugate nodal planes dipping to NW and SE (plane 1: N215°E, 49°, 80°; plane 2: N49°E, 42°, 101° for

strike dip and rake angle, respectively). Both fault planes have been considered by Aoi et al. (2007) for their preliminary waveform inversion, and not significant differences have been found by the authors to discriminate the true fault plane. However, the relocation of aftershocks (e.g., DPRI, 2007: http://www.eqh.dpri.kyoto-ac.jp/~mori/niigata/reloc.html) shows a fairly clear eastward dipping trend.

Besides recent studies (*Toda*, 2007; *Koketsu et al.* 2007), on the 2007 Niigata-ken Chuetsu-oki earthquake, designate the SE dipping nodal plane as the preferred one. Finally, Irikura et al.(2007) consider the same fault plane inferred from the aftershocks distribution re-determined using the OBS seismometers.

The dense seismic telemetry networks (KiK-Net and K-Net), deployed by the National Research Institute for Earth Science and Disaster Prevention (NIED) allow us to collect a large number of ground motion records. Besides, numerous GPS measurements on that area have been supplied by the Geographical Survey Institute (GSI).

In this application we provide a source model for the 2007 Niigata-ken Chuetsu-oki earthquake estimated by jointly inverting strong-motion seismic data and GPS records.

3.3.1 Data and fault model

Strong motion data from 13 stations of KiK-Net and K-Net and 15 GPS records of the co-seismic surface displacement, are used for the analysis. Their epicentral distances are less than 70 km and their locations are shown in Figure3.5.

Original acceleration records are integrated to obtain velocity waveforms. The resulting ground velocities are band-pass filtered between 0.02 and 0.5 Hz using a two-pole and two-pass Butterworth filter. We invert 60 seconds of the records, including body and surface waves. We perform the inversion for the south-east dipping fault (Figure3.5) with the strike and dip set to those of the moment tensor solution provided by F-net (49° and 42°, respectively; NIED). According to aftershocks distribution we assume a fault model of 38.5 km length and 31.5 km

depth with the top border at 0.5 km depth. The rupture starting point is located at the hypocenter: 37.54°N, 138.61°E with 8 km depth.

In this application, we adopt a regularized Yoffe function with T_{acc} (time of peak slip velocity) equal to 0.3 sec (see Eq.(1.11c) in Section 1.6). To calculate the Green's functions, we adopt a one-dimensional structure model (see Table3.1), referring to the velocity structure proposed by Kato et al. (2005).

Table3.1. Velocity Structure of the Niigata region (*Kato et al.*, 2004)

H (km)	**Vp (km/s)**	**Vs (km/s)**	**d (kg/m^3)**
0	2.30	1.33	2400
3	4.05	2.34	2500
6	5.72	3.30	2600
9	5.81	3.35	2700
12	5.89	3.40	2800
15	5.97	3.45	2900

3.3.2 Synthetic test

Despite the high number of triggered station, the azimuth coverage is limited to ~180° due to the off-shore location of the epicenter (Figure3.5).

Preliminarily, we test the goodness of stations' distribution by performing a synthetic test. Synthetic data are generated using the target rupture model displayed in Figure3.6a. Slip is concentrated only on two main asperities, A and B. Asperity A has a peak slip velocity of 2.5 m/s and a rise time of 1.5 s; asperity B has 3.5 m/s of peak slip velocity and a rise time of 2.5 s. Both asperities have slip and rake equal to 1.98 m and 90°, respectively. The rupture front propagates at 2.5 km/s, except in the upper left part of the fault, where it is propagating at nearly 3.5 km/s. We invert simultaneously all parameters at nodal points equally spaced along strike and dip every 3.5 km.

During the inversion, the peak slip velocity can vary between 0 to 5.0 m/s with 0.25 m/s interval; the rise time varies from 0.5 to 4 sec at 0.25 sec interval; the rake angle goes from 75° to 105°, by steps of 5°; the rupture time of each grid node is bounded by the times for a rupture to reach the node traveling at 2 and 4 km/s from the hypocenter.

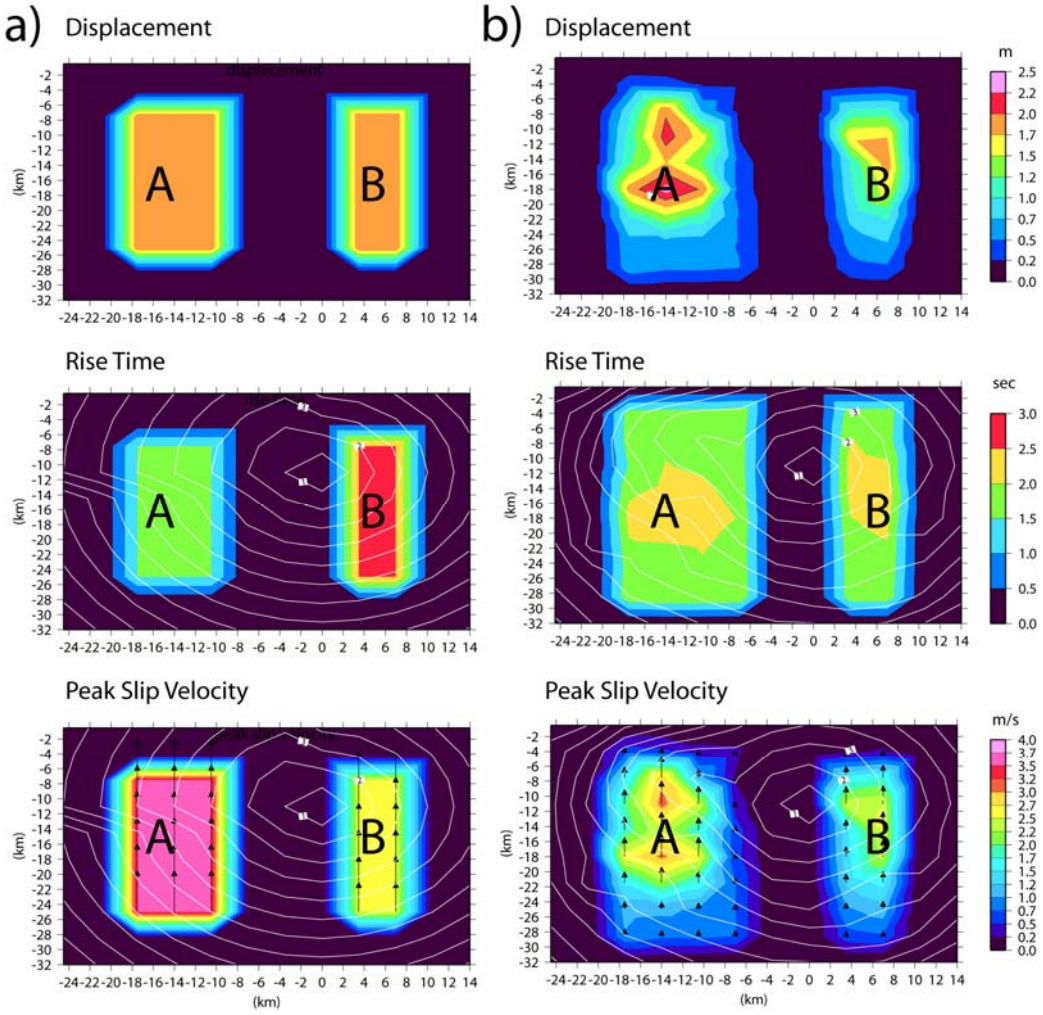

Figure3.6. a) Target rupture model used for synthetic test. b) Inverted rupture model (average model from ensemble inference). In both cases horizontal axis is along-strike distance measured from the epicenter. Vertical axis is down-dip distance measured from the ground surface. Upper panels show total slip; middle and bottom panels shows rise time and peak slip velocity, respectively; rupture time shown by contour lines (in seconds). Black arrows represent the slip vector. The slip patches are denoted by capital letters A and B (see text for details).

Adopting the crustal model listed in Table3.1, we compute synthetic ground velocities in the frequency band 0.02÷0.5 Hz and horizontal components of static displacement and we use these as our dataset.

To perform the inversion we apply the nonlinear technique, described in Section 1.6. The inverted model (see Figure3.6b) is very similar to the target one; the positions of the two asperities are correctly imaged and the peak slip velocity well estimated. The rise time is also well retrieved and the faster propagation of the rupture front, on the upper left side, is caught fairly well. Finally, the rake angle on both asperities is very well constrained.

The comparison of the waveforms (Figure3.7a) and horizontal displacements (Figure3.7b) reveals an almost perfect match between data and synthetics.

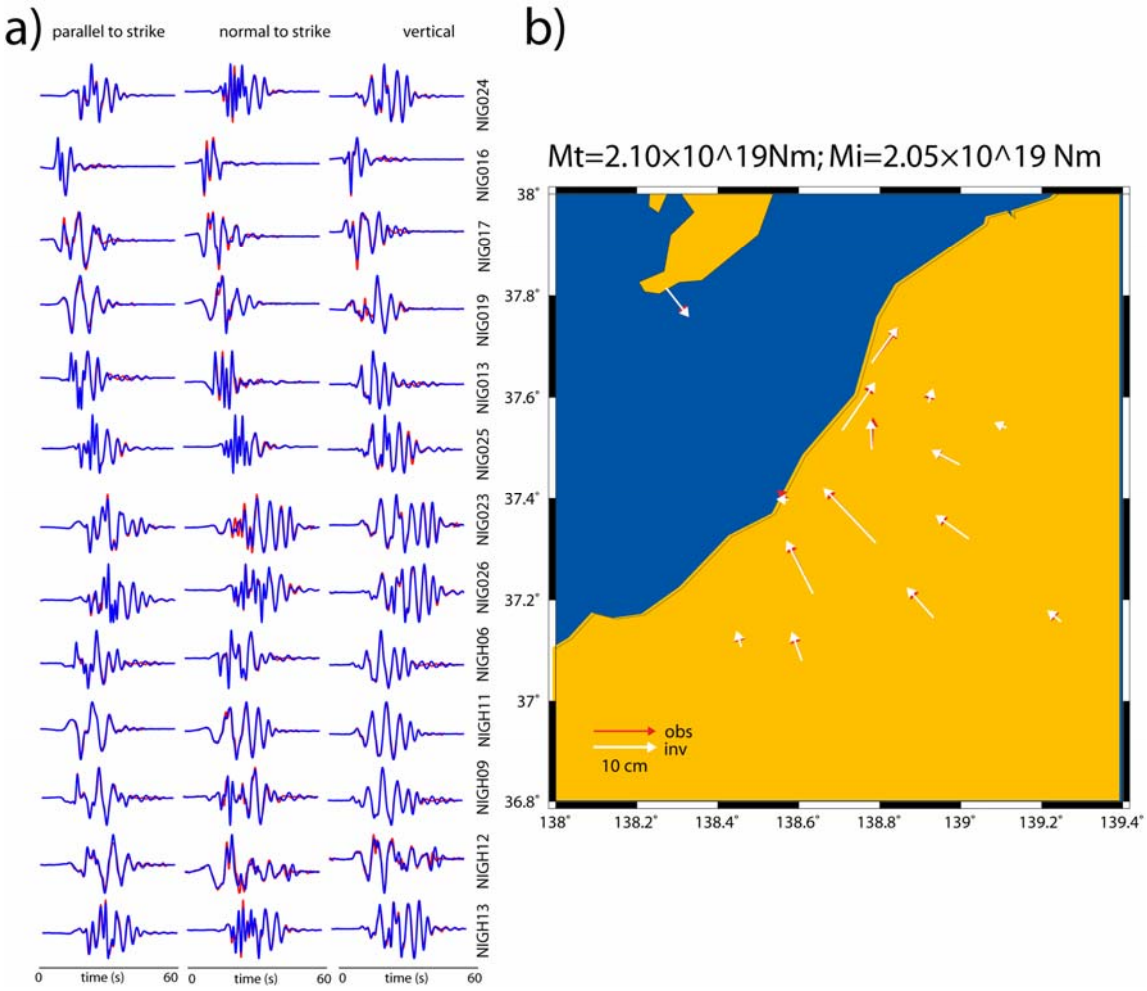

Figure3.7. a) Comparison of synthetic ground velocities from the target rupture model (blue lines) with the inverted rupture model (red lines). b) Comparison of synthetic horizontal displacements from the target rupture model (red arrows) with those from the inverted rupture model (white arrows).

Even if the azimuthal coverage of the stations has a gap, the synthetic test proves that it is good enough to obtain reliable results.

3.3.3 Rupture process of the 2007 Niigata earthquake

In the application to the real data of the 2007 Niigata-ken Chuetsu-oki earthquake, all kinematic parameters are simultaneously inverted at nodal points equally spaced along strike and dip every 3.5 km. During the inversion, the peak slip velocity is allowed to vary between 0 and 4 m/s with 0.25 m/s step increment; the rise time goes from 0.5 to 4 sec at 0.25 sec interval; the rake angle varies within ±30°, by step of 5°,with respect to 101° (that is the rake angle of the moment tensor solution of F-net); the rupture time is bounded by the times for a rupture to reach the node traveling from 2 to 4 km/s from the hypocenter.

The algorithm explores about 3 millions rupture models, finds the best fitting model, calculates the weighted average model, and the associated standard deviation. Figure3.8 shows the weighted average model.

The retrieved rupture history features two principal patches of slip: a small patch near the nucleation point and a larger one at about 15 km south-west from the nucleation. Both asperities are characterized by similar rise time and peak slip velocity values which correspond to maximum values of slip displacement of about (2.0÷2.5) m (upper panel, Figure3.8). The slip distribution and the seismic moment ($M_0 = 1.6 \times 10^{19}$ Nm) agrees with those inferred by Aoi et al. (2007).

The slip direction (rake angle), shown in the bottom panel of Figure3.8 (black arrows), clearly indicates an almost pure dip slip fault mechanism.

The total rupture duration is about 11 sec.

It’s interesting to note that in correspondence of the larger asperity the rupture front accelerates from 2.0 km/s to 2.8 km/s. The rupture acceleration occurs in the south-western portion of the fault plane, very close to the Kashiwazaki-Kariwa nuclear power plant.

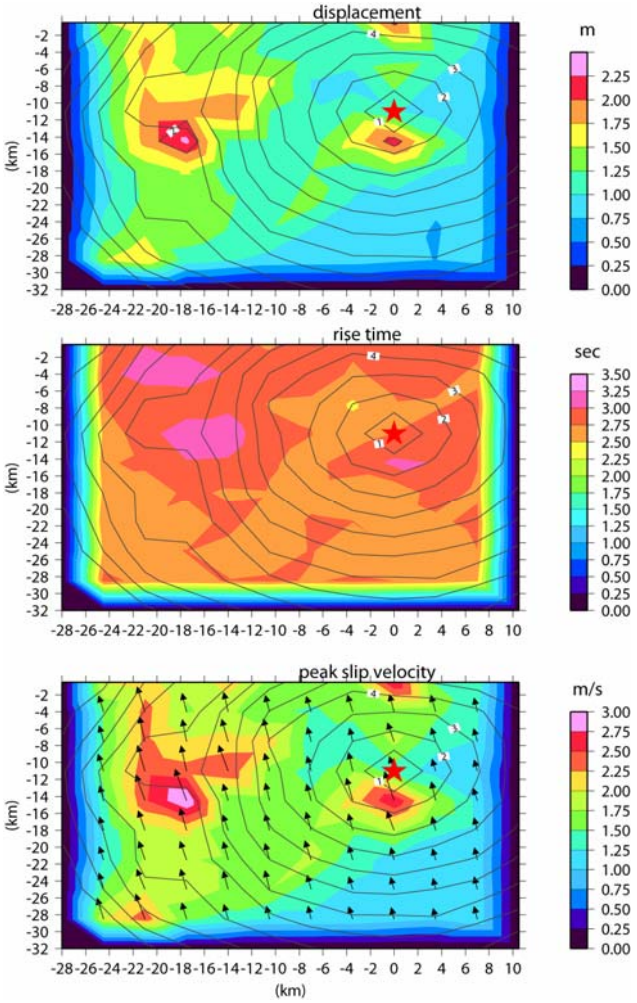

Figure3.8. Inverted rupture model (average model from ensemble inference) of the 2007 Niigata-ken Chuestu-oki earthquake. Top, middle and bottom panels show total slip, rise time and peak slip velocity distributions, respectively. Rupture time shown by contour lines (in seconds); black arrows displayed in bottom panel represent the slip vector.

This feature could partially explain the severe ground motion recorded at KKNP site, which was more than twice, at the maximum, as strong as the designed acceleration in the EW direction at the foundation base mat level of 3 nuclear power units (*Sugiyama*, 2007).

The comparison of the recorded and predicted waveforms (Figure3.9) shows a satisfactory agreement, apart from some stations. This is probably due to the complex wave propagation in an heterogeneous medium and to the presence of dominant surface waves in some records.

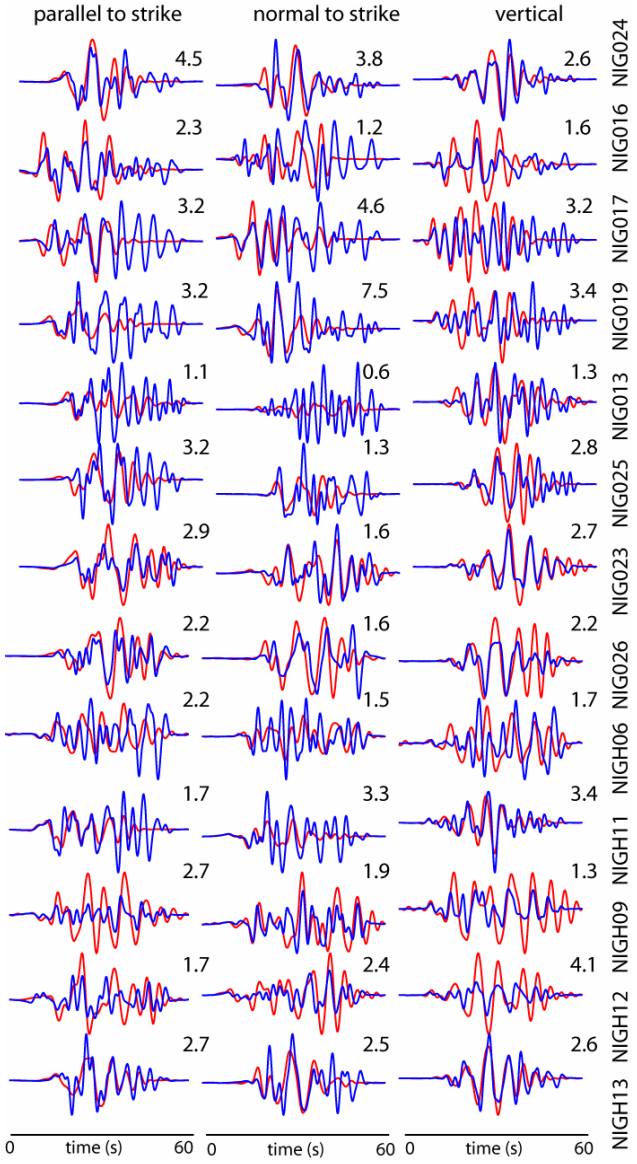

Figure3.9. Comparison of recorded strong motions (blue lines) with predicted (red lines) waveforms computed from the inverted rupture model of Figure3.8. Numbers with each trace are peak amplitude of the synthetic line (cm/s).

Besides, the fit between synthetic and observed horizontal displacement vectors (Figure3.10), at the selected GPS stations, shows a good match except in KKNP site. The recorded GPS in this site shows a different direction compared to the deformation observed on the other GPS data. These discrepancy is probably due to site effects or liquefaction phenomena, which need further investigations.

In general, the coseismic deformation pattern clearly shows dip slip motion, in agreement with the result obtained for the retrieved rake distribution (Figure3.8, bottom panel).

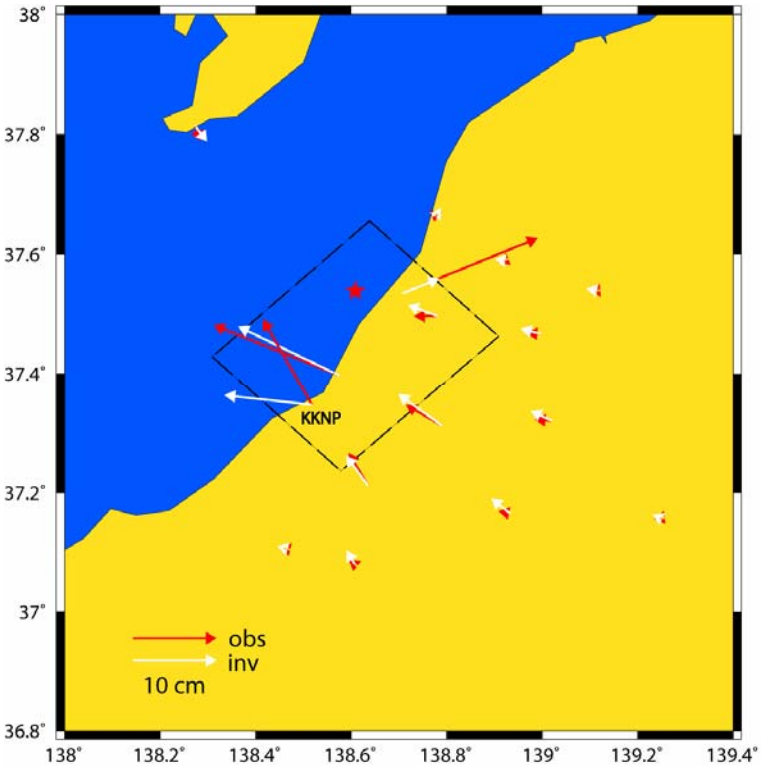

Figure3.10. Comparison of observed (red arrows) with synthetic (white arrows) horizontal displacements.

3.4 Discussion

In this chapter we have stressed the capability of our nonlinear inversion method to solve the finite-fault non-linear inverse problem, which consists of retrieval of the complete rupture history on a finite fault using seismic and geodetic data.

We have applied this inverse technique to study the 2000 western Tottori and the 2007 Niigata-ken Chuestu-oki, Japan, earthquakes.

In the first case we have performed the inversion by using waveforms in the frequency band 0.05÷0.7 Hz recorded by 18 accelerometers and using horizontal static displacements measured at 13 GPS sites. We have confirmed that the rupture process is characterized by large slip (3÷4 m) at very shallow depths, from the top of the fault down to a depth of 6 km. However, thanks to the ability of this inverse technique to escape local minima of the cost function, we imaged a slip patch (2÷2.5 m) located deeper, between 14 and 18 km depth, not inferred by

previous studies. The relatively small standard deviations of the corresponding parameters, computed through the ensemble inference, indicate that this slip patch is a real feature of the rupture history.

The rupture process of the recent 2007 Niigata-ken Chuestu-oki earthquake has been investigated by performing a joint inversion of 13 strong motion and 15 co-seismic surface displacement GPS data. Due to the limited azimuthally coverage, a preliminary synthetic test has been performed with the aim to test the goodness of stations' distribution. The test has shown the good resolving power of the data and the reliability of the inversion results.

The inverted source process model shows two main asperities: a smaller one near the nucleation point and a larger one at about 15 km south-west from the nucleation, with a maximum value of slip displacement of about (2.0÷2.5) m. An interesting characteristic of the retrieved rupture history concerns the inferred rupture velocity distribution, which shows an acceleration of the rupture front in the south-west and shallower part of the fault. This feature could partially explain the large-amplitude signals observed in the Kashiwazaki-Kariwa nuclear power plant (KKNP site), situated at the eastern margin of the source area.
Thus the study of seismic sources in this area becomes an issue of public attention and it results very important for seismic hazard analysis.

In summary, the procedure we propose is able to retrieve the complete rupture history of large earthquakes on a finite fault, by means a nonlinear joint inversion of seismic and geodetic data. Furthermore the ensemble inference provides the possibility of estimating the variability of rupture models that are consistent with the data. In particular it allows us to evaluate lower and upper bounds for some source parameters, such as peak slip velocity and rupture speed. This may have important implications, for instance for ground motion prediction through ground shaking scenarios.

Finally, to test the resolution and efficiency of our technique and to assess its weaknesses and strength, we have participated to the "Blind Test for Kinematic Source Inversion" (http://www.seismo.ethz.ch/staff/martin/BlindTest.html), carried out within the frame-work of the EC-project SPICE (**S**eismic Wave **P**ropagation and **I**maging in **C**omplex Media: A **E**uropean Network).

Several researchers have submitted their inversion procedure to the Blind Test.
A comparison between the different results has been presented during the 2007 AGU Fall Meeting, San Francisco, in the session S11 ("*Earthquake Source Inversion Under Scrutiny: Validation, Resolution, Robustness"*) .
In Appendix we report a detailed description of the Blind Test and we show the obtained results.

Chapter 4

Dynamic consistency of kinematic modeling

4.1 Introduction

An earthquake is a dynamically propagating shear crack that radiates seismic waves and the related stress variation on the fault plane is an indication of the dynamic behavior of the source rupture process. As Aki and Richards (1980) pointed out, to understand the physical processes occurring in the source region, one must study stress-dependent material properties. That is, one examines the way in which material failure nucleates and spreads over a fault plane, rapidly relieving stresses that had slowly risen (due to long-term tectonic processes) to exceed the strength of material in the source region. In general, an earthquake involves three main stages: initiation of rupture, frictional sliding during the rupture process and termination of rupture.

Two major goals of seismology are to discover the stress condition on faults before and during earthquakes and to infer a constitutive relation that describes the material response to the applied stress (*Guatteri and Spudich*, 2000). Besides, the redistribution of dynamic stress during coseismic ruptures has been associated to the evidence of fault interaction and earthquake triggering (*Belardinelli et al*., 1999, 2003a).

Several papers have investigated the dynamic processes of earthquakes (*Fukuyama and Mikumo*, 1993; *Olsen et al*., 1997; *Bouchon et al*., 1998; *Day et al*., 1998; *Fukuyama and Madariaga*, 1998, 2000; *Oglesby et al*., 2000; *Dalguer et al.*, 2002). In these studies the friction law plays a fundamental role; it represents the governing equation of the failure process and specifies the dependence between the components of stress tensor and other physical variables, during the frictional sliding stage of an earthquake. Different earthquakes, show different source rupture processes; this diversity suggests that material properties controlling rupture evolution are spatially heterogeneous and may vary strongly for different earthquakes. Accordingly, understanding the prevailing friction laws

and the relevant parameters could provide a unifying physical basis for understanding this variability and heterogeneity of the source processes (*Zhang et al.*, 2003). Several constitutive laws have been proposed in the literature.

Two friction laws have been commonly used: the slip-weakening law (SW) (*Ida*, 1972; *Andrews*, 1976; *Day*, 1982) and the velocity weakening law (*Carlson and Langer*, 1989; *Cochard and Madariaga*, 1994; *Fukuyama and Madariaga*, 1998). Different studies have presented various friction laws based on laboratory experiments of rock friction in which frictional sliding is regarded as an analog to fault slip in natural earthquakes (*Dieterich*, 1978; *Ohnaka and Kuwahara*, 1990; *Ohnaka and Shen*, 1999).

However, the scale of laboratory rock experiments is too small compared with a fault to apply the experimental results directly to actual earthquakes. Thus, we need to estimate the dynamic processes from the observed data of actual events. In recent years, the detailed kinematic models of earthquake slip obtained from large well-recorded events provide us the means to indirectly infer some of the characteristic of the stress field acting on earthquakes faults. Indeed, earthquake kinematic models are often used to retrieve the main parameters of the causative dynamic rupture process. These models, obtained through the inversion of seismograms and geodetic data, can be used as boundary condition in dynamic modeling to compute the traction evolution on the fault. Once traction and slip time histories are inferred at each point on the fault plane, it is feasible to estimate the key parameters, describing the dynamic of the source rupture process.

To date, several attempts have been made to infer dynamic parameters by various methods (*Papageorgiou and Aki*, 1983; *Ide and Takeo*, 1997; *Olsen et al.*, 1997; *Day et al*., 1998; *Bizzarri et al*., 2001; *Mikumo et al.,* 2002; *Piatanesi et al*., 2004; *Yasuda et al*., 2005; *Fukuyama and Mikumo*, 2007).

However, the measure of these quantities can be strongly affected by the adopted parameterization of kinematic source models, inferred from data inversion (*Hisada*, 2000, 2001; *Guatteri et al*., 2003; *Nielsen and Madariaga*, 2003). Often, such kinematic rupture inversion is only based on plausible considerations, and questions about the dynamic consistence of the rupture processes are not addressed.

Piatanesi et al. (2004), pointed out that dynamic inferences may be strongly biased by unphysical constraints on the source time function adopted for kinematic source modeling. In fact, slip velocity source time functions commonly used in kinematic inversions and forward simulations have a number of problems that could affect the computation of ground motion (*Dreger et al.*, 2007). These problems include an imposed greater than omega square high frequency spectral decay rate, introduction of spectral holes from the use of temporally sharp functions such as boxcar and triangle functions, and the use of functions that are inconsistent with dynamic rupture models. Here we propose that, in order to make this task achievable, suitable inversion schemes and appropriate choices of the kinematic parameters must be adopted.

In this chapter we focus our attention on the importance of adopting source time functions (STFs) compatible with earthquake dynamics to image the kinematic rupture history on a finite fault. To this purpose, first we present several synthetic tests to analyze the uncertainty due to the adopted parameterization scheme of kinematic source modeling. Then, to assess how the choice of source time function can bias the retrieved kinematic rupture histories, we perform different kinematic inversions of strong motion and GPS data, adopting different STFs.
Finally, in order to appreciate the dependence of relevant dynamic parameters on the source time function adopted in kinematic input model, we use the inverted rupture histories as boundary conditions in dynamic modeling of seismic rupture.
Our study is inspired by the work of Piatanesi et al. (2004), but it is basically different from it for the following reasons. Piatanesi et al. (2004) do not perform any kinematic inversion; their study is an application to verify the effect of an assumed kinematic rupture model on the traction evolution. From a methodological point of view their research is exclusively based on dynamic modeling. The novelty of our approach is the use of different slip velocity time functions, which are directly implemented in the inversion procedure. The use of this innovative inversion technique implemented with different source time functions is an important improvement in finite-fault nonlinear inversion studies and allows us to evaluate the importance of the adopted source time functions in kinematic inversions. The main distinction from the work of Piatanesi et al.

(2004) is that the effect of a particular choice of source time function is inherently included in the inversion procedure; so that it could be successively estimated on the dynamic modeling.

The innovation dwells with the possibility to evaluate, in a quantitative manner and by means of real data, the differences between traction history estimates; given that kinematic inversions could retrieve rupture's parameter affected by strong heterogeneities. Therefore, it is essential to analyze the effect of this features on the dynamic inferences. The method we propose provides us an effective tool to attain this task; since it allows us to associate to a given kinematic rupture model its corresponding dynamic model. This is an important result, since nowadays, obtaining a dynamic model of real earthquake still represents an open and unsolved problem inside the scientific community.

4.2 Sensitivity to parametric uncertainty

In this section we investigate the sensitivity of kinematic modeling to different kind of model parameterizations and we verify the effect of the *a priori* choices or assumptions that must be made in any kinematic inversion procedure.

In particular we study the robustness and the reliability of the inverted kinematic parameters, focusing on total slip and peak slip velocity. In the literature, the kinematic modelers invert for only one of the latter two parameters and derive the others. The relation between these parameters depends on the *a priori* choice of the source time function (STF). This occurs in a single time window approach, in which the temporal evolution of slip (or slip velocity) is given by adopting an analytical expression of STF.

We use our slip inversion procedure to study these parameters uncertainties due to the model parameterization, and to verify if an accurate choice of STF allows us to improve the resolution of both slip and slip velocity parameters.

Several researchers pointed out that source model discrepancies for the same event result from different model parameterizations (*Cohee and Beroza*, 1994) and recommended taking into account the complex interactions between kinematic source parameters (*Guatteri and Spudich*, 2000; *Beresnev,* 2003).

These aspects can strongly bias the result of a kinematic inversion in terms of the retrieved model parameter distributions. These biases should be considered when interpreting the reliability of an inferred rupture model (*Mai et al.* 2007).
To this purpose, in this section we compare the results obtained from two different inversions performed with two different choices of inverted model parameter.

4.2.1 Synthetic test I: Target model

In order to discuss how the choice of parameterization scheme can bias the retrieved kinematic rupture histories, we present the results of two different synthetic tests.
We consider the fault geometry and station distribution of the 2000 western Tottori, Japan, earthquake (Mw 6.6). We select 18 accelerometric stations and 13 GPS locations (shown in Figure2.1).
To obtain a more realistic source characterization we construct a fairly complicated target rupture model. The fault has the following geometrical parameters: strike is 150°, dip is 90°, rake is 0°, length and width are 40 km and 20 km, respectively; the top of the fault is 0.5 km below the free surface. Slip is concentrated only on two main asperities, A and B (see Figure4.1).
Both asperities have a slip displacement of 2 m (upper panel of Figure4.1) ; asperity A has a rise time of 1 sec, while asperity B has a rise time of 2 sec (middle panel of Figure4.1).
The rupture front propagates at 2.5 km/s. In all sub-faults, we assume a boxcar function as a slip velocity time-function (see Eq.(1.11a), Section 1.6). The resulting peak slip velocity distribution is shown in Figure4.1 (bottom panel): asperity A has a peak slip velocity of 2 m/s, while asperity B has 1 m/s of peak slip velocity.

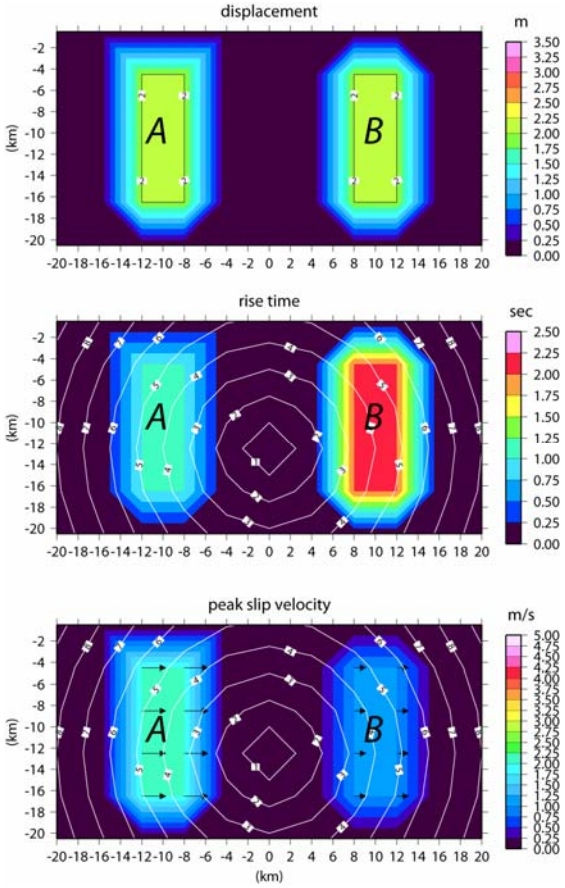

Figure4.1. Target rupture model used in synthetic test I. Horizontal axis is along-strike distance measured from the epicenter. Vertical axis is down-dip distance measured from the ground surface. Top panel shows slip displacement. Middle panel shows the rise time; rupture time shown by contour lines (in seconds). Bottom panel shows peak slip velocity. The slip patches are denoted by capital letters A and B (see text for details). Black arrows represent the slip vector.

We highlight that, in this synthetic test, the relation between peak slip velocity, slip and rise time is linear because of the simplicity of the assumed source time function. Adopting the crustal model, listed in Table2.2, obtained by overlapping the velocity structure of the Tottori region (DPRI, 2000) with the KiK-Net borehole information (*Pulido and Kubo*, 2004) we generate synthetic seismograms in the frequency band 0.05÷1.0 Hz and we associate the horizontal component of static displacements to synthetic GPS data, using these as our virtual datasets. Each node of the fault plane is characterized by four model parameters: peak slip velocity (or by slip displacement), rake angle, rise time and rupture time.

To assess how the choice of model parameterization affects the reliability of imaged rupture process, we perform two different kinematic inversions. We invert

the same synthetic dataset but in one case we invert for peak slip velocity and rise time (we call this *test inv_PSV*), in the other one we invert for slip displacement and rise time (we call this *test inv_Dmax*). Then, from the retrieved parameters, we compute total slip and peak slip velocity distribution, respectively. Rupture time and rake are kept equal to the target model in both inversions. In order to guarantee the same dimensions of model space, explored in the two different inversions, we set suitable bounds for each of kinematic parameters: the peak slip velocity varies from 0.0 m/s to 3.5 m/s with 0.25 m/s interval (in *test inv_PSV*); the slip displacement goes from 0.0 m to 3.5 m by steps of 0.25 m (in *test inv_Dmax*); the rise time ranges between 0.5 sec and 3.0 sec at 0.25 sec interval, in both synthetic tests.

4.2.2 Synthetic test I: Kinematic parameters comparison

For each inversion, the algorithm explores about one million rupture models, finds the best fitting model and calculates the weighted average model $< m_i >$ (see Eq.(1.20), Section1.6) and the corresponding standard deviation $< \sigma_i >$ (see Eq.(1.21), Section1.6). The choice of a weighted average model permits us to extract the most stable features of the earthquake rupture that are consistent with the data (*Piatanesi et al.*, 2007). In Figure4.2 we compare the kinematic source parameters associated to the average model and inferred from the two different inversions (*test inv_PSV*, left side; *test inv_Dmax*, right side). The retrieved rupture models obtained from the two different inversion schemes are not equal. Looking at the slip on the fault plane (upper panels of Figure4.2), we observe that the different models tend to retrieve a slip distribution quite similar to the target one. These results are confirmed by the retrieved total seismic moment M_o, constrained through the inversion of geodetic data: both models have M_o very similar ($M_o=1.45\times10^{19}$ Nm for *test inv_PSV*; $M_o=1.43\times10^{19}$ Nm for *test inv_Dmax*) to the target seismic moment ($M_o=1.5\times10^{19}$ Nm). Comparing the rise time and peak slip velocity distributions (middle and bottom panels of Figure4.2), of the two inversions, we note that both models show two patches for each parameter, with similar extent and location on the fault. Besides, while the

amplitudes of rise time are comparable, the peak slip velocity values obtained from the *test inv_Dmax* show some differences with respect to the target model.

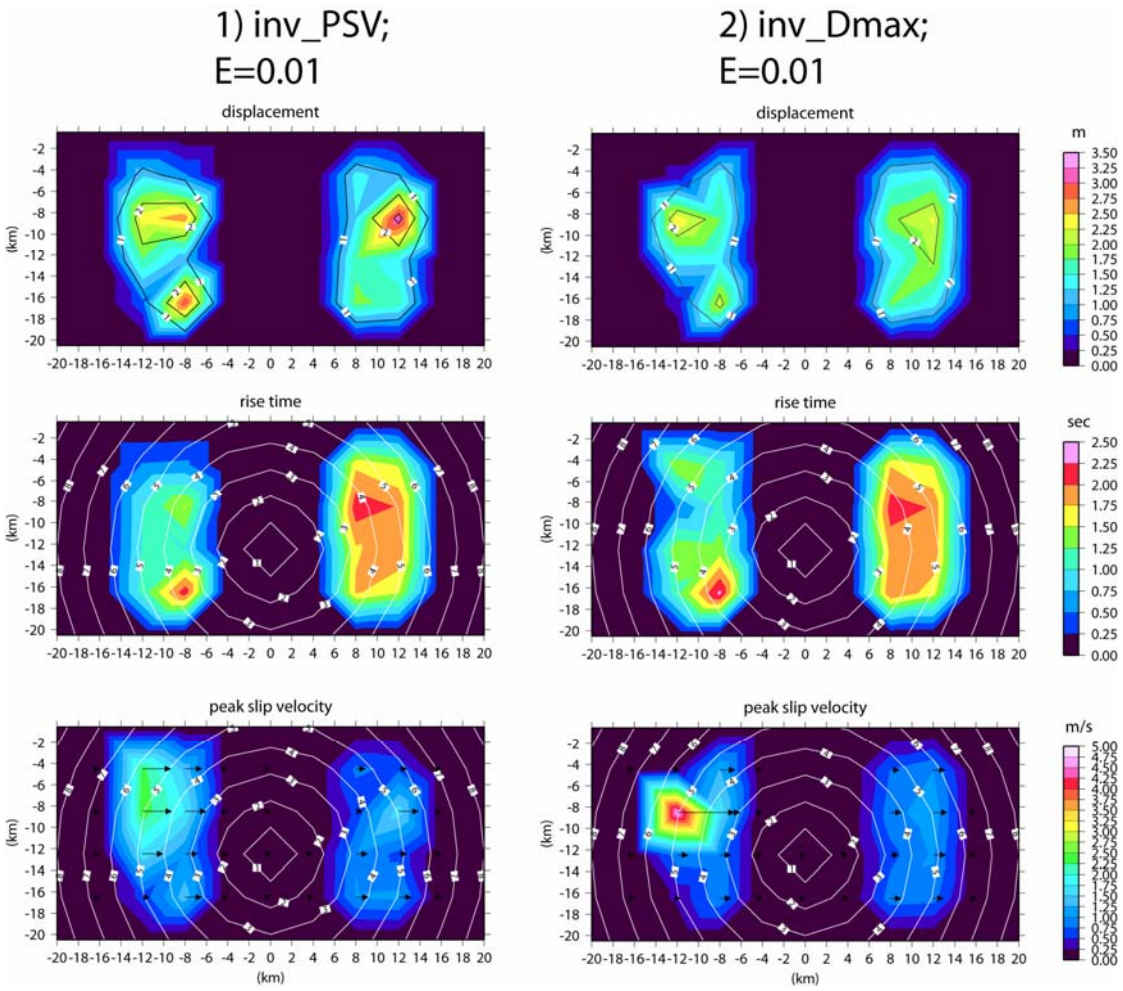

Figure4.2. Inverted rupture models (average model from ensemble inference) from the two synthetic tests performed with a boxcar and obtained inverting for 1) peak slip velocity (*test inv_PSV*; left side) and for 2) slip (*test inv_Dmax*; right side). For each case: top panels show the total slip on the fault; middle panels show the rise time; bottom panels show the peak slip velocity. Rupture time is shown by contour lines. Black arrows represent the slip vector. For each test it is displayed the cost function value (E).

This effect can be highlighted looking at the standard deviation $< \sigma_i >$ associated to the average model of peak slip velocity retrieved from the two synthetic tests (Figure4.3).

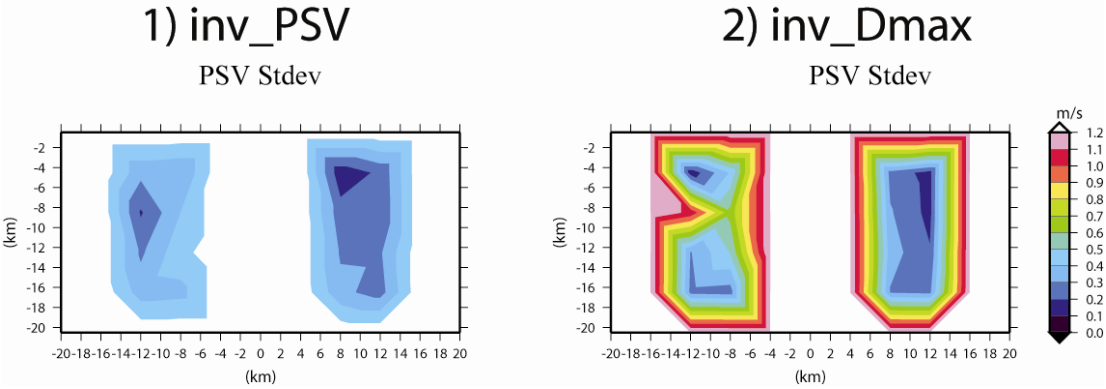

Figure4.3. Standard deviation of peak slip velocity average models, computed through ensemble inference. For each synthetic test performed with a boxcar function and inverting for : 1) peak slip velocity (*test inv_PSV*; left side) and for 2) slip (*test inv_Dmax*; right side).

The standard deviation associated to the peak slip velocity obtained from the inversion of slip (*test inv_Dmax*; right side of Figure4.3) has larger values, and, therefore, larger dispersion, with respect to those obtained from the inversion of peak slip velocity (*test inv_PSV*; left side of Figure4.3). This means that the peak slip velocity values of *test inv_Dmax* are less stable than the values of *test inv_PSV.*

The comparison of the waveforms (see Figure4.4b), for the nearest (SMNH01, d = 8 km) and furthest (TTR005, d = 47 km) stations reveals an almost good match between data and synthetic for both inversions. Besides, the fit between observed and synthetic horizontal displacement vectors, at the selected GPS stations, shows a good match both in amplitude and direction (Figure4.4a).

These behaviors show the intrinsic non-uniqueness of the inverse problem: we could have many rupture models that are consistent with the data.

The obtained results highlight the importance to assess the spatial resolution and the reliability of a solution.

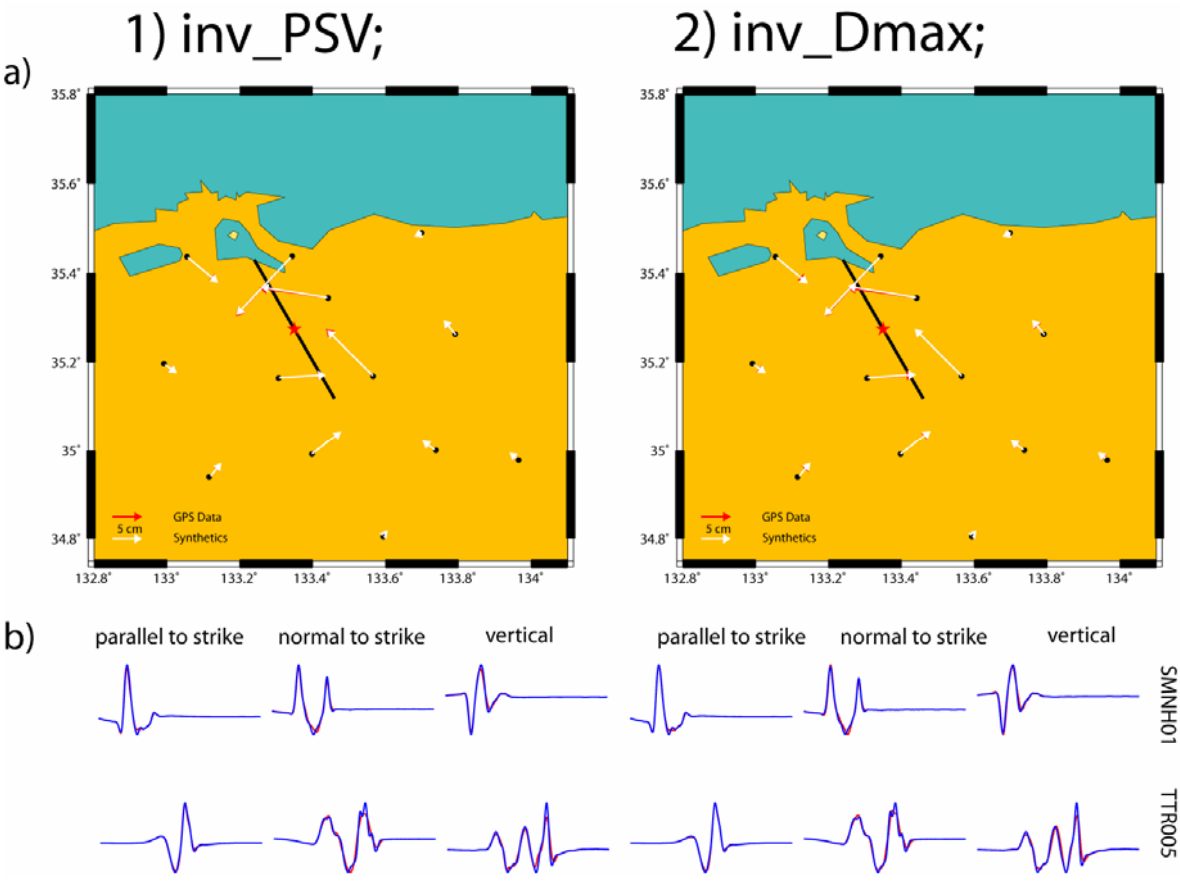

Figure4.4. a) Comparison of synthetic horizontal displacements from the target rupture model (red arrows) with inverted rupture model (white arrows) for each performed test. b) Comparison of synthetic ground velocities from the target rupture model (blue lines) with inverted rupture model (red lines) for each performed test. The comparison it's showed for the nearest (d=8 km; SMNH01) and furthest (d=47 km; TTRO05)stations.

4.2.3 Synthetic test I: Resolution analysis

In this section, we want to quantitatively study the *bias* on the retrieved models introduced by the *a priori* assumption of a particular parameterization scheme.

Following the same framework presented in Section 2.3, we use the term '*bias*' to indicate how an erroneous choice of the model parameterization can produce a not well-retrieved rupture process with respect to the target.

First, considering all rupture models explored by our algorithm, we evaluate, for each kinematic parameter, its weighted residual between the retrieved model and the corresponding target value, normalized to the target itself.

This quantity represents the distribution in percentage of the residual (we call it *res*)*:*

$$res_{jk} = \frac{\frac{1}{E_j}\left(\sum_{i=1}^{N} \frac{m_{ij} - t_i}{t_i}\right)}{\sum_{j=1}^{M} \frac{1}{E_j}} \tag{4.1}$$

where *k* refers to the kinematic parameter (peak slip velocity, total slip, rise time, rupture time and rake).

In the Equation (4.1) m_{ij} represents the value of the parameter assumed on the *i*-th grid-node of the *j*-th model belonging to the ensemble Ω, *M* is the number of rupture models explored by the algorithm and *N* is the number of grid nodes on the fault plane. The weight is the same used to compute the average model and its standard deviation and corresponds to the inverse of the cost function (E_j).

For each distribution of residual (*res*) we compute the mean value (*m*) over all the explored models and the associated standard deviation (*stdev*). In this way, for the two models (*test inv_PSV* and *test inv_Dmax*), we are able to provide a quantitative measure of parameter's dispersion between the target and the retrieved model.

Figure4.5 shows the histograms of the distribution of residual (*res*) for each performed synthetic test (*test inv_PSV* on the left, *test inv_Dmax* on the right) and for the following kinematic parameters; slip, peak slip velocity and rise time (panel *a*, *b*, and *c*, respectively). The mean and standard deviation values are displayed in each single panel of Figure4.5. The mean value, shown through a red bar, tells us how much each retrieved kinematic parameter under/over-estimates the target one.

It is worthy of noting that the two parameterization schemes yield similar residuals distribution of slip (Figure4.5a) and rise time (Figure4.5c), but very different distributions in terms of peak slip velocity (Figure4.5b).

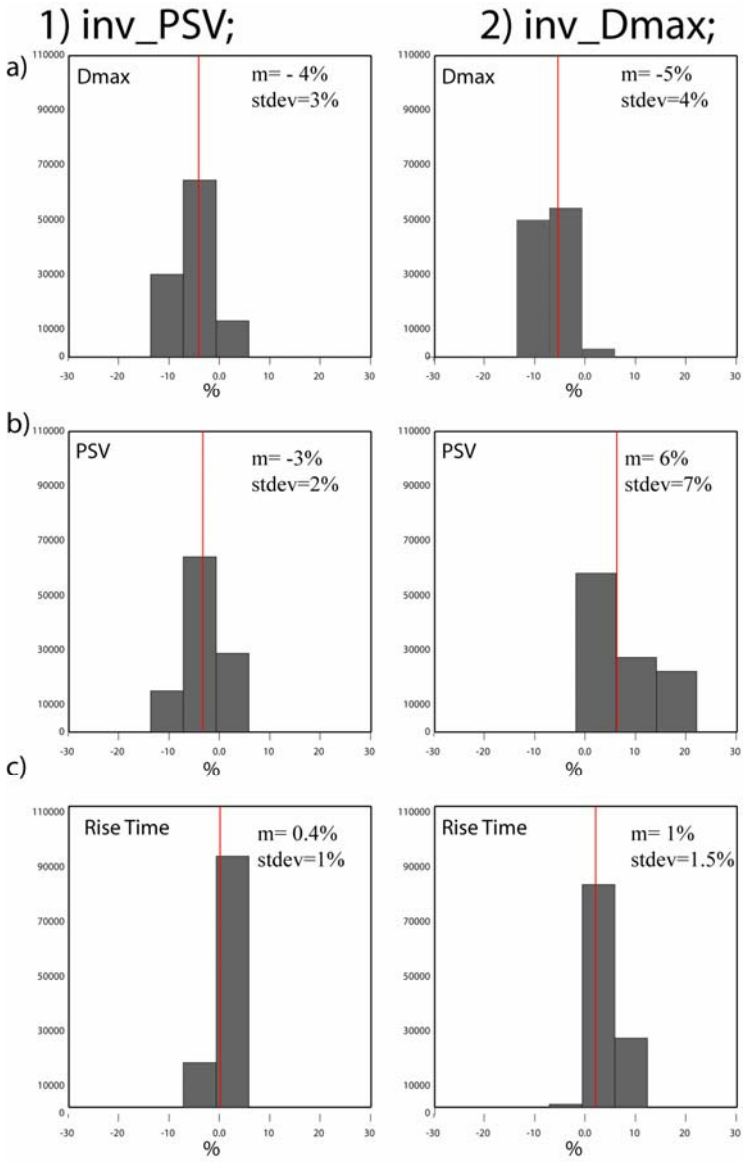

Figure4.5. Histograms of the residual for each synthetic test performed with a boxcar function and inverting for : 1) peak slip velocity (*test inv_PSV*; on left side) ; 2) slip (*test inv_Dmax*; on right side) displayed along columns; and for all kind of parameter; slip, peak slip velocity and rise time (panel *a*, *b*, *c*, respectively) . The red bar indicates the mean value of each distribution. For each distribution it is displayed the mean (*m*) and standard deviation (*stdev*) values.

The synthetic test in which we directly invert for slip displacement and subsequently we derive peak slip velocity values (*test inv_Dmax*), shows that the retrieved peak slip velocities are over-estimated of about 6% (mean value of distribution), with fluctuations that can reach 7% (standard deviation value) with respect to the corresponding target value. The latter estimates are as greater as twice than the corresponding estimates obtained from the test performed by inverting for the peak slip velocity (*test inv_PSV*). This means that if we assume a parameterization scheme based on the direct inversion of slip displacement, we

could retrieve a not-well constrained peak slip velocity distribution., i.e. the choice can affect the reliability of the solution.

The proposed approach allows us to appraise how the choice of a particular parameterization scheme can bias the inverted rupture histories and highlights the importance of assessing the solution stability and spatial resolution to estimate its reliability.

4.3 Dynamically consistent source time function

In the previous section we have studied the effects of the choice of kinematic parameters directly inverted from the data. We underline that the results have been obtained with a different *a priori* assumption: the source time function (STF) used for the target as well as for the two inversions is a boxcar function. In Chapter 2 we have quantitatively verified that an inappropriate choice of STF strongly affects the retrieved rupture models. Besides, recent papers discuss the effect of using different STFs for imaging the distribution of dynamic parameters on the fault plane. In particular, Piatanesi et al. (2004) have shown that even kinematic models that differ only for the choice of STF yield different values of dynamic parameters. On the next Section 4.5 we will show the effects of the a priori assumption of source time functions on the inverted kinematic models for a real earthquake (2000 western Tottori earthquake).

In this section we emphasize the relation between total slip (Dmax) and peak slip velocity (Vpeak), which depends on the adopted STF; then we show that a dynamically consistent source time function may reduce the bias induced on a rupture model by the choice of a parameterization scheme. To this purpose we follow the same approach described in the previous section. We design a target earthquake rupture model and we use the synthetic dataset to recover the original faulting process. To test the reliability and the resolution of the retrieved model, we analyze the consistency between the inversion results and the 'target model'. The main difference between this application and the previous one is the assumed source time function: in this second test we adopt a regularized Yoffe function

with constant value of T_{acc} = 0.4 sec (i.e. time of positive acceleration) all over the fault (see Eq.(1.11c)). This source time function has been recently proposed in the literature because of its consistency with earthquake dynamics (*Tinti et al.*, 2005a; *Fukuyama and Mikumo*, 2007).

4.3.1 Synthetic test II: Target model

We assume the same crustal model, fault geometry and station distributions adopted in the previous synthetic test. We construct a target model with the same slip distribution as in the previous target model; however, owing to a different source time function adopted in this test. Asperity A has a rise time of 4.76 sec and a peak slip velocity of 1.75 m/s, while asperity B has a rise time of 3.06 sec and a peak slip velocity of 2.25 m/s (middle and bottom panel of Figure4.6). The rake angle is 0° on both asperities and the rupture front propagates at 2.5 km/s. We generate synthetic seismograms in the frequency band 0.05÷1.0 Hz and we associate the horizontal component of static displacements to synthetic GPS data. We perform two different inversions, called *test inv_Dmax* and *test inv_PSV*, in which we vary the inverted parameters (see Section 4.2).

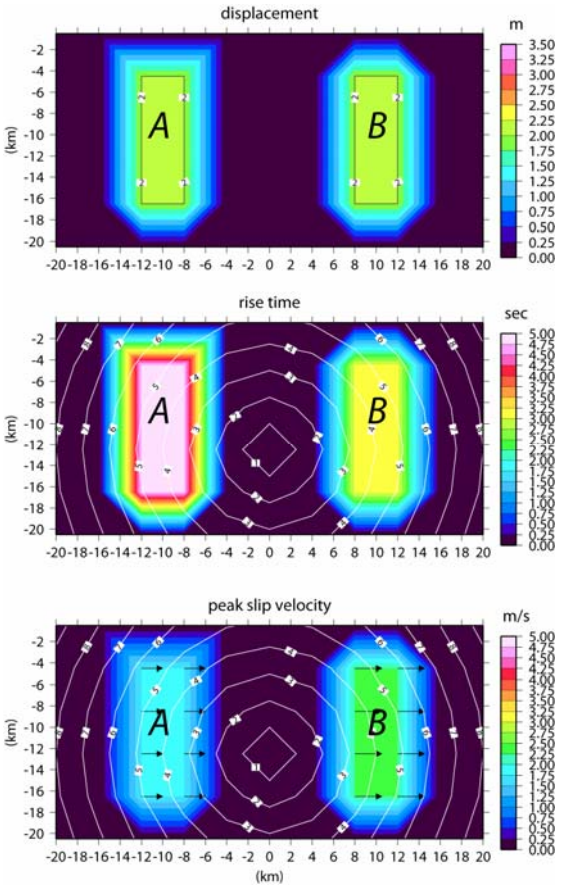

Figure4.6. Target rupture model used in synthetic test II. Horizontal axis is along-strike distance measured from the epicenter. Vertical axis is down-dip distance measured from the ground surface. Top panel shows slip displacement. Middle panel shows the rise time; rupture time shown by contour lines (in seconds). Bottom panel shows peak slip velocity. The slip patches are denoted by capital letters A and B (see text for details). Black arrows represent the slip vector.

4.3.2 Synthetic test II: Results

In Figure4.7 we compare the kinematic source parameters of the average models inferred for both inversions (*test inv_PSV*, on the left side; *test inv_Dmax*, on the right side). We observe fewer differences between the two inversions with respect to the previous synthetic test (performed with a boxcar source time function). Moreover, the peak slip velocity distribution is not so sensitive to the two different kinds of parameterization schemes, and its features are well-constrained and stably retrieved on the entire fault plane. This result is supported by the analysis of the distribution of the residuals (*res*) (see Figure4.8). The mean (*m*) and standard deviation (*stdev*) values associated to each parameter (total slip, peak slip velocity and rise time) are shown in percentage in each panel of Figure4.8. The *bias* on the retrieved models introduced by the a priori assumption of a particular model parameterization (*test inv_Dmax* and *test inv_PSV*) is strongly reduced, compared to the previous synthetic test, especially in terms of peak slip velocity (compare panels b of Figure4.8 and Figure4.5).

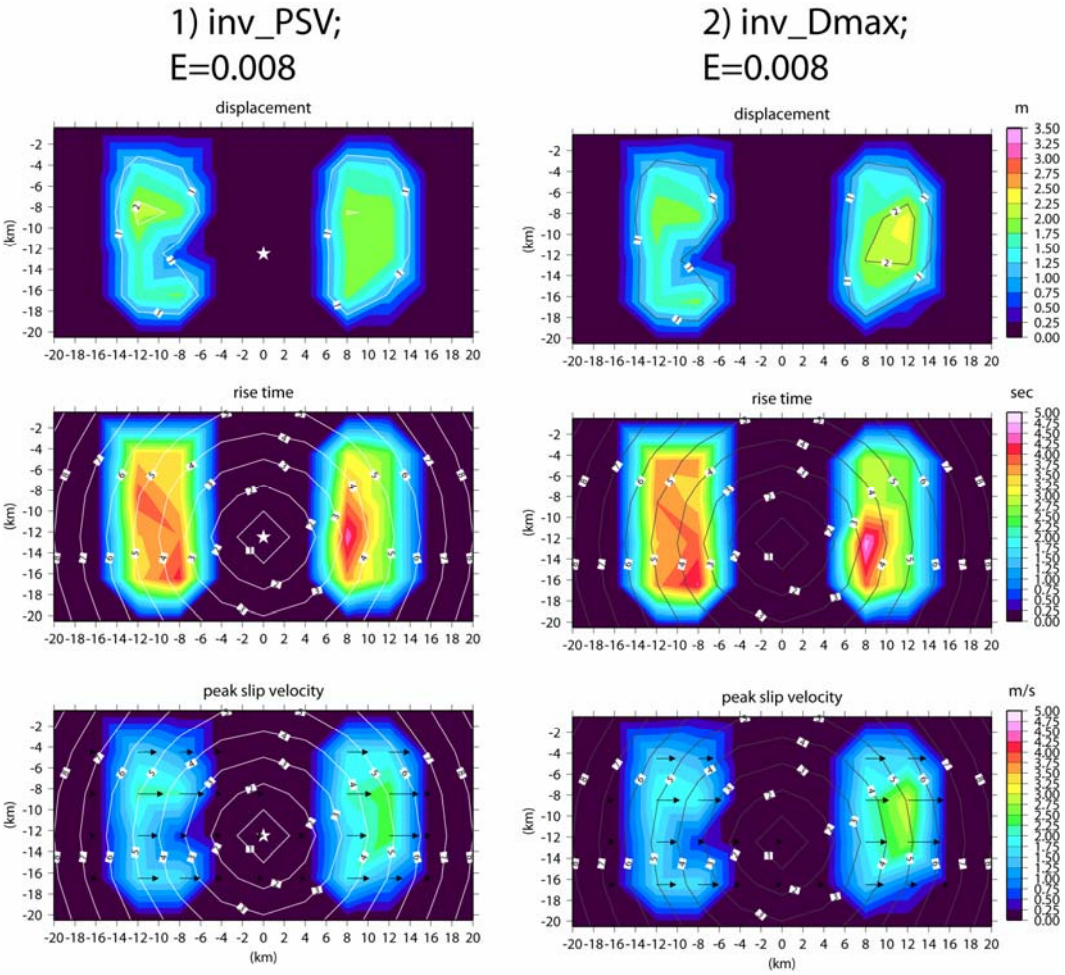

Figure4.7. Inverted rupture models (average model from ensemble inference) from the two synthetic tests performed with a Yoffe function, with T_{acc} equal to 0.4 sec; and obtained inverting for: 1) peak slip velocity (*test inv_PSV*; left side) and for 2) slip (*test inv_Dmax*; right side). For each case: top panels show displacement on the fault; middle panels show the rise time; bottom panels show the peak slip velocity. Rupture time is shown by contour lines. Black arrows represent the slip vector. For each test it is displayed the cost function value (E).

The adoption of a dynamically consistent source time function permits us to reduce the bias induced by the model parameterization and to improve the reliability of the solution.

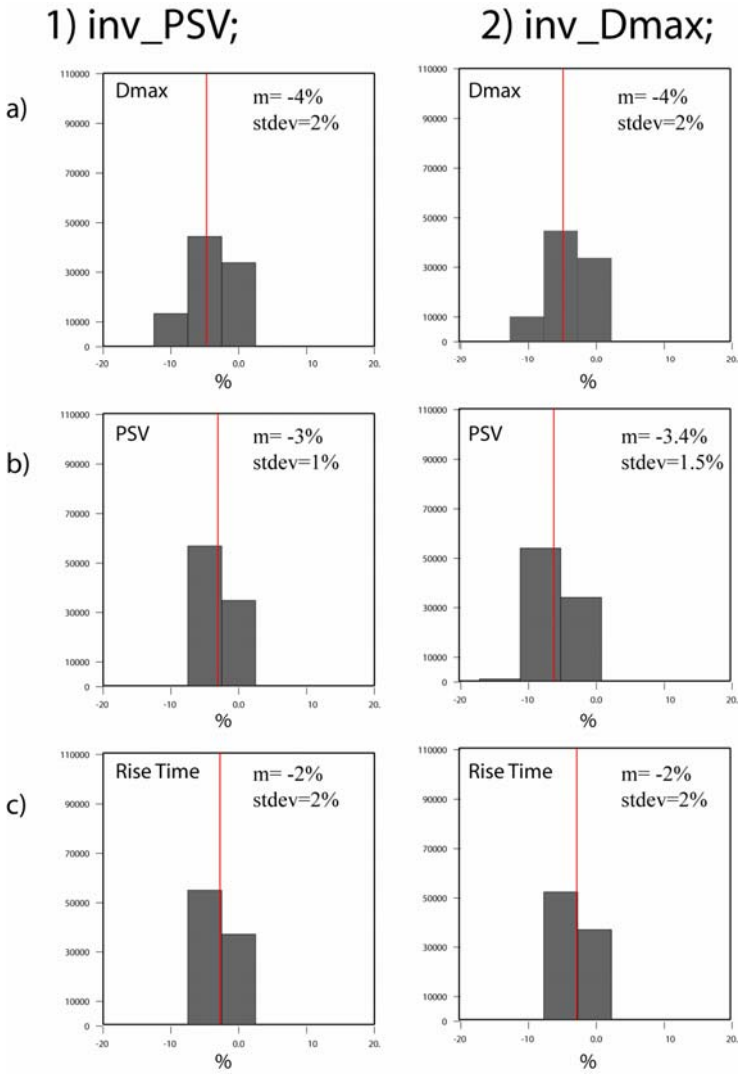

Figure4.8. Histograms of the residual for each synthetic test performed with a Yoffe function and inverting for : 1) peak slip velocity (*test inv_PSV*; left side) and for 2) slip (*test inv_Dmax*; right side) displayed along columns; and for all kind of parameter; slip, peak slip velocity and rise time (panel *a*, *b*, *c*, respectively). The red bar indicates the mean value of each distribution. For each distribution it is displayed the mean (*m*) and standard deviation (*stdev*) values.

4.4 Proposals

Many recent papers have investigated the limitations of using poorly resolved kinematic source models (*Guatteri and Spudich,* 2000; *Beresnev,* 2003).

In this study we have proposed an approach to evaluate how a particular model parameterization can bias the imaged kinematic rupture histories. We have shown several sensitivity synthetic tests in order to study the effects of parametric uncertainty. Our results emphasize that the peak slip velocity, among all kinematic parameters, is strongly sensitive to the choice of the model

parameterization. We want to highlight that the peak slip velocity is an important kinematic parameter of the earthquake source; it contains information on the underlying dynamic process. In spontaneous dynamic modeling, peak slip velocity can change dramatically during the dynamic rupture process, because of the heterogeneity of the dynamic parameters on the fault. Moreover, the inferred linear relation between peak slip velocity and breakdown-stress drop, (*Ohnaka and Yamashita*, 1989) points out that peak slip velocity is related to the mechanisms controlling the breakdown process and to the earthquake stress drop. All these aspects suggest us the use of robust inferred kinematic models. The modeler has to carefully choose the independent kinematic parameters to be inverted, and tests the capability to constrain simultaneously peak slip velocity and slip displacement on the fault plane. These source parameters are important when kinematic rupture models are used to infer dynamic parameters, as we will show in the next section.

4.5 Dynamically constrained kinematic inversion

Understanding shear traction evolution during dynamic propagation of earthquakes is one of the major task for seismologists. Dynamic fault weakening can be fully described by the total shear traction evolution at a target point on the fault plane as a function of time or slip (*Rice and Cocco*, 2006), and it is characterized by the stress degradation near the propagating rupture front. The shear stress drops from an upper yield value (τ_y) to a residual level (τ_f, dynamic frictional stress) in an extremely short time, called the breakdown time (T_b), and over a characteristic slip, called the slip weakening distance (D_c). The spatial extent of the breakdown zone (or cohesive zone), defined as the region of shear stress degradation near the tip of a propagating rupture, depends on the slip weakening distance. Constraining the traction evolution is an extremely important but very difficult task for modeling the earthquake source.

Several stress parameters can be defined from the traction evolution (*Mikumo and Miyatake*, 1995; *Bouchon*, 1997): the strength excess ($\tau_y - \tau_o$), the dynamic stress drop ($\tau_o - \tau_f$) and the breakdown stress drop ($\tau_y - \tau_f$); where τ_o is the initial value of

stress for a particular position on the fault plane (Figure4.9). These parameters allow us to study the dynamic traction evolution within the cohesive zone and to understand the physical processes controlling the weakening, hardening and healing mechanisms (i.e., the slip duration during the dynamic rupture propagation).

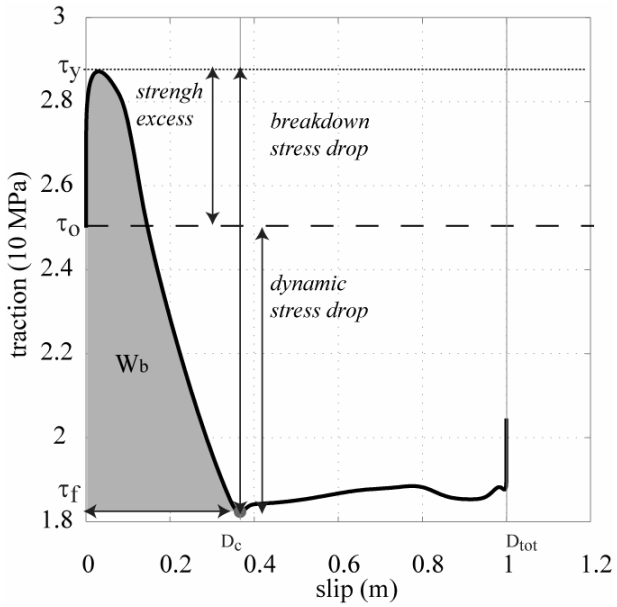

Figure4.9 Classical slip weakening curve proposed in the Andrews' model (*Andrews*, 1976). In this plot τ_o is the initial stress, τ_y and τ_f are the yield and the residual stress values, respectively. D_{tot} is the final slip and D_c is the slip weakening distance.

Different papers, studying dynamic processes of earthquakes, adopt the kinematic inversion results as input to infer the dynamic source parameters (e.g. *Bouchon* 1997; *Ide and Takeo*, 1997; *Dalguer et al*., 2001a, 2001b ; *Piatanesi et al*., 2004 among several others) and to determine scaling properties (*Mai and Beroza*, 2002). Then, the reliability and accuracy of kinematic inversion of earthquake rupture history must be taken into account and carefully investigated, to avoid an erroneous interpretation of the real rupture processes. In this section we focus our attention on the importance of adopting dynamically consistent source time function to retrieve kinematic rupture model. The temporal evolution of dynamic traction on the fault plane is obtained by the slip time history, consequently the choice of the source time function might strongly affect the inferred dynamic parameters. There is still an open debate within the scientific community on those dynamic inferences *(Guatteri and Spudich,* 2000*)* and several recent works have

emphasized that the adopted parameterization in kinematic source modeling could strongly bias the measure of dynamic quantities.

We want to contribute to this debate by estimating the dependence of traction evolution on the source time function adopted to model kinematic rupture histories on a finite fault. To this goal, we present an application to a real earthquake.

4.5.1 Methodology

To infer the kinematic rupture model, we jointly invert velocity waveforms and GPS data from the 2000 western Tottori earthquake, applying our nonlinear inversion technique. In this procedure, the spatio-temporal evolution of rupture on the fault plane is obtained assuming an analytical expression for the source time function (single window approach inversion). We select four distinct source time functions: a boxcar, a modified cosine, and two regularized Yoffe functions, characterized by different values of positive acceleration time (T_{acc}), (see Figure2.9). The functional forms and a detailed description of the adopted STFs are given by the Eq.(1.11a- 1.11b- 1.11c) in Section 1.6. We invert for peak slip velocity, rise time, rupture time, rake, and then we compute the corresponding slip distribution. For each assumed STF the result is a kinematic rupture model, characterized by five source parameters spatially variable on the fault (peak slip velocity, rake, rupture time, rise time and slip amplitude). Each kinematic parameter distribution is obtained through a statistical analysis of the entire model ensemble; this allows us to quantitatively draw the average model, weighted among all possible rupture models (see Eq.(1.20), Section 1.6), and the associated standard deviation (see Eq.(1.21), Section 1.6). The slip velocity histories of the obtained kinematic models are then used as boundary condition on the fault plane to compute the temporal traction evolution (*Day et al*., 1998) by solving the elasto-dynamic equation. The traction evolution enables us to infer the spatial distribution of dynamic and breakdown stress drop, and the critical slip weakening distance (D_c), for the four different kinematic rupture models. To compute the dynamic traction time history on the fault plane, we employ a 3-D finite

difference code (*Andrews*, 1999). The fault is represented by a surface containing double nodes and the stress is calculated through the fundamental elasto-dynamic equation (*Ide and Takeo*, 1997). The total dynamic traction in each fault location is computed by the sum of two terms: the instantaneous contribution that depends on the slip velocity and the dynamic load that allows for the previous slip history. This dependence has been analytically formulated by Fukuyama and Madariaga (1998), through the following equation:

$$\sigma(x,t) = \frac{\mu}{2Vs} s(x,t) + \int_{\Sigma} \int_{0}^{t} K(x-\xi;t-t')s(\xi,t)dt'd\Sigma \qquad (4.2)$$

where *s(x,t)* represents the slip velocity, *Vs* the shear velocity, μ the rigidity, *K* the dynamic load associated to those points that are still slipping and Σ is the area of the fault plane. We show this formulation only to highlight the direct effect of the local source time function on the corresponding traction evolution. In the present study we impose the slip velocity as a boundary condition on the fault. In other words, each node belonging to the fault plane is forced to move with a prescribed slip velocity time history and the stress change is determined everywhere on the fault plane. This approach does not require to specify a constitutive law and the dynamic traction evolution is a result of the calculations.

4.5.2 Kinematic inversion: Applications to the 2000 western Tottori earthquake

We assume the geometry, station distributions and crustal model of the 2000 October 6, western Tottori Prefecture earthquake (Mw=6.6).

The data (waveforms and GPS measurements) are processed and weighted following the same procedure described in Section 3.2.1. We perform four different kinematic inversions adopting four different STFs: a boxcar, a modified cosine and two regularized Yoffe functions with T_{acc} of 0.225 sec and 0.400 sec, respectively (Figure2.9). The fault plane is subdivided through 66 nodal points equally spaced along strike and dip every 4 km. Each node is characterized by four model parameters: peak slip velocity, rake angle, rise time and rupture time. We simultaneously invert all parameters, setting suitable bounds for each of them:

the peak slip velocity varies from 0.0 to 7.0 m/s with 0.25 interval; the rake angle goes from -15° to 15° by steps of 5°; the rise time ranges between 1 and 5 sec at 0.5 sec interval; the rupture time is bounded by the times for a rupture to reach the node traveling at 2 and 4 km/sec from the hypocenter. For each performed inversion, the algorithm explores about 2 millions rupture models, finds the best fitting model, calculates the weighted average model, and the associated standard deviation.

4.5.3 Results: Kinematic parameters and data fit

In Figure4.10 we compare the kinematic source models retrieved by the inversions performed with the four different source time functions. For all four cases the weighted average model shows two different patches of slip (top panels of Figure4.10). Slips occurs mainly at the shallower part of the fault, above the hypocenter and goes down in SE dip direction with at most 3.0÷3.5 m left lateral slip, except for the boxcar that yields a slightly higher value (about 4÷4.5 m). This major patch extends from the upper border to a depth of 6 km with a length of about 12÷14 km. Little slip occurs deeper, between 12 and 18 km depth, in NW direction from the hypocenter. All four models show a similar shape of displacement distribution and a resulting seismic moment of about 1.7×10^{19} Nm, in agreement with the results obtained in previous studies (*Semmane et al*., 2005; *Festa and Zollo*, 2006; *Piatanesi et al*., 2007) . For very similar slip distribution (top panels of Figure4.10), the different STFs yield very different peak slip velocity and rise time distributions (Figure4.10: middle and bottom panels, respectively) especially in terms of amplitude. The source time function with the steepest initial slope (Yoffe with T_{acc}=0.225s), yields greater values of peak slip velocity. The slip direction (rake angle), shown with black arrows in the bottom panels of Figure4.10, clearly indicates left lateral strike slip mechanism for all the inversions.

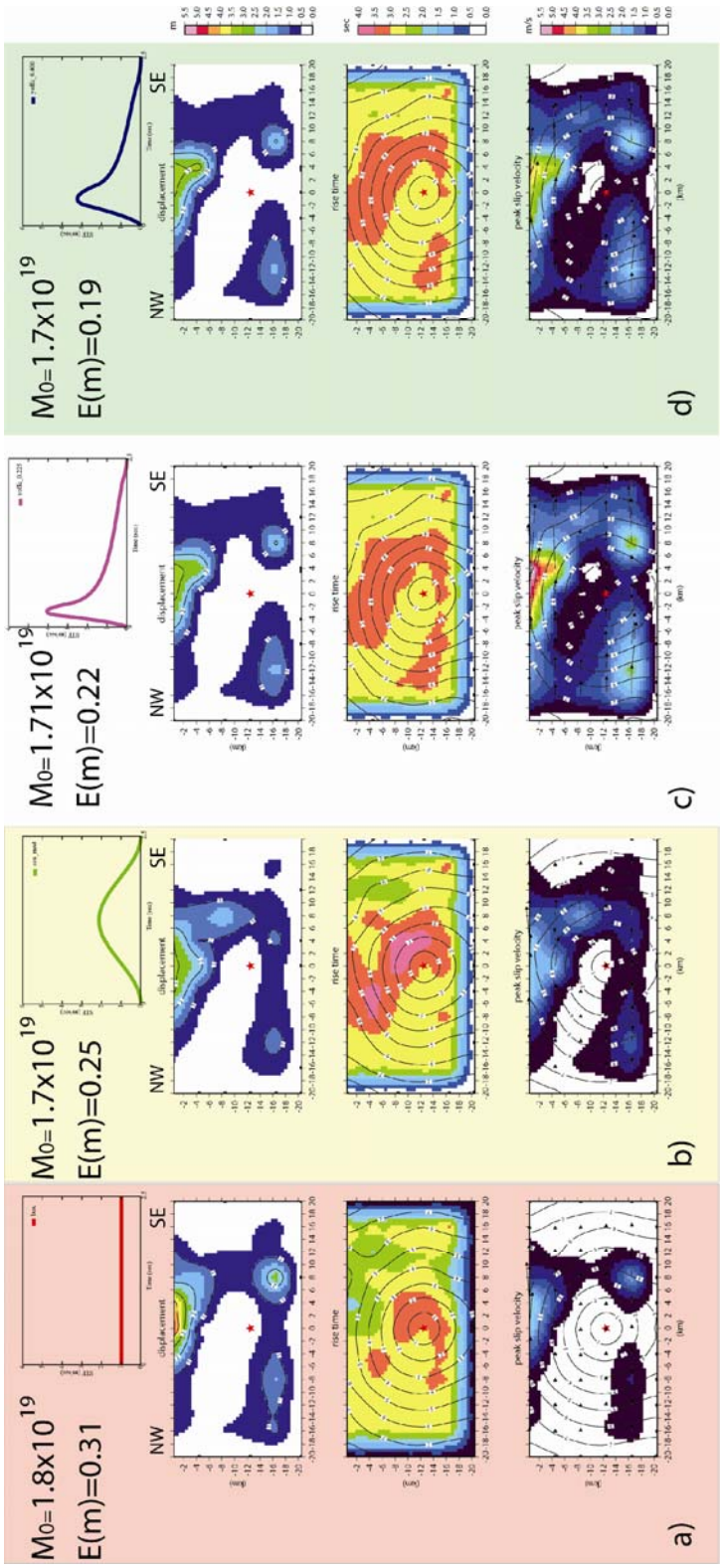

Figure4.10. Retrieved rupture histories obtained for the Tottori earthquake adopting: a) a boxcar; b) a modified cosine; c) a regularized Yoffe with T_{acc}= 0.225sec; d) a regularized Yoffe with T_{acc}= 0.400sec. Top panels display displacement distribution on the fault, middle and bottom panels show rise time and peak slip velocity, respectively. Black arrows indicate rake angle. Rupture time is shown by contour lines. Average model parameter are shown. For each performed inversion are specify the reached minimum cost function (E) value and the seismic moment recovered (in Nm).

The rupture propagation is quite similar for all adopted source time functions: it's slightly faster along strike (< v_r > = 2.6 km/s) than along up-dip direction (< v_r > = 2.2 km/s). The total rupture duration is about 8 s. Although the strong similarity, overlapping the rupture fronts retrieved from the different STFs (see Figure4.11), we can see that ruptures generated by the two regularized Yoffe functions are slower than those produced by a boxcar or a modified cosine function and feature an almost regular front.

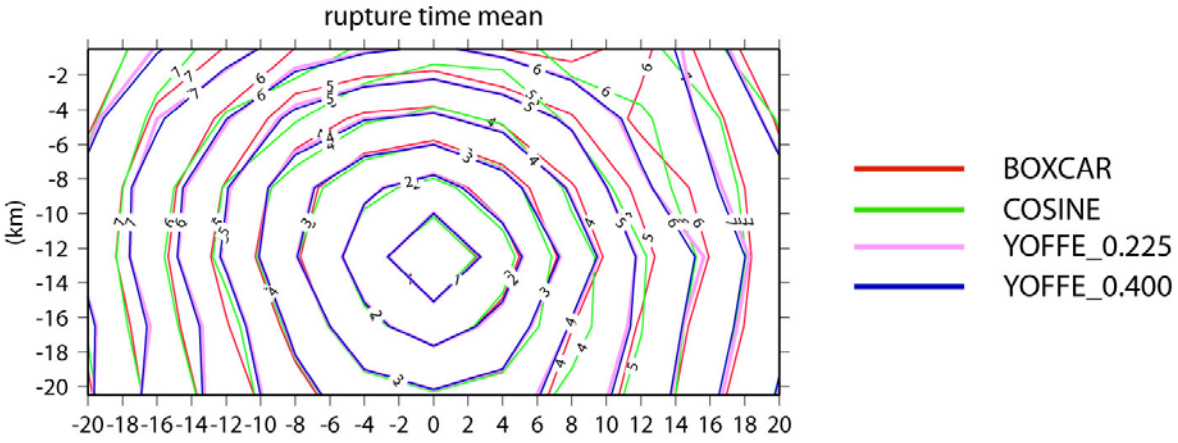

Figure4.11. Overlap of the rupture front (in km/s) retrieved from the four different inversions. The legend shows the adopted STFs.

Finally, in Figure4.12 is shown the comparison between the data and the synthetic for the waveforms dataset (Figure4.12a) and for GPS measurements (Figure4.12b), obtained from the retrieved model reaching the smallest cost function value (E(m)=0.19). This model corresponds to the regularized Yoffe function with T_{acc}=0.400 sec.

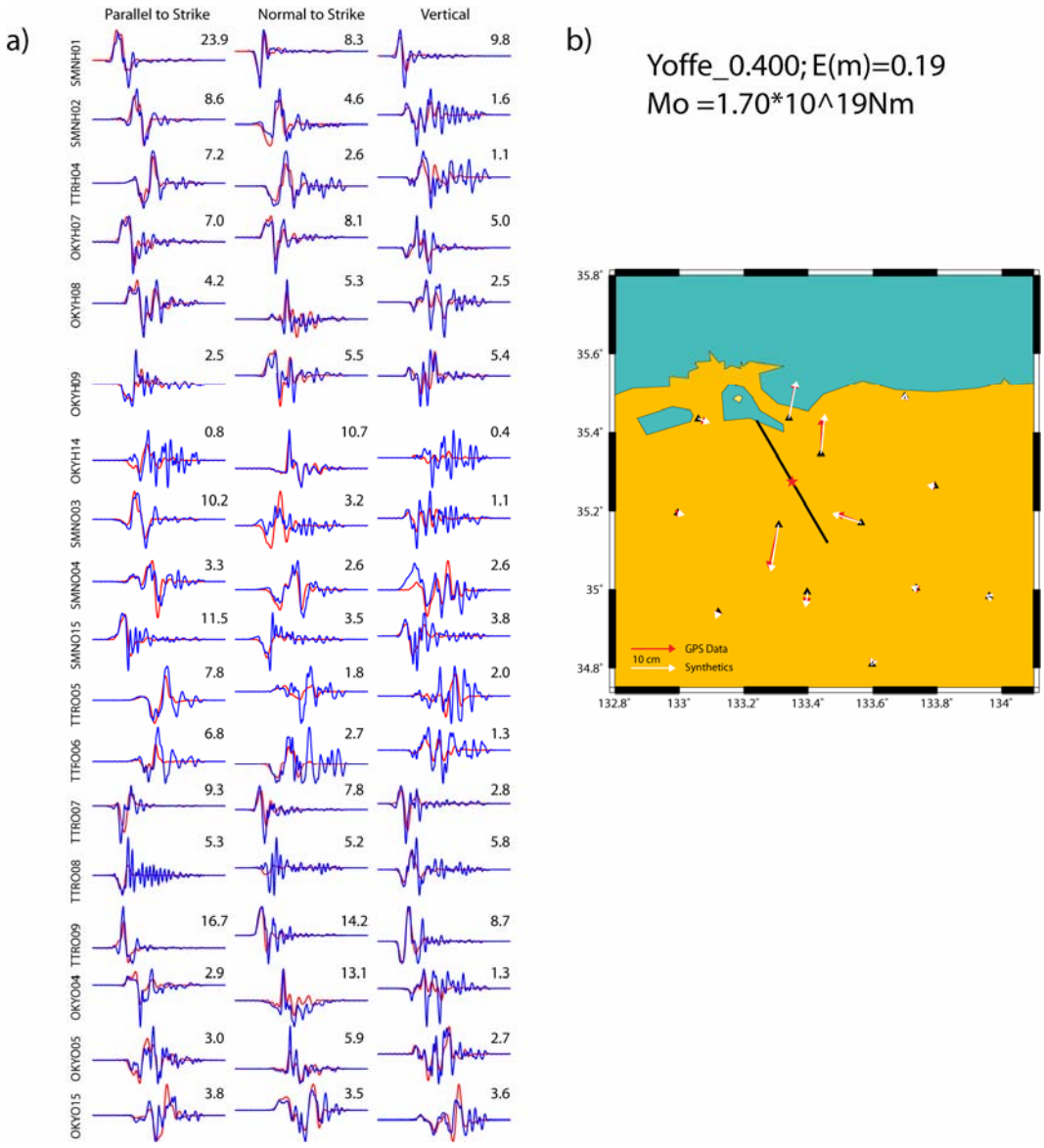

Figure4.12. a) Comparison between the observed (blue lines) and the synthetic (red lines) waveforms; b) comparison between the recorded (red arrows) and the predicted (white arrows) GPS horizontal displacements. The synthetic data refer to the retrieved model having the smallest cost function value (E(m)=0.19). This model is obtained from a regularized Yoffe with T_{acc}=0.400 sec. Numbers with each trace are maximum peak velocity (cm/s).

4.5.4 Results: Appraisal of the ensemble

In general, the kinematic source models retrieved from inversions are affected by uncertainties of different type and origins. The knowledge of the inherent non-uniqueness in kinematic parameters is important. To this purpose, as we did in Section 2.3.1, we analyze the coefficient of variation (CV) associated with the

average models, which are inferred from the ensemble of rupture models explored by the algorithm.

In Figure4.13 are shown the coefficient of variations of the peak slip velocity (top panels) and rise time (bottom panels), for the different rupture models.

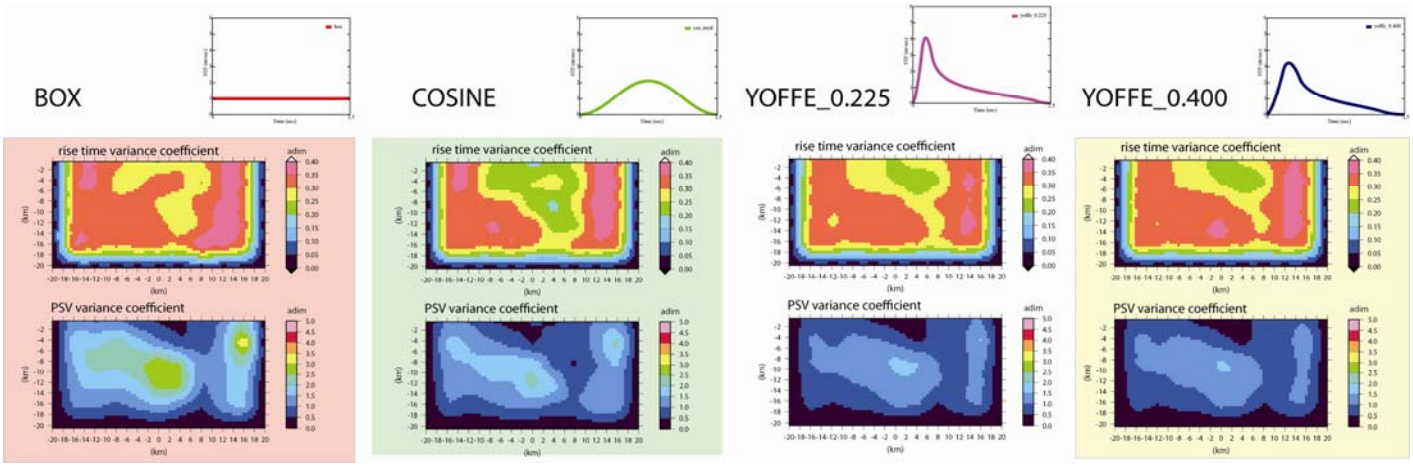

Figure4.13. Coefficient of variation of average models, computed through ensemble inference. For each test performed: top panels show the coefficient of variation corresponding to the peak slip velocity distribution ; bottom panels show the coefficient of variation of the rise time.

Focusing the attention on the areas of the fault that are characterized by higher slip values, we may appreciate that the rupture model is stably inverted there. For each case, it should be noted that large values of CV correlate to regions of the fault with a small amount of slip; this demonstrates that those areas don't contribute to the ground motion and cannot be constrained by the inversion.

A statistical analysis of the retrieved rupture models allows us to indicate which are the well resolved areas of the fault plane.

4.6 Dynamic Modeling

We find that the choice of the source time function affects the retrieved rupture histories, especially in terms of peak slip velocity and rise time distributions, which are crucial when kinematic rupture models are used to infer dynamic parameters.

In this section we discuss the evolution of the dynamic traction histories inferred for the four imaged kinematic models.

Figure4.14 shows, for each dynamic model, the comparison of traction versus slip curves for ten neighboring points around the maximum slip. These points are located on the top of the fault plane, in correspondence of the main patch of the inferred slip distributions (see Figure4.10).

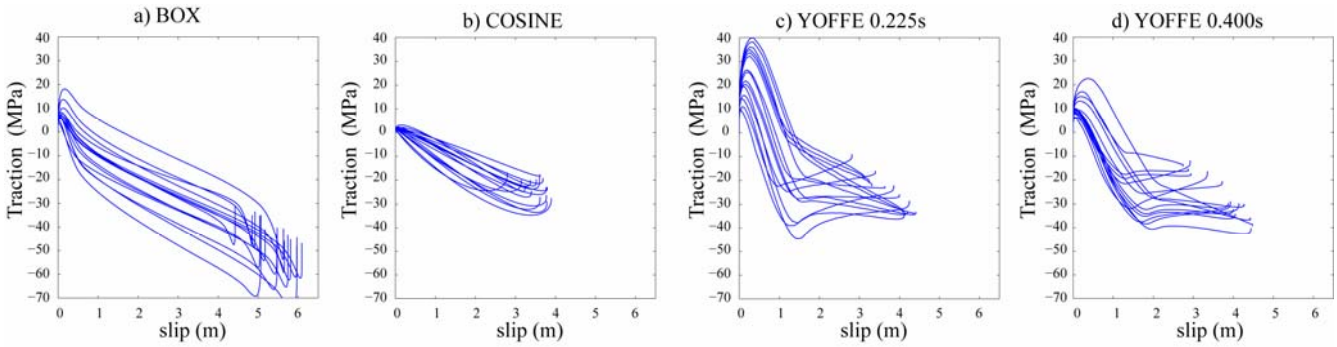

Figure4.14. Traction versus slip curves for 10 neighboring points around the maximum displacement for the four models inferred with (a) a boxcar ; (b) a cosine; (c) a Yoffe with T_{acc}= 0.225 sec; (d) a Yoffe with T_{acc}= 0.400 sec.

Although all the curves exhibit a slip weakening behavior, these plots show different features. The dynamic model derived from the boxcar function (panel a) displays reduced hardening phases and a nearly constant and slow weakening rate during the total increase of slip. Therefore, the end of the weakening phase approximately corresponds to the healing phase, that is D_c is a large fraction of total slip ($D_c/D_{tot} \sim 0.9$). The traction-slip curves derived from the cosine function (panel b) show similar characteristics with a more reduced hardening phase. Finally, the two models derived from the Yoffe functions (panels c and d), have more similar peculiarities; they show an unambiguous hardening phase followed by a weakening phase and by an almost constant value of traction before the healing phase. The initial slip hardening phase that precedes the dynamic

weakening phase it is associated with relatively small slip amplitudes. These latter plots are very similar to those inferred through spontaneous dynamic modeling using different constitutive laws (such as slip weakening law or rate- and state-dependent laws).

Figure4.15 shows the time history of slip, slip velocity and dynamic traction calculated for a particular target point (close to the maximum slip on the fault plane). These plots clearly highlight how the different source time functions control the traction histories.

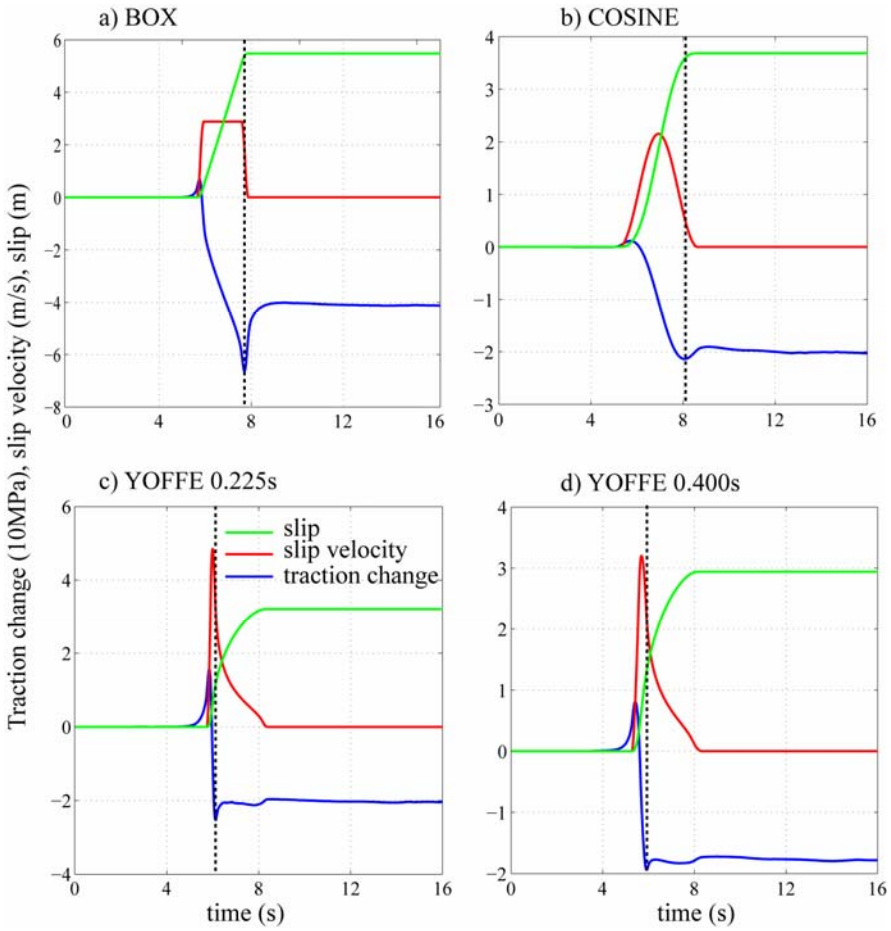

Figure4.15. Dynamic traction, slip and slip velocity time histories for one of the subfault around the maximum slip inferred from the four models characterized by: (a) a boxcar ; (b) a cosine; (c) a Yoffe with T_{acc}= 0.225 sec; (d) a Yoffe with T_{acc}= 0.400 sec.

For the boxcar function (panel a) the traction is very similar to the slip evolution because it has a constant rate up to the healing phase. Besides, we observe an evident traction restrengthening after the end of the rise time. For the cosine function (panel b), the traction results smoother and still shows a gradual

weakening phase for the nearly total duration of the slipping phase. For the Yoffe functions (panels c and d) we observe a sharp weakening phase that reaches the minimum value (dynamic stress drop) just after the peak of slip velocity. Therefore the traction evolution shows a plateau before the healing phase followed by a small restrengthening during the healing phase. In these two latter panels, the loading of other slipping points (second term of Eq.(4.2)) is significant and is showed by the increase of the traction before the rupture time, while the local effect of the slip velocity (first term of Eq.(4.2)) dominates during the weakening phase.

From the inferred slip weakening curves we can measure D_c, the breakdown stress drop and other dynamic parameters at each point on the fault plane.

Slip weakening distance is one of the parameters to describe the dynamic fault rupture process. To date, the physical interpretation of D_c is still debated in the literature. Several seismologists have investigated the critical slip weakening distance by theoretical studies (e.g., *Ida*, 1972; *Andrews*, 1976), from laboratory experiments (e.g., *Okubo*, 1989) and on the basis of seismic waveform observations (e.g., *Ide and Takeo*, 1997; *Olsen et al*., 1997; *Guatteri and Spudich*, 2000). Pulido and Irikura (2000), Spudich and Guatteri (2004) and Peyrat et al. (2001), among several others, found D_c proportional to the final slip (D_{tot}): D_c ranges between 20% and 90% of D_{tot}. The correlation between D_c and D_{tot} has been reported in many other papers (*Zhang et al*., 2003; *Tinti et al*., 2005a). However, Piatanesi et al. (2004) pointed out that in the kinematic modeling the use of source time functions not compatible with the dynamic rupture propagation could bias the estimate of D_c and hence the inferred values of D_c/D_{tot}. These results raise the question on the actual size of Dc, whether it is proportional to the final slip and if it can be scaled with some other quantity such as seismic moment. Actually, the D_c parameter is strongly dependent on the shape of the STF.

In Figure4.16 we show the histograms for the distribution of D_c/D_{tot} for the four dynamic models. The boxcar function gives most of the values around 1 (that is D_c is 95% of D_{tot}); the cosine function shows values spread out around 0.9; and the two Yoffe functions show values around 0.3÷0.4. These values are computed through an automatic procedure and for the two latter panels it can occur that the

D_c parameter is picked around 100% of total slip when the plateau after the weakening rate is not completely flat (see the traction versus slip curves in Figure4.14, panel c and d). However, even for those points the D_c parameter is around 30÷40 % of total slip.

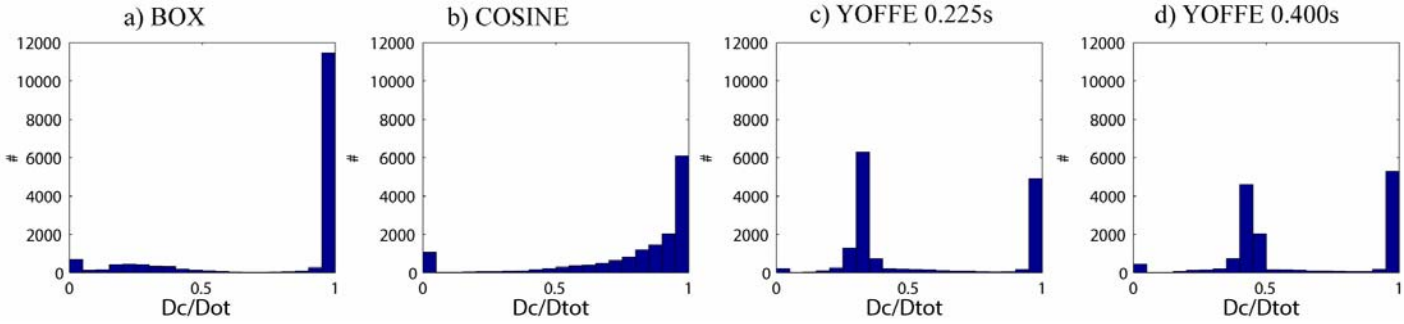

Figure4.16. Histograms for the distribution of D_c / D_{tot} for the four models inferred with: (a) a boxcar ; (b) a cosine; (c) a Yoffe with T_{acc}= 0.225 sec; (d) a Yoffe with T_{acc} = 0.400 sec.

Finally, we have computed the breakdown work distribution on the fault plane for the four different models. Tinti et al. (2005b) have defined the breakdown work (W_b) as the area below the slip weakening curve and above the residual stress level (τ_f). This quantity represents the excess of work over the minimum traction level achieved during slip, and it has been proposed as an alternative measure of seismological fracture energy.

We compute W_b as the integral of the traction versus slip curve from zero slip to the point where the traction drops to the minimum level of traction during slip.

Figure4.17 shows the W_b distribution on the fault plane for all the four models: the boxcar (panel a) yields the highest values (average value: 7.56×10^6 J) while the cosine and the two Yoffe functions give quite similar W_b distributions (average values: 3.97×10^6 J (cosine); 4.51×10^6 J (Yoffe_0.225sec); 4.65×10^6 J (Yoffe_0.400sec)). These features agree with the results obtained by recent studies: Tinti et al (2005b) have concluded that estimates of W_b might be stable despite the poor resolution in the kinematic source model, in agreement with Guatteri and Spudich (2000). The average W_b inferred for the boxcar model is slightly overestimated with respect to the others models. This is probably due to the inherent unphysical properties of the boxcar function.

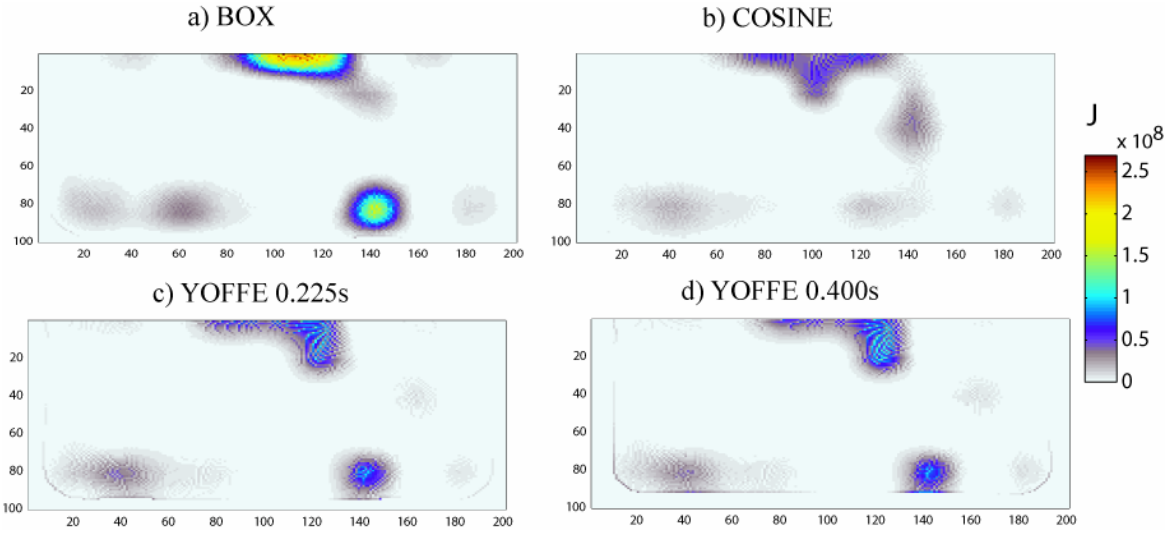

Figure4.17. Breakdown work (W_b) distribution on fault plane, for the four models inferred with: (a) a boxcar ; (b) a cosine; (c) a Yoffe with T_{acc}= 0.225 sec; (d) a Yoffe with T_{acc}= 0.400 sec.

These differences are due to the variability of the critical slip wakening distance and to the ratio D_c/D_{tot} ; as we have seen, for the boxcar D_c is close to 95 % of total slip (Figure4.16) and, as a consequence, the breakdown stress drop is reached at the end of the slipping phase. Only the two Yoffe STFs yield traction evolution versus slip curves (Figure4.14) consistent to what expected from a slip weakening model and D_c is around 30 % of total slip. Furthermore, the different STFs show evident differences between the duration of the breakdown phase and the slip duration (Figure4.15). These features may therefore have important effects on the energy balance of the rupture process.

4.7 Discussion

Kinematic source models obtained by inverting seismic and geodetic data provide a detailed image of the slip history during the earthquake rupture process. One fundamental purpose of these kinematic inversions is to improve our understanding of the physical process governing the dynamic propagation. These kinematic inversion models have been often used as input data to infer the dynamic source parameters of real earthquakes, without paying much attention on their reliability and accuracy. Tinti et al. (2005b) have discussed in detail the fidelity of calculations of some dynamic parameters. Some of the difficulties in

constraining these parameters arise from the *a priori* assumptions made on the kinematic models.

In this study we have proposed an approach to evaluate how the choice of a particular source model parameterization can bias the imaged kinematic rupture histories. We have performed several sensitivity synthetic tests to study the effects of parametric uncertainty. The results obtained from the sensitivity tests highlight the difficulty, in an inversion procedure, to jointly constrain slip displacement and peak slip velocity and show how the parameterization scheme could affect the resolution and reliability of the inferred parameters describing the rupture history on a finite fault.

This effect is particularly evident for the peak slip velocity; in some cases this parameter may be poorly constrained. We have found that for a parameterization scheme which inverts for slip displacement and rise time (*test inv_Dmax*), the peak slip velocity is not-well constrained with respect to that one obtained from the inversion of peak slip velocity and rise time (*test inv_Psv*). This means that two different parameterization schemes don't provide the same solution and that the peak slip velocity is particularly sensitive to the choice of model parameterization.

Moreover we have seen that in a single-time window approach, where the source time function is assumed *a priori*, the choice of a particular functional form is crucial, because it affects the capability to retrieve and to constrain the kinematic parameters. We have quantitatively verified that adopting a source time function compatible with earthquake dynamics reduces the bias induced by the parameterization uncertainty and stabilizes the inversion of the rupture history on a finite fault.

In light of the obtained results, we suggest the use of peak slip velocity parameterization scheme, rather than slip, and recommend the use of source time functions dynamically consistent with the earthquake rupture processes. The proposed parameterization scheme mitigates the bias due to parametric uncertainty and it is able to stably retrieve and to well-constrain rupture history on a finite fault.

In a second step, we have focused our attention on the importance of adopting source time functions (STFs) compatible with earthquake dynamics in order to image the kinematic rupture history of real earthquakes, and we have shown the effects of the retrieved kinematic models on the dynamic parameters.

Adopting different source time functions, we have performed different joint kinematic inversions of real dataset (strong motion and GPS measurement observed during the 2000 western Tottori, Japan earthquake).

We have quantitatively verified that the choice of the STF affects the inverted rupture model, and that the inferred peak slip velocity and rise time strongly change among the inverted models.

These differences have a dramatic impact when kinematic models are used to infer dynamic parameters. In order to appreciate the dependence of these latter quantities on the STF adopted in kinematic input model, we have employed the inverted rupture histories as boundary conditions in dynamic modeling to calculate the traction evolution on the fault. Once traction and slip time histories are inferred at each point on the fault plane, we have estimated the dynamic and breakdown stress drop, the slip weakening distance (D_c) and the breakdown work (W_b). We have found that relevant dynamic parameters of the rupture process definitely depend on the source time function assumed in the inverse procedure to retrieve the kinematic models.

The dynamic traction evolution, the shape of the slip weakening curve, the ratio between D_c and the final slip, and the breakdown work distribution are remarkably affected by the adopted source time functions.

We recommend the adoption in kinematic inversions of source time functions that are compatible with earthquake dynamics.

Chapter 5

Ground motion modeling and radiated seismic energy

5.1 Introduction

In the previous chapter we have focused our attention on the parametric uncertainty and on the dynamic consistency of the kinematic rupture models inferred from the inversion of seismic and geodetic data. We have found that the retrieved rupture models could be strongly affected by the choice of the source time function.

In the present chapter we will devote our attention on the importance of adopting dynamically consistent source time function to improve strong ground motion prediction and to estimate seismically radiated energy for kinematic earthquake rupture models.

5.2 Ground motion forward modeling

The computation of ground motion that would result from a given earthquake, procedure known with the term 'forward modeling', is necessary to forecast shaking scenario for engineering design purposes and to study the effects of complex earth structure (*Spudich and Archuleta*, 1987). Predictions of ground motion strongly rely on the capability to build up realistic models of earthquake rupture (*Guatteri et al*., 2003). Theoretical studies of relationships between strong motion and earthquake source parameters were encouraged by the 1966 Parkfield, California, earthquake (*Aki*, 1968; *Haskell*, 1969; *Anderson*, 1974; *Boore and Zoback*, 1974; *Bouchon*, 1979; *Olsen and Archuleta*, 1996).

Even if sophisticated kinematic procedures have been developed for deterministic ground motion simulations (*Olson et al*., 1984; *Bernard and*

Madariaga, 1984; *Spudich and Archuleta*, 1987; *Hisada*, 2000, 2001; *Mai and Beroza*, 2002) the variability in the slip-velocity function is not considered and the resulting source complexity may not be physically plausible.
In this work, we aim to highlight the importance of the adopted source time function on the forward modeling of ground motions.

5.2.1 Computation strategy

The representation theorem provides us the instrument for computing synthetic seismograms; to solve the representation theorem integrals on a fault surface we use the Compsyn package (*Spudich and Xu*, 2003) based on the numerical techniques of Spudich and Archuleta (1987). The Compsyn applications allow us to obtain ground displacements through a compact form of the representation theorem given by Eq.(1.9). We perform the forward modeling taking the fault geometry and the station distribution of the 2000 western Tottori earthquake, Mw=6.6 (Figure2.1) and adopting different source time functions (Figure5.1): a boxcar, a modified cosine and two regularized Yoffe functions, characterized by two different values of T_{acc} (i.e. time of positive acceleration). A detailed description of the adopted source time functions is given in Section 1.6.

It is interesting to point out that for the same final slip, different STFs yield very different values of peak slip velocity and different spectra shapes (middle and bottom panel of Figure5.1, respectively). These source features could strongly affect the ground motion modeling since from the representation theorem it follows that the spectral properties of the source time function control the spectra of ground motion.

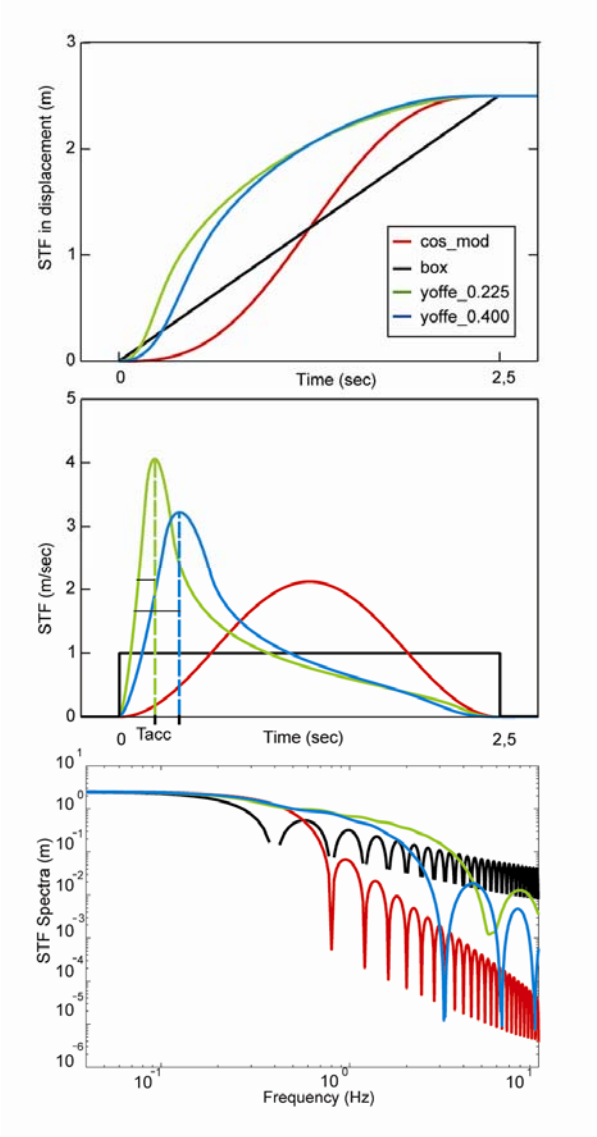

Figure5.1. Slip, slip velocity and amplitude spectra (upper, middle and lower panels, respectively) of the source time functions used in this study. Legend identifies the different source time functions.

To obtain a more realistic source characterization we consider a quite complex target rupture model. The fault has the following geometrical parameters: strike is 150°, dip is 90°, length and width are 40 km and 20 km, respectively; the top of the fault is 0.5 km below the free surface. Slip is concentrated only on two main asperities, A and B (see Figure5.2). Asperity A has a slip of 0.8 m and a rise time of 2.5 s; asperity B is narrower and extends deeper than A; it has a displacement of 1 m and a rise time of 2.5 s. The rupture front propagates at 2.5 km/s, except in the upper left part of the fault, where it is propagating at nearly 3.5 km/s.

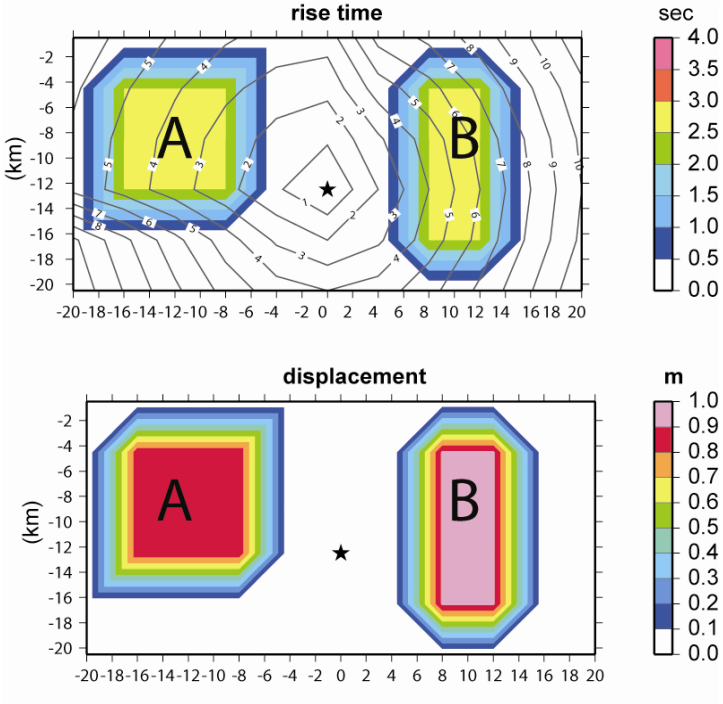

Figure5.2. Target rupture model used in strong ground motion forward modeling and for radiated seismic energy estimates. Horizontal axis is along-strike distance measured from the epicenter. Vertical axis is down-dip distance measured from the ground surface. Top panel shows the rise time; rupture time shown by contour lines (in seconds). Bottom panel shows slip displacement. The slip patches are denoted by capital letters A and B (see text for details).

Adopting the crustal model, listed in Table2.2, we model synthetic ground velocity and amplitude spectra in the frequency band 0÷1 Hz.

The frequency range limitation is based on the behavior of the earthquake source, which is relatively well modeled for frequencies up to 1÷2 Hz. Above this frequency the source is not deterministically well understood; this aspect is one of the major difficulty to obtain accurate prediction of ground motions above 1.0 Hz (*Spudich and Archuleta*, 1987).

5.2.2 Results: Waveforms and spectra comparison

We compare the velocity time series and the amplitude spectra in all the stations, computed by using source models characterized by different STFs.

The simulated ground motions depend on the choice of the source time function, especially at stations located near the source; differences decrease moving far away from the fault.

In Figure5.3 we show the comparison between ground-velocity seismograms (upper panel) and amplitude spectra (bottom panel) calculated at the nearest-fault location, SMNH01 station (d=8 km).

The near fault locations show much more sensitivity to adopted STF because the directivity effect, the rise time, and the time dependence of slip after rupture lead to ground motion that may be dominated by large pulse of short duration (*Heaton,* 1990; *Somerville et al*., 1997).

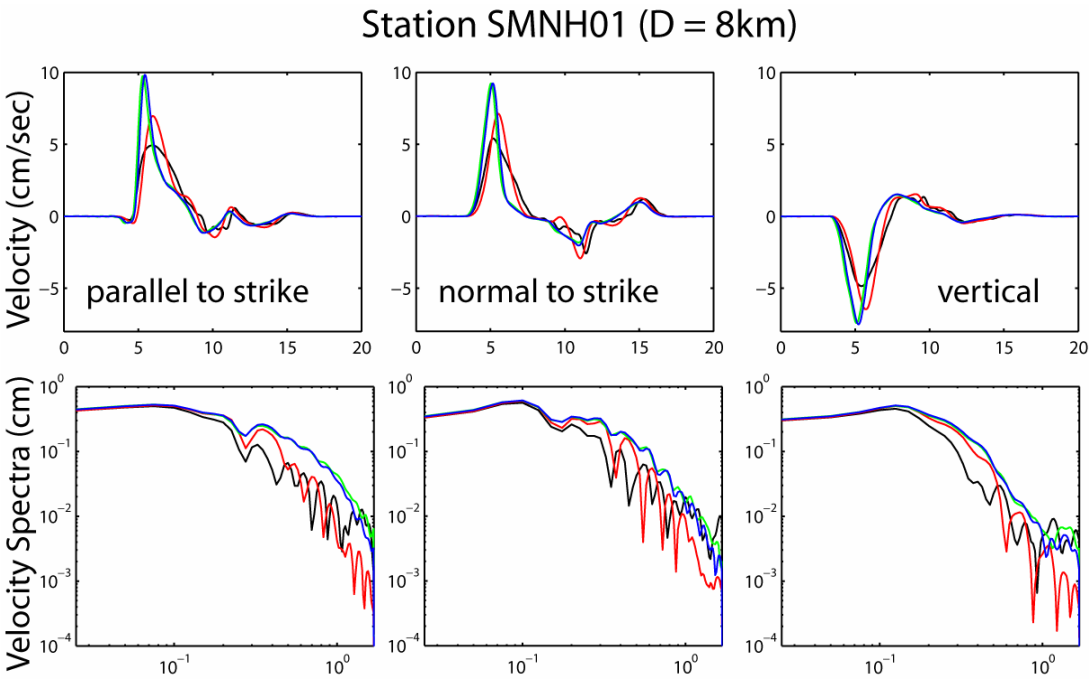

Figure5.3. Comparison between velocity seismograms and spectra amplitude calculated with different source time functions (see legend of Figure5.1), for the nearest strong motions stations, located at epicentral distance d=8 km (SMNH01).

This evidence is attributable to variations in the slip-velocity function arising from rupture dynamics effects and highlights the importance of understanding the slip velocity behavior for predicting strong ground motion in the near-fault region.

The amplitude spectra (bottom panels of Figure5.3) show that dynamically consistent STFs (i.e. the regularized Yoffe functions) have a greater high frequency content in the considered frequency range and therefore they are able to better constrain the details of the earthquake rupture in the near field.

These results suggest us to develop more physically constrained and consistent kinematic source model for deterministic near-fault ground motion simulations.

The assumption that a boxcar describes the time evolution of slip during earthquake rupture is inadequate to realistically characterize the fault behavior: there are two singularities (rupture time and healing phase) and a constant slip velocity; these features have been never obtained during spontaneous dynamic modeling. A cosine slip function (*Cotton and Campillo*, 1995) or a regularized Yoffe function (*Tinti et al*., 2005a) better describes the fault particle motion of a complex source. The latter source time function permits us to develop a time domain parameterization of a dynamically consistent STF that has great challenge for applications to near-field strong ground motion prediction.

These results suggest that the choice of STF may have an important role to estimate the energy radiated from the earthquake source.

5.3 Radiated seismic energy

In this section we evaluate the effects of source time function on the radiated seismic energy estimates.

The energy released during an earthquake is a fundamental physical parameter for earthquake sources, but the only part of the total energy that can be measured from seismological data is the seismic energy radiated in seismic waves. The radiated energy is considered the original seismological measure of earthquake size. It has been measured since more that 50 years ago (*Gutenberg and Richter*, 1942, 1956). In the literature, radiated energy has been estimated from either near-field with regional data or far-field with teleseismic data. Earlier studies used the empirically derived Gutenberg-Richter relation to estimate the radiated energy (*Wyss and Brune*, 1971). Radiated energy has also been estimated from source functions determined by inversion of seismograms (*Kikuchi and Fukao*, 1988) and empirical Green's function deconvolutions (*Venkataraman et al*., 2002).

The advent of digital broadband networks has allowed estimates of radiated energy by direct integration of velocity records (*Boatwright and Choy*, 1992; *Houston and Kanamori*, 1990; *Singh and Ordaz*, 1994; *Choy and Boatwright*, 1995; *Winslow and Ruff*, 1999; *Pèrez-Campos and Beroza*, 2001).

The underlying principle for the direct estimate of seismic energy from the data is that far-field *P*- and *S*-wave displacement is proportional to the moment rate time history (*Venkataraman and Kanamori*, 2004).

In general, the *P*-wave group (*P*, *pP* and *sP*) is used for the teleseismic estimate of seismic energy (*Choy and Boatwright*, 1995; *Pèrez-Campos and Beroza*, 2001). For the regional estimates the S-wave is used instead (*Kanamori et al*., 1993; *Singh and Ordaz*, 1994; *Boatwright et al*., 2002).

Even if the digital networks have improved radiated energy estimates, the uncertainty on these estimates still exists due to the complex effects of scattering, attenuation waves and source complexity (*Ma and Archuleta*, 2006).

5.3.1 Methodology

The radiated energy comes from the entire volume around the fault plane and it should be computed by integrating in time and in space the total energy flux over the focal sphere. The far field, S-waves radiated energy can be computed integrating the energy flux over the focal sphere at distances larger than the fault dimension, accounting for the slip velocity histories on the fault plane.

From Boatwright et al. (2005) it results that the radiated energy computed in the frequency domain over the entire focal sphere is given by the integral:

$$\mathrm{Es} = \rho\beta \frac{r^2}{\pi} \iint \int_0^\infty \left| \dot{u}'_s(x,\omega) \right|^2 d\omega \sin\vartheta d\vartheta d\varphi \tag{5.1}$$

Evaluated at a distance $r >> \Sigma^{1/2}$, where Σ is the rupture area and $x(r,\vartheta,\varphi)$ is the location. $\left| \dot{u}'_s(x,\omega) \right|^2$ are the Fourier transform of the S-wave velocity seismograms at the observers, r is the source-receiver distance, ρ is the density and β is the average S-wave velocity.The far field contribution to the seismograms (*Boschi and Dragoni*, 2000) is given by:

$$u_i(x,t) = \frac{\mu}{4\pi\rho c^3 r_0} R_i \Omega(x,t) \tag{5.2}$$

where ρ is the rigidity, R_i is the radiation pattern coefficient, appropriate for the component of ground motion analyzed, $\Omega(x,t)$ is the source term, r_0 is the distance to the receiver from the origin on the fault plane, c is the waves velocity ($c = \beta$). The u_i are the synthetic seismograms calculated in a whole space, therefore they contain both radiation pattern and directivity effects.
If we rearrange the order of integration in Eq.(5.1), we can identify the resulting integral:

$$\left\langle r\dot{u}'_s(\omega)\right\rangle^2 = \frac{1}{4\pi}\iint r^2\left|\dot{u}'_s(x,\omega)\right|^2 \sin\vartheta d\vartheta d\varphi \tag{5.3}$$

as the *mean-square* S-wave velocity source spectrum. Here the term "source spectrum" implies that the spectrum has been corrected for both geometrical spreading and anelastic attenuation. The *rms* source spectrum $\left\langle r\dot{u}'_s(\omega)\right\rangle$ provides us a potential tool to highlight the frequency contribution to the radiated energy (*Boatwright et al*., 2005). This quantity can be computed by generating synthetic seismograms $\dot{u}'_s(x,t)$ at a sufficiently dense set of points on the focal sphere, transforming them to $\left|\dot{u}'_s(x,\omega)\right|$ and evaluating the *rms* average.

In order to estimate radiated energy, we compute the far field seismograms for four different kinematic models obtained assuming the target model shown in Figure5.1 and adopting the four different source time function displayed in Figure5.2. Then we use the computed ground velocity seismograms to estimate the effect of different source time function on the radiated energy. The latter is computed integrating the energy flux, due only to the S-waves (see Eq.(5.1)), over the focal sphere by assuming a distance of r_0=100 km, longer than the fault dimension, and a sufficient dense discretization of the focal sphere (10000 points on the surface). The radiation pattern of S-waves is computed following the Eq.(15) of the Insert 4.6 given by Boschi and Dragoni (2000); while the source term $\Omega(x,t)$ is described by a simple integral:

$$\Omega(x,t) = \iint_{\Sigma}\Delta\dot{u}\left(\xi, t-\frac{r}{c}\right)d\Sigma \tag{5.4}$$

where $\Delta\dot{u}$ is the kinematic source function and c is the velocity of wave propagation. We simplify the computations considering only the strike slip velocity component of each kinematic model.

5.3.2 Results

In Figure5.4 we show both the contribution of mean-square S-wave velocity (*rms*) source spectrum (panel a) and the cumulative seismic energy flux (panel b) for the four kinematic models.

It is evident that the adopted source time function affects the frequency contribution of the radiated energy. The different STFs contribute differently to both the *rms* spectrum and the cumulative energy.

The curves split for frequencies higher than about 0.5 Hz. Besides, the kinematic model characterized by a boxcar slip velocity function (black line) underestimates the radiated energy at frequency above 2 Hz of nearly a factor 3 with respect to the radiated energy computed with the other source time functions.

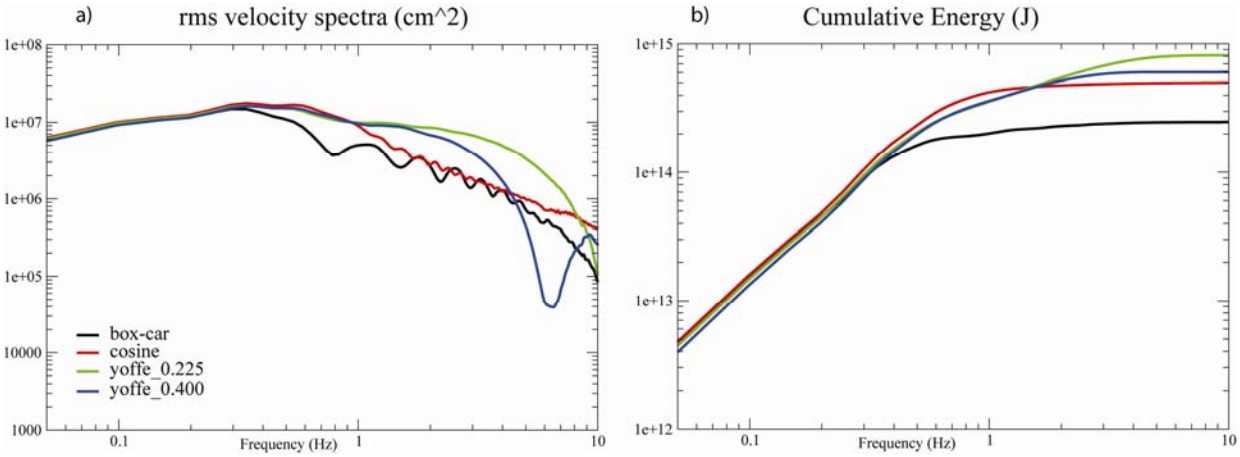

Figure5.4. a) Comparison between *rms* velocity spectra obtained with different source time functions; b) Comparison between cumulative radiated energy estimated with different source time functions.

The holes present in the curve associated to the boxcar function (panel a) are probably due to the holes inherent to the spectral properties of a boxcar function (see bottom panel of Figure5.1).This feature could strongly bias frequency (or period) dependent ground motion parameters, such as seismic radiated energy.

5.4 Discussion

Our results show that the choice of the source time function affects the ground motion modeling and the radiated seismic energy estimates. These latter are particularly sensitive to the spectral properties of the adopted source time function.

In most of the kinematic procedures developed for deterministic ground motion simulations, the source time function is chosen as an integral of a simple triangles or boxcars.

The radiated signal in a form of triangle or boxcar function is clearly not physical (*Beresnev*, 2003). The shape of these source time functions suffers the presence of several nodal holes.

In particular, the amplitude spectrum of a boxcar of width t_0 is a sinc function, whose first two nodes occur at $f=1/t_0$ and $f=2/t_0$. Hartzell and Langer (1993) utilized t_0 = 2 sec and included frequencies up to 1 Hz in their studies, which consequently cover both spectral nodes at 0.5 and 1 Hz. Das and Kostrov (1990) utilized boxcars with t_0 = 5 sec (first node at 0.2 Hz) and included frequencies up to 0.5 Hz, and Hartzell and Liu (1995) utilized boxcars with t_0 = 1 sec (first node at 1 Hz) and included frequencies up to 5 Hz. In the work by Bouchon et al. (2002), boxcar t_0's are permitted to vary between 0.25 and 5 sec, yielding frequencies of the first nodes between 0.2 and 4 Hz.

Several spectral nodes may occur in the modeled frequency range if the boxcar elemental functions are used. This deficit in spectral energy affects the results of a formal strong motion forward modeling, providing synthetic data with null spectra in certain frequency intervals (*Beresnev*, 2003).

These analyses emphasize the unphysical lack of energy near nodal frequencies for elemental functions, which do not show a behavior consistent with the dynamic characterization of an earthquake rupture.

The results of our contribution to this interesting debate recommend that one should be cautioned against any dogmatic interpretation of slip distributions that are obtained without a careful analysis, since that reliable images of slip on rupturing faults have large implications for seismic-hazard and shaking-scenario analysis.

Chapter 6

Variability of kinematic source parameters: Implications on shaking scenario

6.1 Introduction

With the intensive use of analysis techniques in the seismic design of structures, the prediction of ground motion time series has become indispensable for the complete determination of structural response and damage estimation from future large earthquakes. For that purpose many methods have been developed focusing on seismic risk evaluation.

Among them, the so-called seismic scenario consists of carrying out the evaluation of seismic risk based on simulations of ground motions produced by well-known active faults that constitute a potential seismic source. Although we don't know the exact time of the next damaging earthquake, geologists, seismologists and geodesists have recognized faults that are capable of producing large-magnitudes earthquakes in urban areas (*Liu et al*., 2006b).

In general, ground-motion estimates strongly depend on fault geometry, detailed rupture process, propagation's paths and local site effects. A recent review *(Douglas*, 2003) summarizes more than 120 studies that have derived equations for the estimation of peak ground acceleration (PGA) and 80 studies that derived equations for the estimation of response spectral ordinates. Therefore, there is still an open debate to identify a common strategy to face the ground motion prediction and to select shaking scenarios. Possible selection criteria are often hard to quantify, and there is no common thoughtful about the relative importance of individual criteria.

The estimation of the ground motion variability and the studies on its origin have gained importance with the evolution of modern seismic hazard analysis. Since Bender (1986), this variability has been a fundamental ingredient in the common approach of the probabilistic seismic hazard analysis (e.g. *Cornell*, 1968)

and its upper limit has been also an essential element in the hazard analysis for long return period (e.g. *Bommer et al*., 2003; *Andrews and Hanks*, 2007). The physical mechanisms producing the ground motion variability are complex and may be categorized following many criteria. A preliminary classification can be done in terms of *inter*-event and *intra*-event origins. The *intra*-event variability corresponds to the spatial variability, i.e. the variability observed at different sites during a single earthquake, meanwhile the *inter*-event variability includes the temporal variability, i.e. the variability of the ground motion considering several earthquakes.

A second criterion to classify the causes of the ground motion variability is based on the separation between the variability due to the heterogeneities of the propagation medium and to the kinematic parameters describing the seismic source. Nevertheless, the *intra*-event variability is not only due to the propagation medium heterogeneities but includes also source effects, like directivity or radiation pattern, which are not isotropic.

The relative weights between the effect of seismic source complexity and the heterogeneity of the propagation medium remains also an open question. At large distances from the seismic source, the high frequency motion is expected to be mainly controlled by the properties of the propagation medium. For instance, Spudich and Chiou (2008) show that the radiation pattern imprint in this frequency-distance domain tends to vanish. However, during the last earthquakes, occurred inside dense seismic networks (e.g. Chi Chi, 1999; Parkfield 2004), the large spatial variability of the ground motion, recorded in near source range, is due for the most part to the local variation of the fault geometry and the rupture process (e.g. *Ma et al*., 2000; *Shakal et al*., 2005).

The relative weights between the *intra*-event/*inter*-event and source/propagation causes for ground motion variability will be better understood in the future with the improvement of ground motion databases. However, for the time being, the use of synthetic approach may partially help to overcome the paucity of near-source data to study the variability on the strong ground motion (e.g. *Andrews et and Hanks*, 2007). The use of synthetic computation has few advantages; it allows us to separate the causes of the ground motion variability and to understand the

ratio between the influence of the source and the path. Moreover, it is a useful tool to appreciate the effects of each source parameter on the ground motion variability. Synthetic computation helps therefore to study the hierarchy among the source parameters in terms of their influence on the ground motion parameters.

The interest of a massive use of synthetic scenario computations is also connected to engineering seismology field; the large amount of synthetic data gives a very detailed description of the ground motion variability, also if it could represent a drawback for the engineers who needs to select only few temporal signals for dynamic analysis purpose.

However, it is possible to extract a subset of scenarios on the basis of quantitative and objective criteria and to easily combine them to take into account different stations or different fault segments, following a sort of vectorial approach (i.e. *Bazzurro and Cornell*, 1999). In this way, it is possible to select the synthetic scenarios matching the engineering requirements, providing also useful information on the effect of the source kinematic parameters.

The present chapter is focused on the analysis of the ground motion variability due to the kinematic source parameter variation, through the massive use of synthetic scenario computations. In particular, we limit the study to the variability generated by the variation of four different seismic source parameters.

This analysis allows in a second step to combine the information in more complex situations where are involved different stations and/or different ground motion parameters in order to select the most representative scenarios.

6.2 Shaking scenario and kinematic source parameters

The computation of ground motion of a designed earthquake is necessary to forecast a shaking scenario.

The shaking scenarios for engineering applications are generally provided in terms of ground motion parameters (e.g. peak ground acceleration, PGA, peak ground velocity, PGV, and peak ground displacement, PGD) expected at a given site. The required parameter is constrained by the vulnerability analysis that will be performed and by the region of interest, depending on different kind of structures (e.g.: tunnel, bridge, building, railways, etc.) and/or on different earthquake magnitudes.

Besides the sites effect and the velocity structure, the ground motion parameters are related to the characteristics of the kinematic rupture process occurring on the fault plane; the ground motion should be strongly affected by the variability of the source parameters describing this process, such as the source time function (STF), the position of nucleation point (*np*), the rupture velocity (v_r) and the slip distribution on the fault plane.

In this study we quantify the effect of this variability on two ground motion parameters (PGV and PGD).

6.2.1 Variability of kinematic parameters

The variability ranges of the kinematic parameters describing the rupturing fault (rupture velocity, slip distribution, nucleation point, source time function) are generally constrained by the scaling laws, or physically defined by studies on source dynamics. In the following we summarize the expected ranges and the reference values of the kinematic parameters we vary in this study.

Position of the nucleation point (*np*)

The location of the hypocenter on the fault plane is very important because it controls the directivity effect. In the literature, this parameter is not very well constrained; however, in a large number of events the hypocenter is found close to

the bottom of the fault, while very few events have the hypocenter located close to the fault top (*Manighetti et al.,* 2005; *Mai et al*., 2005). Moreover, repeating ruptures on the same fault can nucleate in different position along rupture length; for example, the two more recent similar Parkfield earthquakes, 1966 and 2004, indicate a complementary hypocenter location in the fault plane (*Custodio and Archuleta,* 2007).

Rupture velocity (v_r)

The velocity of the rupture front on the fault affects the signal duration and it contributes to the directivity effect, which increases as the rupture velocity increases. In the literature we find simplified descriptions of this parameter; it is often fixed constant on the fault plane. The assigned values are defined as a fraction of the shear-wave velocity (v_s), ranging between $0.6 \cdot v_s$ and $0.92 \cdot v_s$ (the latter corresponds to the Rayleigh waves velocity) as suggested by the dynamic simulations (*Andrews*, 1976; *Bouchon et al*., 2001; *Bizzarri et al*., 2001). Recent studies, using nonlinear kinematic inversion, infer kinematic models with variable rupture velocities on the fault. In the spontaneous dynamic models, the rupture velocity depends on the distribution of dynamic parameters on the fault plane; the heterogeneity of these parameters controls the variability of the rupture front. In particular, Ruiz (2007), through spontaneous dynamic simulations, obtains a rupture velocity proportional to the 4^{th} power of the slip gradient. The dynamic models predict also rupture velocities greater than the shear velocity under particular constitutive parameter assumptions (super-shear velocity, $v_r > v_s$; *Andrews,* 1976; *Rosakis et al*., 1999). In all these models, very high peaks of slip velocity are observed and they could be responsible of unphysical wave amplitudes. Nevertheless, models having supershear rupture velocity have been inferred for recent earthquakes (Izmit 1999, *Bouchon et al*., 2002; Denali 2002, *Oglesby et al*., 2004).

Slip distribution on the fault plane

The slip distribution imaged by kinematic inversion techniques, for several recent earthquakes, results heterogeneous on the fault plane. This heterogeneity can be observed at all the inherent scales. The self similar slip distribution (k^2) on the

fault plane, proposed by Herrero and Bernard (1994), results the simplest method to account for the details of slip in a large range of wavelengths.

Several authors have studied the influence on the ground motion of large slip patch and the relative position of these patches with respect to the hypocenter location (*Mai et al*. 2005; *Manighetti et al.* 2001).

Source time function

Each point on the fault plane starts to slip when the rupture front reaches its position. The final slip is attained in a time interval (i.e., rise time) and its evolution can be described through a slip velocity function varying on the fault.

Several authors have been proposed different models describing dynamic ruptures: crack-like models (*Das and Aki*, 1977; *Day*, 1982) and pulse-like models (*Heaton* 1990). In the crack-like models the healing is due to the rupture front back-propagating from the fault boundaries; in this case the rise time is comparable to the rupture duration and it depends on the dimension of the fault. In the pulse-like models the rupture front is followed by an healing front and the rise time is shorter and independent from the rupture duration.

The pulse models are generally used in kinematic simulations and the rise time is assumed either variable or constant on the fault. In these models the slip velocity is described by a functional form called source time function (STF), whose shape is usually described using a boxcar (see Eq.(1.11a)), or an exponential, or a cosine (see Eq.(1.11b)), or a triangle, or a regularized Yoffe (see Eq.(1.11c)) function.

6.3 Strategy to predict shaking scenarios

To compute the synthetic ground motion scenarios we propose the following strategy:

I) we use a fixed fault geometry and we vary some of the rupture parameters modeled by the chosen computational technique;

II) we synthesize the displacement and velocity seismograms at several sites around the fault;

III) we study the influence of kinematic parameters variability on ground motion;

IV) we collect the ensemble of synthetic shaking scenarios, which represent the expected ground motion for a possible design earthquake to be used for engineering application. In this perspective it is possible to select: (i) the synthetic records whose ground motion parameters match the engineering requirements, and/or (ii) a sub-set of scenarios which are related to the statistical values of the distribution (modal value, i.e. maximum probability of occurrence, extreme or mean values, percentiles, etc.).

In this section we focus on the variability generated by different kinematic parameters describing the seismic source (rupture velocity, slip distribution, nucleation point, source time function), and on the effect of this variability on the ground motion shaking scenario.

6.3.1 Computation method

It is well known that each ground motion parameter is controlled by different frequencies: the peak ground displacement (PGD) is related to the low frequency motion and it is mainly correlated to the magnitude and station-epicenter distance, the peak ground velocity (PGV) is controlled by the coherent low-to-intermediate frequency ground motion, whereas the peak ground acceleration (PGA) is related to the high frequency and attributed to small scale geological heterogeneities.

As a consequence, the choice of ground motion parameters drives the selection of a specific simulation method; different techniques reproduce the ground motions in different ranges of frequency. Moreover, among the simulation methods proposed in the literature, we have to select those that give us the possibility to vary the source parameters of interest. To achieve this task, we use a simulation procedure for extended fault; a discrete wave-number/finite element technique (Compsyn code; *Spudich and Xu*, 2003) which allows us to compute full-wave displacement and velocity time series in the low-to-intermediate frequency band.

6.3.2 Geometrical setting and fault parameters

We model all the shaking scenarios adopting a single fault plane with the focal mechanism similar to the 1980 Irpinia, Italy, earthquake (Mw 6.9): normal fault of (35x15) km^2 dimension, 60° dip, fault top depth at 2.2 km. Synthetic seismograms are computed in the frequency band (0÷2.5) Hz, considering 43 sites (12 stations of the Accelerometric Italian Network (RA) and 31 virtual sites) showed in Figure6.1. The fault distance of the selected sites varies between 7 km and 70 km.

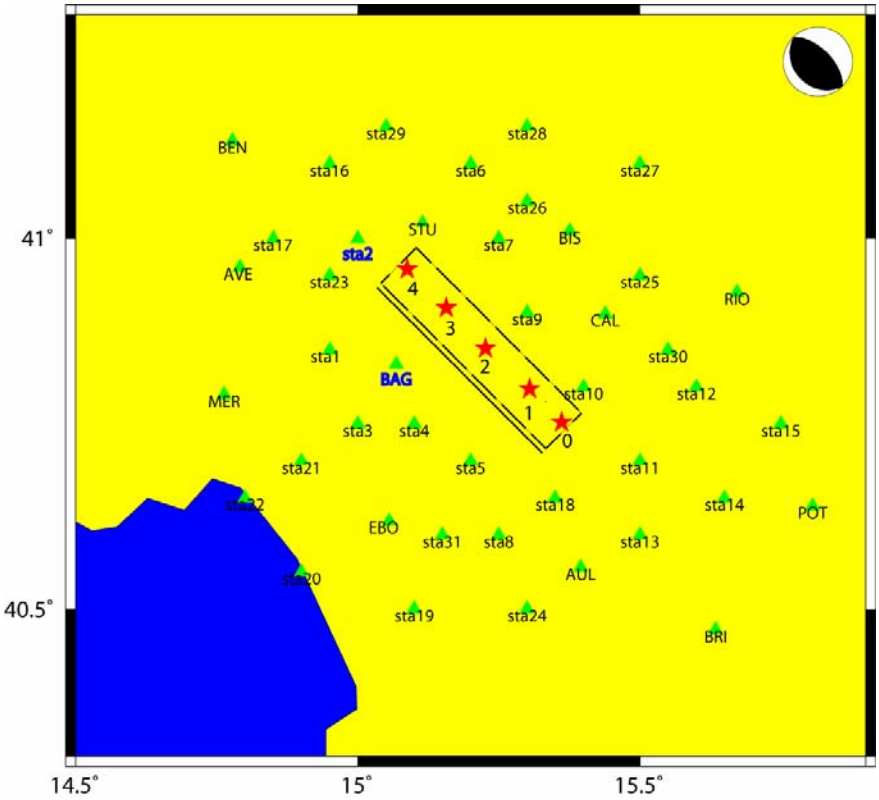

Figure6.1. Stations location (green triangles) and fault geometry similar to the 1980 Irpinia, Italy, earthquake source. Red stars indicate the position of nucleation points we consider in this study. They are located at 10 km down-dip from the upper edge of the fault.

We compute the Green's functions for a vertically varying 1-D crustal model and we exclude any site effect.

Table6.1 describes the 1D-layered propagation model (*Improta*, 2005, personal communication; *Amato and Selvaggi*, 1993) used in this study.

Table6.1. Velocity Structure.

h (km)	Vp (km/s)	Vs=Vp/1.81	Qs	rho (g/cm3)	comments
0	3.5	1.93	100	2.3	
2	4.5	2.49	100	2.5	
4	5.7	3.15	100	2.6	Apula platform
10	6.5	3.59	100	2.7	
25	7.5	4.14	100	2.9	
35	8.1	4.48	100	3.2	Moho

The different rupture models are obtained by varying four kinematic parameters: position of the nucleation point, rupture velocity, source time function and final slip distribution (Table6.2). Their values have been chosen in the range defined by several scaling laws inferred from the literature or through studies on source dynamics, as summarized in the previous section. We consider: i) five nucleation points (*np*) in the deeper half-width of the fault, equally spaced along its length to account of the potential directive and anti-directive effects (red stars in Figure6.1); ii) three distributions of final slip on the fault (model *A*, model *B*, model *C;* Figure6.2), each of them having asperities (i.e., patch of large slip) in different positions and computed using a k^2 model (*Herrero and Bernard*, 1994; *Gallovic and Brokešová*, 2007);

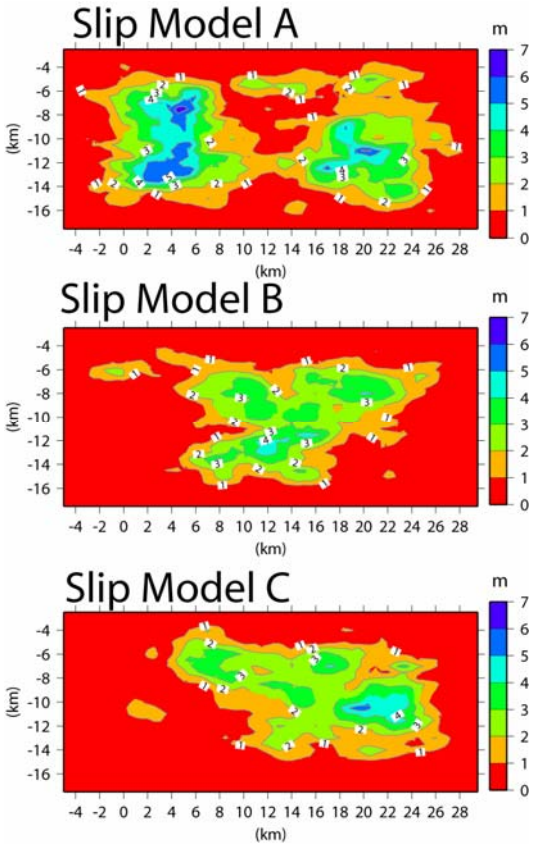

Figure6.2. Three distributions of final slip (model A, model B, model C) considered in this study

iii) four analytical source time functions (STFs) describing the slip velocity evolution: a boxcar (*BOX*), an exponential (*EXP*), a cosine (*COS*) and a smoothed Yoffe function (*Y0.225*), (Figure6.3);

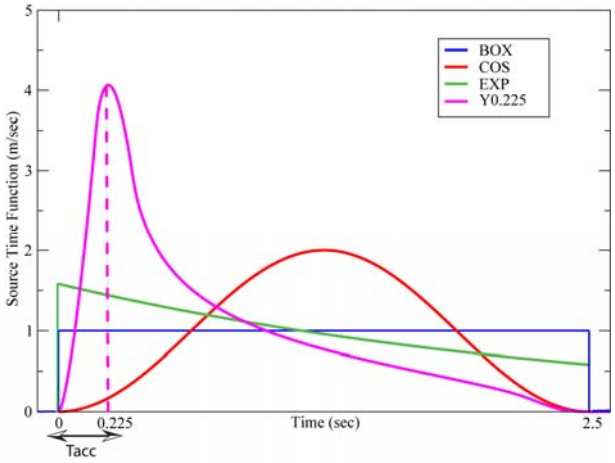

Figure6.3. Slip velocity source time functions adopted in this study

iv) three constant rupture velocities (v_r1, v_r2, v_r3), defined as 70%, 80% and 90% of S-wave velocity (v_s= 3.0km/s), and two heterogeneous distributions of rupture velocity on the fault, whose variations depend either on the distance (d) of the rupture front from the nucleation point (v_r4):

$$v_r(d) = d \cdot 0.035 + 0.6 \cdot v_s \qquad (v_r(d) \le 0.92\, v_s); \tag{6.1}$$

or on the final slip distribution *D(x,y)* on the fault plane (v_r5):

$$v_r(x,y) = (0.32 \times (D(x,y)/Dmax)^2 + 0.6) \cdot v_s; \tag{6.2}$$

where Dmax is the maximum slip reached on the fault (Figure6.4).

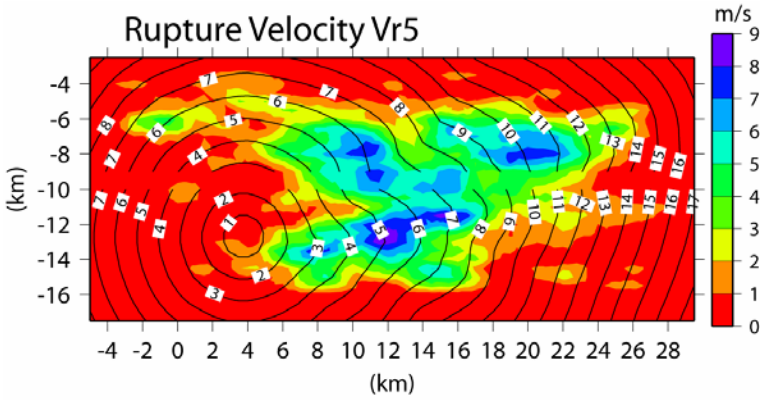

Figure6.4. Example of the rupture front (black traces) generated by a rupture velocity model whose variations depend on the slip distribution on the fault plane (rupture velocity v_r5)

The choice of the rupture velocity described in Eq.(6.1) derives from dynamic spontaneous modeling: at larger distances from the nucleation, the loading of the breaking points becomes higher and accelerates the rupture front. The constant parameters in Eq.(6.1) are chosen in order to fix a minimum velocity value at zero distance and to have a slow growing of rupture velocity.

Eq. (6.2) has been defined by modifying the formulation of Ruiz (2007) using a 2^{nd} order dependence of v_r on the total slip, in order to maintain a smooth rupture front propagation.

Table6.2.Variability of kinematic source parameters

Slip distribution	A	B	C		
Source time function	Boxcar	Exponential	Cosine	Yoffe (T_{acc}=0.225s)	
Nucleation point (km along strike)	0.0	8.9	17.8	26.7	35.0
Rupture velocity (km/s)	v_r1=2.1	v_r2 = 2.4	v_r3=2.7	$v_r4 = v_r(d)$ Eq.(6.1)	$v_r5=v_r(D(x,y))$ Eq.(6.2)

6.3.3 Shaking scenarios

For each site, the variability of the kinematic rupture parameters leads to 300 simulated shaking scenarios. Computations are performed at bedrock level, thereby site effects, non-linear effects and attenuation are not taken into account. From the synthetic time series at each site we obtain two ground motion parameters: the peak ground displacement (PGD) and the peak ground velocity (PGV).

Peak ground motions and empirical predictive model

We focus our attention on the distribution of the peak ground displacement and peak ground velocity at each site.

The peak ground velocity value associated to each site corresponds to the average of the PGV values of the two horizontal components.

Although the vertical component of ground shaking is important, the highest priority is given to the horizontal ground shaking because of its greater potential for causing damage (*Ambraseys et al.,* 1996*; Ambraseys and Simpson,* 1996).

As an example, we show in Figure6.5 the PGV (panel a) and the PGD (panel b) histograms computed for all the shaking scenarios at five sites (BAG (Bagnoli site), POTE (Potenza site), st02, st09, st22; see map in Figure6.5); the different sites have been selected to sample spatial regions of possible different behavior.

In general, the shape of the ground motion parameter histograms depends on the type of ground parameter itself and on the site position.

Empirical predictive relationships, developed after statistical analysis of data recorded during strong earthquakes, offer a useful tool for forecasting the ground motion of future earthquakes. Several predictive equations are by now available in different regions of the world (*Douglas*, 2003). In particular, Sabetta and Pugliese (1996) have developed an empirical model based on the Italian strong-motion database (190 horizontal components and 95 vertical components of strong motions recorded from 17 Italian earthquakes of magnitudes ranging from 4.6 to 6.8), as a function of magnitude, distance, and site geology.

In order to check the reliability of the obtained results, we compare the shape of the PGV histograms (Figure6.5a) with the log-normal distributions expected from the empirical model proposed by Sabetta and Pugliese (1996), labeled as *SP1996* in the plots of Figure6.5.

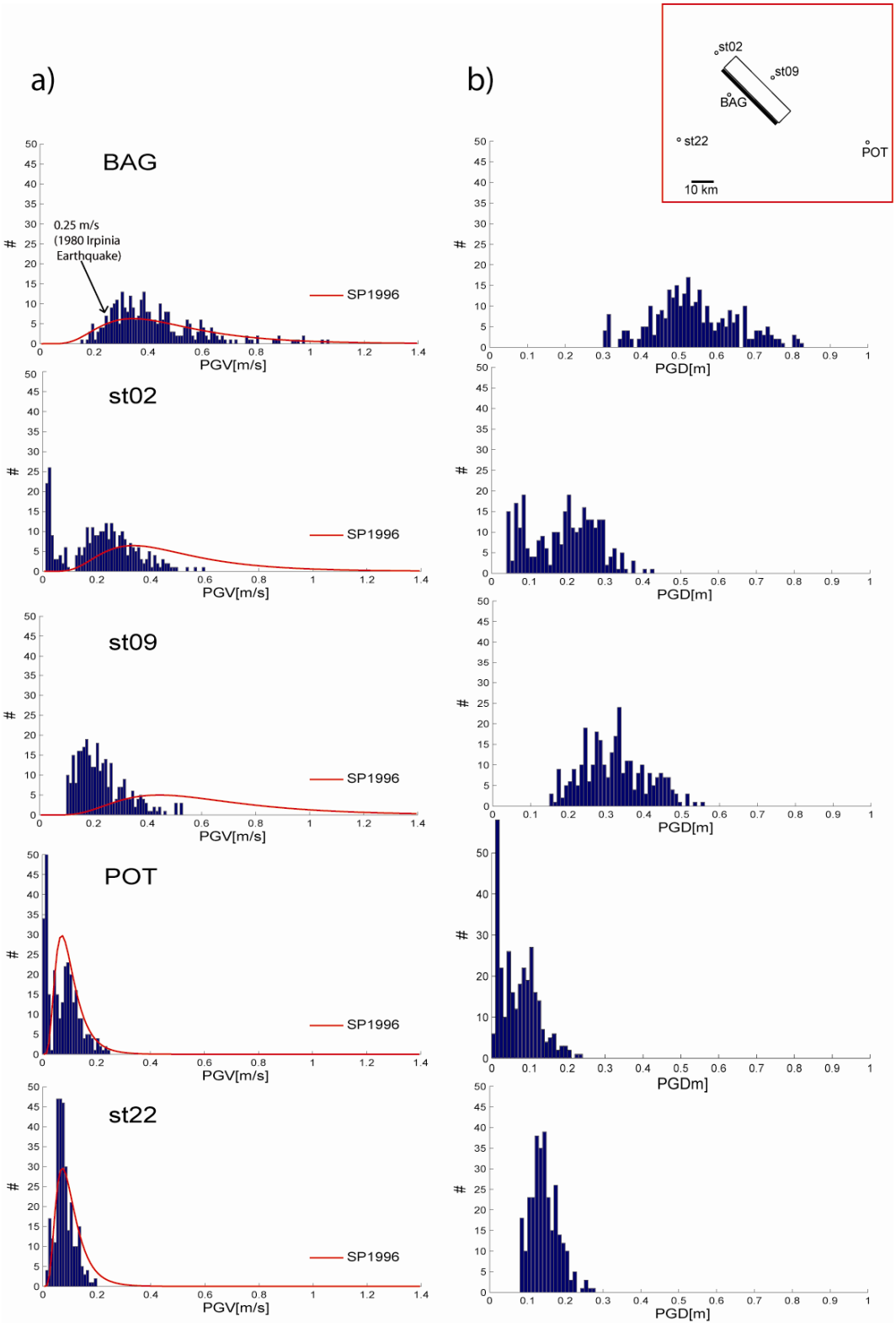

Figure6.5 a) PGV and b) PGD histograms computed for all the shaking scenarios at 5 sites. The empirical models are normalized to the total area of the histograms. Red traces represents the empirical model of Sabetta and Pugliese (1996).

Many interesting observations can be made on the comparison with the empirical model of Sabetta and Pugliese (1996).

First, the agreement of calculated peak ground velocity with the attenuation relation of *SP1996* model provides us an estimate about the performance and the reliability of the ground-motion simulation strategy we use.

Second, the shape of the obtained histograms is comparable with a log-normal distribution. In some stations, such as st02 and POTE, we observe the presence of very low peak values. This feature is probably due to the back-directivity of the ground motion distribution with respect to the site position.

The differences of the obtained PGV histograms with respect to the empirical model are consistent with the initial assumptions, since we don't take into account geological and site effects and we adopt a simplified 1-D propagation medium.

Finally, it is interesting to note that during the 1980 Irpinia earthquake the Bagnoli site experienced a PGV of 0.25 m/s. It is evident how this recorded value is only one of the range of possible values (0.17÷1.07 m/s) inferred at Bagnoli station from our simulations (Figure6.5).

Since we have verified that the computed peak ground velocity distributions are mostly log-normal; we can evaluate their geometric mean as a function of fault distance. In Figure6.6 we compare the geometric mean of the inferred peak ground velocity, PGV_{GM} , computed as the average of the two horizontal components, at all sites (black traces, the bars represent the corresponding standard deviations) ordered with fault distance. The data are compared with the empirical model (*SP1996*; showed with red traces; dotted lines represent the corresponding standard deviations).

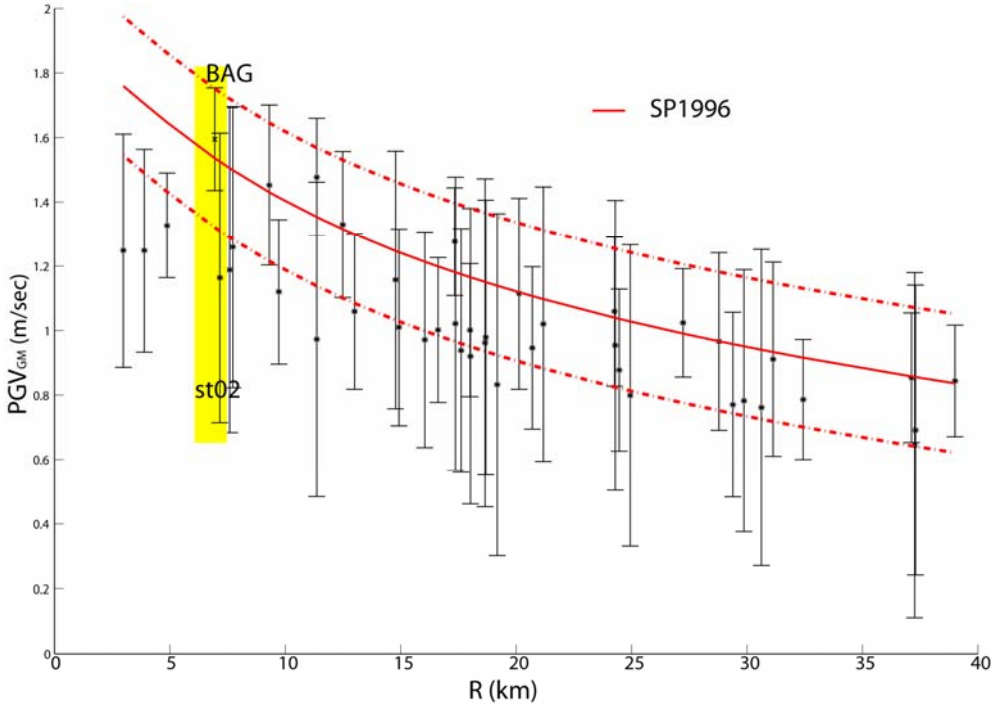

Figure6.6 Geometric mean and standard deviation of simulated PGV from scenarios computed at more sites, ordered by fault distance. Red traces show the comparison with the predictive equation of Sabetta and Pugliese (1996). Yellow box identifies the peak variability for sites having the same distance from the fault (e.g. BAG and st02).

In general, the range of peak variability is strongly dependent on the site location: closer are the stations to the fault, larger is the range of peak ground motion variability, described by the standard deviation. Besides, different ranges of peak variability occur even for sites having the same distance from the fault. (e.g. BAG and st02, enucleated with yellow box in Figure6.6).The comparison with the empirical model of Sabetta and Pugliese (1996) shows that the mean values of simulated scenarios tend to underestimate the predicted values. However, the standard deviations are consistent with the empirical upper bounds, and show a greater variability for the lower PGV values.

Sensitivity of peak ground motions to kinematic source parameters

We can highlight the influence of each kinematic parameter on the ground motion estimates looking at the details of the inferred PGV histograms.

Figure6.7 shows how the different choices of rupture velocity (panel a), of nucleation point (panel b), source time function (panel c) and slip model (panel d) affect the PGV expected at the same site (BAG: Bagnoli station).

The color histograms separate the contribution of a specific kinematic parameter to the PGV distribution (see the first line of each panels).

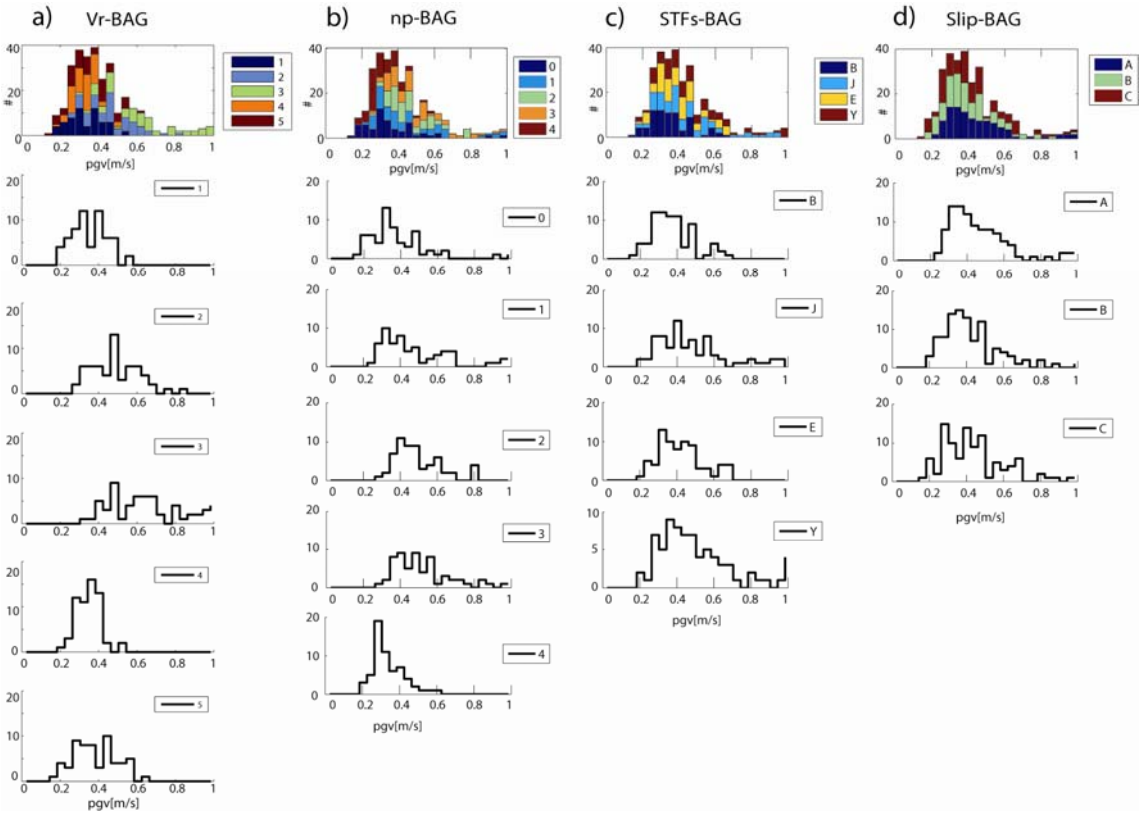

Figure6.7 PGV distribution at Bagnoli station (BAG). Color histograms (top panels) represent the cumulative distribution of scenarios due to the contribution of a specific kinematic parameter a) rupture velocity; b) position of nucleation point; c) source time function; d) slip model. Black histograms (single line) represent the PGV versus different values of each source parameter.

The histogram is the same for all vertical panels and it includes all the shaking scenarios; however the colors are different because they indicate the contribution of the different kinematic parameter values to its shape (see legends in Figure6.7). The single contribution of each source parameter value on the PGV distribution, at Bagnoli station, is shown in lower panels.

Panel a) of Figure6.7 shows the effect of the five different rupture velocities on the peak ground velocity motion. In this case, the rupture velocity has a strong effect on the PGV and it is evident how the rupture velocity v_r3 (green color) contributes to the highest PGV values. Increasing the rupture velocity also increases the PGV, whereas a reduction in rupture velocity causes reduced PGVs (see rupture velocity v_r1, blue color).

The effect of changing the location of rupture initiation is evident from panel b) of Figure6.7. The nucleation points *n0* and *n4* , located at the easternmost and westernmost point on the fault plane (red stars in Figure6.1), contribute to the lowest PGV values; while for nucleation points *n1, n2, n3* we see an increase of PGV. These results highlight how the effect of directivity on the PGV estimates is very clear and significant and confirm the strong effect of the location of rupture initiation on the ground motion directivity.

It is interesting to note how the different source time functions (panel c) affect the peak ground velocity distribution. In particular, the regularized Yoffe function yields the highest values of peak ground velocity motion. This feature is due to the spectral (see Figure5.1) and dynamic properties of this source time function. As we have seen in the previous chapter, the Yoffe function, has a larger high frequency content with respect to the other source time functions and therefore it contributes to the maximum values of the simulated PGV motion. These results confirm the importance of understanding the slip velocity source behavior in the near-fault region.

The variability of the three considered slip models (panel d) in Figure6.7, does not have an important impact on the PGV values.

We have to underline that all these effects are referred only to the selected site and are generally different on the other sites.

6.4 Scenario selection

The statistical distributions of ground motion parameters can help for the selection of a shaking scenario whose characteristics follow defined criteria. A typical example is the choice of a scenario whose values fit a defined peak value or spectral ordinates, such as expected from empirical models (*Sabetta and Pugliese*, 1996; *Ambraseys et al*., 2005), or from probabilistic hazard analysis (*Scherbaum et al*., 2004).

The selection of a specific scenario or of a sub-set of scenarios can be carry out directly from the distribution of ground motion parameters, i.e. by selecting the

scenarios which produce the modal value (maximum probability of occurrence), or the extreme or mean values, or the percentiles, etc.

In general, we can extract different information on the basis of different conditions; we can look for “one ground motion parameter at one site”; “more ground motion parameters at one site” and for “one ground motion parameter at more sites”.

6.4.1 One ground motion parameter at one site

In general, there are more than one scenario giving similar values of peak ground velocity (or peak ground displacement) at one site. In this case, we can define a subset of scenarios, characterized by different combinations of kinematic rupture parameters.

Figure6.8a shows the PGV distribution at Bagnoli station. Red shades highlight two different groups of shaking scenarios: group I represents the ensemble of scenarios whose PGV values range around ± 10 % of the maximum PGV value, and group II collects the ensemble of scenarios ranging around ± 5 % of the maximum probability of occurrence. Group I and group II are 1% and 29% of the total distribution, respectively.

For each group we can separate the contribution due to the different kinematic parameters (rupture velocity, slip model, nucleation point and source time function; labeled as 1, 2, 3, 4, respectively, in the plots of Figure6.9b and Figure6.9c). Scenarios with the maximum PGV values (Group I in Figure6.9b) are characterized by the largest rupture velocity (v_r3), slip model *A*, nucleation point in the directive position (*np1*) and the regularized Yoffe function. Scenarios providing the maximum probability of occurrence (Group II in Figure6.9c) depend on the lowest rupture velocities (v_r1 and v_r4) and on several positions of the nucleation point, slip models and source time functions.

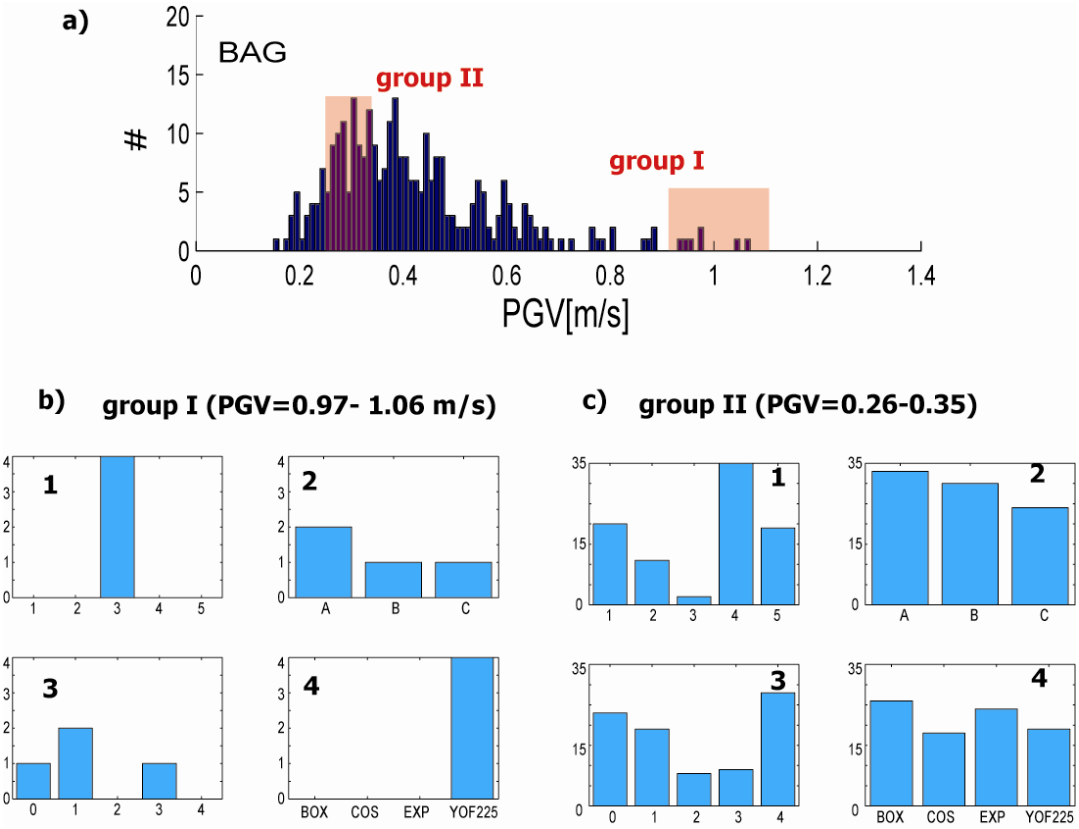

Figure6.8 a) One ground motion parameter (PGV) at one site (BAG). Red shades shows two different group of scenarios: group I (scenarios ranging around ± 10 % of the maximum PGV value) and group II (scenarios ranging around ± 5 % of the maximum probability of occurrence). b) selection of kinematic parameters contributing to the shaking scenarios of group I. c) selection of kinematic parameters contributing to the shaking scenarios of group II. Labels 1, 2, 3, 4 represent the contribution of different values/models of the rupture velocity, the total slip, the nucleation point and the source time function, respectively.

6.4.2 More ground motion parameters at one site

Instead of the correspondence with a single value at one site, the scenario selection can require to satisfy the combination of several conditions. However, it is not always possible to select a scenario satisfying more than one request.

Figure6.9 shows the combination of two kinematic parameters (slip distribution and rupture velocity; bottom panels of Figure6.9) producing the maximum values (red shades in upper panels) of peak ground velocity (PGV) and peak ground displacement (PGD) at one site (BAG: Bagnoli station).

In both cases the scenarios contributing to the maximum values are characterized by the maximum rupture velocity (v_r3) and by several slip distributions (*A*, *B*, *C*); however, none of them have the same source time function. This means that there

is not a common set of rupture parameters producing both maximum PGV and PGD at the same time; the selected scenarios are characterized by common rupture velocity, several slip distributions but different source time functions.

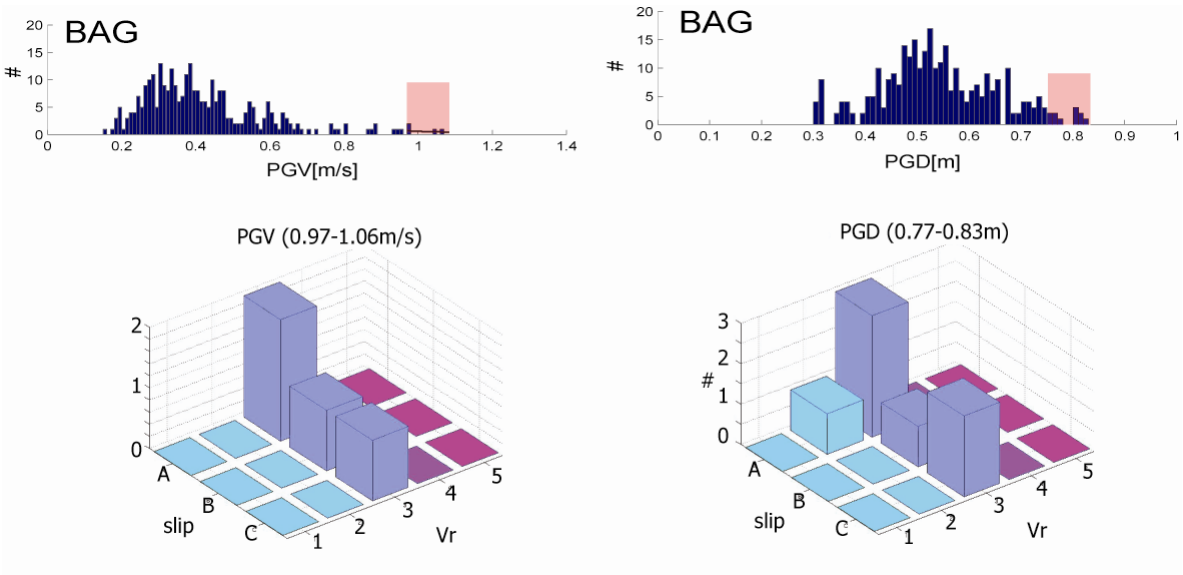

Figure6.9 More ground motion parameters (PGV and PGD) at one site (BAG). Bottom panels shows the combination of two kinematic parameters (slip distribution and rupture velocity model) producing the maximum values (red shades in upper panels) of PGV and PGD at Bagnoli station.

6.4.3 One ground motion parameter at more sites

In the case of earthquake scenarios for extended areas (such as an urban district), the selection of a scenario whose peak values are the same at more then one site (*multiple sites selection*) is not straightforward. This is generally true for sites in near source, as the two sites BAG and st02 which have the same fault distance (R = 6.9 ÷ 7.16 km) but different azimuth (Figure6.1).

In this case, the scenarios producing the expected PGV values (PGV=0.31÷0.38 m/s from *Sabetta and Pugliese*, 1996) at both sites, are 21% of the total for BAG and 12% for st02 (Figure6.10a, red shades). The empirical models are normalized to the total area of the histograms.

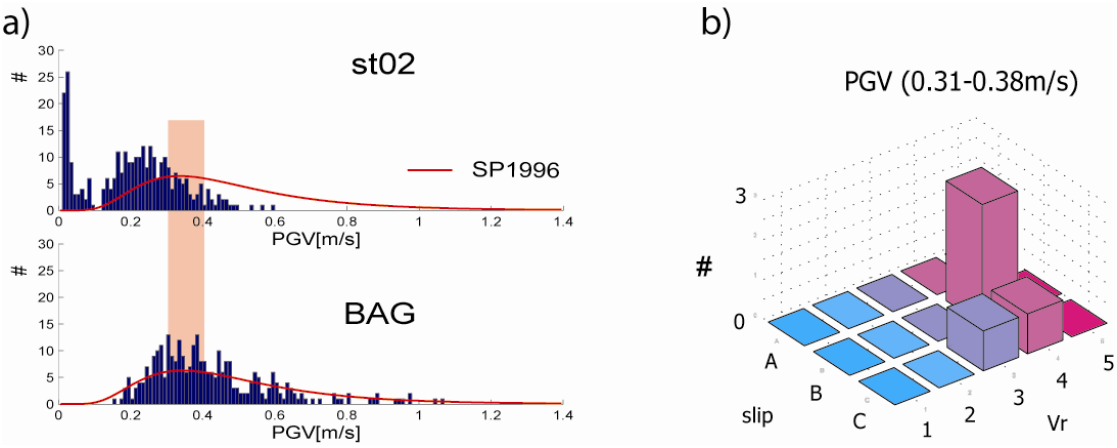

Figure6.10 One ground motion parameter (PGV) at two sites (st02 and BAG), which have the same fault distance (6.9÷7.16 km) but different azimuth (Figure6.1). a) PGV distribution at st02 and BAG. Red traces represent the predictive model of Sabetta and Pugliese (1996), normalized to the total area of the histograms. Red shades select the sub-set of scenarios producing the PGV values expected by the empirical predictive model valid for the area (PGV=0.31÷0.38 m/s from *Sabetta and Pugliese*, 1996) at both sites. b) Contribution of two kinematic parameter (rupture velocity and slip distribution) on the selected scenarios.

Looking for the contribution of kinematic parameters on the selected scenarios, we find that a fraction of them have the same slip distribution and rupture velocity (Figure6.10b), but only 2% of the total have also the same nucleation point and source time function. The combination of kinematic parameters describing the common scenarios are listed in Table6.3.

Table6.3 Combination of kinematic parameters describing the common scenario

Scenario	Source time function	Nucleation point	Slip distribution	Rupture velocity
1	BOX	0	C	3
2	COS	0	B	4
3	COS	1	C	4
4	EXP	0	B	4
5	YOF0.225	0	B	4

This means that only five scenarios, among the selected scenarios, have a common set of rupture parameters producing the PGV value predicted by Sabetta and Pugliese empirical model (*Sabetta and Pugliese*, 1996).

6.5 Discussion

The near-fault seismic motion recorded during recent earthquakes (Chi Chi earthquake, 1999; Parkfield 2004) shows a high spatial variability. This variability is controlled by the fault geometry, the rupture process complexity and also by the propagation and site effects. As a result of these observations, the earthquake scenarios can be largely influenced by the vicinity of the seismic source, and the number of available recordings is still not enough to infer a robust parameterization of the ground motion to be used for retrieving multi-parametric predictive equations. Recently, several studies have been focused on the understanding of the relationships between the kinematic source parameters and the choice of the design scenario (*Irikura et al*., 2004). This important issue is strongly affected by the uncertainties related to defining the source parameters of a scenario earthquake. Furthermore, uncertainties on source parameters influence the results in a way which until now has not been well resolved (*Søresen et al*., 2007).

The work we have presented in this chapter aims to contribute to this open debate, with the main objective to study and to quantify the effect of the kinematic source variability on the ground motion parameters.

We have modeled scenarios from different rupture models of a fault mechanism similar to the 1980 Irpinia, Italy, earthquake source (Mw 6.9), using a discrete wave-number/finite element technique to compute the full-wave displacement and velocity time series in low-to-intermediate frequency band. We have investigated the *inter* and *intra* event variability as a function of different source rupture parameters (rupture velocity, slip distribution, nucleation point, source time function), whose values depend on the degree of knowledge of the physical mechanisms controlling the process. The different shaking scenarios have been defined by varying these critical source parameters, in order to observe their influence on the simulated ground motion parameters (peak ground velocity, PGV, and peak ground displacement, PGD).

Kinematic source parameters have a significant effect on the resulting ground motions, both in terms of distribution and absolute level of the ground motions. The rupture velocity has an important effect on the PGV values and the largest

variations are due to the highest value of rupture velocity. The location of the rupture initiation (nucleation point) is critical because of the effects of directivity. Moreover, the source time function strongly affects the simulated ground motion. In particular, the adoption of dynamically consistent source time functions, such as the regularized Yoffe function, has important effects on the maximum values reached by the ground motion parameters.

This approach allows us to recognize the contribution of each kinematic source parameters and to analyze the effects of their variability on the ground motion scenarios. The reliability of our strategy has been checked through the comparison of the distribution of the computed peak ground velocity motions with the empirical model of Sabetta and Pugliese (1996). In a second step we have used the histograms of the simulated ground motion parameters, (PGD and PGV), to select one or more representative scenarios matching specific criteria. The results of this analysis reveal that even if we have reliable ground-motion estimation procedures we are still limited in the prediction of ground motions by our limited knowledge of the source. The source uncertainty is important and should always be kept in mind when interpreting ground motion simulation results.

The present study provides a contribute to improve our understanding on the seismic source and on its effects on the ground motion predictions. Much efforts should be focused on improving our ability to accurately estimate the most critical source parameters influencing the ground motion; a robust model of the complex source process is essential to correctly estimate ground shaking scenarios for seismic-hazard assessment and risk analyses.

This work started during the Italian Project S3 "Shaking seismic scenarios in area of strategic and/or priority interest" (http://esse3.mi.ingv.it/index.htm), funded by the Italian Dipartimento della Protezione Civile in cooperation with Istituto Nazionale di Geofisica e Vulcanologia - INGV. Last development has been carried out under the financial auspices of the Italian Ministry for Research and Higher Education (MiUR - Ministero dell'Università e della Ricerca) through the FIRB Project No RBIN047WCL (Assessment and Reduction of Seismic Risk to Large Infrastructural Systems).

Conclusions

Kinematic description of the rupture process forms the basis of our inferences about the seismic phenomena, and provides a stepping stone for our understanding of earthquake physics (*Haskell*, 1969). The kinematic rupture models for moderate to large earthquakes are currently obtained by inverting seismic and geodetic data, and represent the starting point for several seismological applications. Two main goals of kinematic source modeling are to improve the knowledge of the physical processes governing dynamic rupture propagation and to predict ground motions for seismic hazard assessment. To achieve these important aims, the reliability and accuracy of the retrieved kinematic rupture models are crucial issues and are the fundamental tasks of the current scientific research.

We present a two-stage nonlinear technique to jointly invert strong motion records and geodetic data to image the complete earthquake kinematic rupture history on a finite fault. To account for the actual rupture complexity, the fault parameters are spatially variable peak slip velocity, total slip, slip direction, rupture time and rise time. The unknown parameters are given at the nodes of the subfaults, whereas the parameters within a subfault are allowed to vary through a bilinear interpolation of the nodal values. The forward modeling is performed with a discrete wave-number technique whose Green's functions include the complete response of the vertically varying Earth structure. During the first stage, an algorithm based on the heat-bath simulated annealing generates an ensemble of models that efficiently sample the good data-fitting regions of parameter space. In the second stage (appraisal), the algorithm performs a statistical analysis of the model ensemble and computes a weighted mean model and its standard deviation. The algorithm is conceived to perform several multiple restarts with different random trial models, in order to make the model ensemble independent from a particular choice of the initial model. This technique allows the use of a very large model ensemble, and rather than simply looking at the best model, extracts the

most stable features of the earthquake rupture that are consistent with the data, giving an estimate of the variability of each model parameter. Our technique belongs to the single-time window approaches, where the temporal evolution of slip on the fault plane is obtained assuming an analytical expression for the source time function. In the present implementation, different forms of the slip velocity source time function (STF) can be chosen, providing us a tool to investigate the effect of the adopted STF on the retrieved kinematic rupture models.

In order to discuss the applicability and the main features of the proposed method, we present several synthetic tests, based on the geometry of the 2000 western Tottori, Japan earthquake. Uncertainties exist in kinematic source models deduced from inversions but these are difficult to quantify since they may have several origins. In particular, we check the effectiveness and robustness of our procedure with respect to two main sources of uncertainty in finite-fault inversion: the poor knowledge of both the crustal model and the slip velocity source time function. The sensitivity analyses show that the resolution of the retrieved rupture models could be strongly biased by an inaccurate crustal model, as well as by an inappropriate choice of the source time function.

The effect of the velocity structure is significant for the strong motion waveforms, while the variations in static displacements are small. Except for the near-surface slip, which is strongly affected by the velocity structure, the recovery of the overall slip distribution is relatively robust. The comparison between the noise-free data test and the uncertainty of velocity structure test emphasizes the importance of a suitable velocity structure for source inversion studies.

The representation of the adopted source time function affects the retrieved kinematic parameter distributions. The analysis of the *trade-off* between model parameters and the *bias* due to an erroneous choice of the STF, allows us to quantitatively assess how an inaccurate knowledge of the source time function affects the imaged kinematic rupture histories. The obtained results show that the effects of uncertainty factors on source resolution are crucial to assess the reliability of an inversion procedure and must be taken into account and carefully analyzed. The appraisal stage in nonlinear inversion is as important as the search

for the best model, and it should be further developed and it should become a common practice in finite-fault nonlinear inversion studies.

In order to stress the reliability of our nonlinear inversion technique, we perform a joint inversion of strong motion and GPS coseismic data to retrieve the rupture history of two Japan earthquakes. We study the 2000 western Tottori (M_w 6.6) and the 2007 Niigata (M_w 6.6) earthquakes. Both quakes occurred within the recently developed nationwide seismic networks (K-net and KiK-net), providing us a unique opportunity to investigate the source process in detail. These recent events show different interesting aspects which have drawn a growing attention of the scientific community.

For the 2000 western Tottori earthquake, we do not have any clear manifestation of surface break, thus it is almost impossible to derive fault geometry from geological observations. However the source model we retrieve, definitely shows that large shallow slip can occur without any surface break. Such shallow rupture with no surface break has been observed previously (e.g., Morgan Hill, in 1984; northern part of the Kobe earthquake, in 1995). According to Semmane et al. (2005), large strike slip earthquakes may have occurred in the past without cutting the surface. This phenomenon could complicate the interpretation of paleoseismological data. Return periods of damaging earthquakes could be overestimated if such shallow earthquakes with no surface rupture (blind fault) occurred. Moreover, according to Kagawa et al. (1999), ground motions generated by buried fault are larger than ground motions generated by earthquakes that rupture the surface. It is therefore essential to better constrain the source properties to perform ground motion simulations for earthquake scenarios.

The 2007 Niigata-ken Chuetsu-oki earthquake is the first large event whose source fault extends beneath a nuclear power plant (Kashiwazaki-Kariwa nuclear power plant), and for which peak ground acceleration (PGA) value of more then 1200 gals (surface motions) have been recorded. An interesting characteristic of the retrieved rupture history concerns the inferred rupture velocity distribution, which shows an acceleration of the rupture front in the south-west and shallower part of the fault, in correspondence of the largest slip patch. This feature could partially explain the large-amplitude signals observed in the Kashiwazaki-Kariwa

nuclear power plant. The study of seismic sources in this area becomes an issue of public attention and it results very important for seismic hazard analysis.

Earthquake kinematic models are often used as input data to infer the key parameters of the dynamic source process. The measure of these quantities can be biased by the adopted parameterization of kinematic source models. Often, such rupture inversion is only based on plausible considerations, without taking into account the reliability and the dynamic consistency of the rupture processes. In particular, the dynamic inferences may be strongly biased by unphysical constraints on the source time function adopted for kinematic source modeling (*Piatanesi et al.*, 2004).

Here we propose that, in order to make this task achievable, suitable inversion schemes and appropriate choices of the kinematic parameters must be adopted.

We perform several sensitivity tests to analyze the effect of parametric uncertainty on the retrieved rupture histories. We see that the choice of the source time function is fundamental to constrain the inferred kinematic parameters. In particular we find that source time functions compatible with earthquake dynamics strongly reduce the bias due to the parametric uncertainty, and we provide a parameterization to stably retrieve the rupture history on a finite fault.

These results stimulate us to evaluate the relevance of adopting dynamically consistent source time function to image the rupture history of real earthquakes. Different analytical forms of source time function are therefore assumed to retrieve the rupture process of the 2000 western Tottori earthquake. Comparing the inferred source models, we see that the choice of the source time function affects the kinematic parameter distributions, especially in terms of peak slip velocity and rise time.

We quantitatively verify that these differences are crucial when kinematic models are used to infer dynamic parameters. The choice of the source time function has a dramatic impact on the dynamic traction evolution. The shape of the slip-weakening curve, the ratio between D_c (slip weakening distance) and D_{tot} (final slip), and the breakdown work (W_b) distribution are remarkably affected by the adopted source time functions.

We propose the adoption in kinematic inversions of source time functions compatible with earthquake dynamics, because they are able to better constrain the kinematic rupture models, which are fundamental to infer dynamic properties of real earthquakes.

We investigate the effect of different source time functions on ground motion and on radiated seismic energy. We find that the computed ground motions depend on the choice of the STF, especially at stations located near the source (within about 10 km from the fault). In particular, the comparison of the amplitude spectra highlights that dynamically consistent source time functions have a greater high frequency content in the considered frequency range and therefore they are able to better constrain the details of the earthquake rupture in the near field. We estimate the far field S-waves contribution to radiated energy (E_r) of each source model. We see that the adopted source time functions affect the mean-square S-wave velocity (*rms*) source spectrum and the cumulative seismic energy flux estimates.

These results stress the need of developing more physically constrained and dynamically consistent kinematic source characterizations; they could have important implications for earthquake energy balance estimates and for deterministic ground motion prediction.

Finally, we investigate the influence of some kinematic source parameters on the ground motion variability and on shaking scenario selection.

We show a strategy to deterministically compute a large ensemble of synthetic ground motion scenarios, taking into account a great variability of the kinematic source parameters. In particular, we focus on the ground motion sensitivity with respect to nucleation point, rupture velocity, slip distribution and source time function. We simulate a total of 300 earthquake scenarios at 43 sites, by varying the kinematic parameters of interest and by adopting a fault mechanism similar to the 1980 Irpinia, Italy, earthquake (M_s 6.9). From the synthetic time series at each site we obtain two ground motion parameters: the peak ground displacement (PGD) and the peak ground velocity (PGV). We quantitatively analyze the effect of each kinematic source parameter on the PGV and PGD estimates. We see that the rupture velocity and the position of the nucleation point strongly affect the

resulting peak ground motion parameters, and that the largest variations are observed along the forward directivity direction. The analytical form of the slip velocity source time function has also a significant effect. Dynamically consistent STFs contribute to the highest values of ground motion scenario. These results confirm the importance of understanding the slip velocity source behavior in the near-fault region. The comparison of predicted peak ground motions with the empirical model of Sabetta and Pugliese (1996) validates the reliability of the ground-motion simulation strategy we propose. We use the ensemble of the simulated ground motion parameters, (PGD and PGV), to select one or more representative scenarios matching specific criteria, and we show how it is often hard to define a common set of kinematic source parameters that fit the requirements of a specific scenario. This is due to (our still) limited knowledge of the source.

We suggest that much efforts should be focused on improving our ability to accurately estimate the most critical kinematic source parameters influencing the ground motion. This task is essential to model ground shaking scenarios for seismic-hazard assessment in area of strategic and/or priority interest.

We think that the present work gives a robust and reliable modeling of the seismic source, thus providing very useful hints to understand and to correctly represent the real earthquake processes.

Appendix

Blind test for kinematic source inversion

1. Description

Kinematic source inversion of near-fault data allows to retrieve important properties of earthquake ruptures, such as the distribution of the slip, the rupture timing, and, with limitations, the local slip-function. With that, kinematic source inversions have become a crucial input for dynamic modeling of the faulting process. The challenge these kinematic source models have to face is the resolution of the model parameters (slip, rupture velocity etc.). In fact, depending on the inversion strategy, the *a priori* assumptions on the rupture and on the Earth properties, the data processing and data selection, the final slip maps and distribution of rupture onset times are generally different, sometimes even incompatible with each other. The "Blind Test for Kinematic Source Inversion" (http://www.seismo.ethz.ch/staff/martin/BlindTest.html) is an interesting project basing on the idea that one research group generates near-source ground-motions for some scenario earthquake, and provides these synthetics to researchers who then conduct the source inversion. The correct solution of the earthquake rupture model is hence known only to one person/group, while interested participants can apply whatever inversion strategy to solve for the model parameters. The goal of this endeavor is to compare different inversion methods in terms of resolution and efficiency, to assess their weaknesses and strength, and to understand their limits and advantages. This will also help us to better understand the general properties of such inversion techniques, and perhaps aid in the future development of improved methods. This blind test for kinematic source inversion has been initially carried out within the frame work of the EC-project SPICE (**S**eismic Wave **P**ropagation and **I**maging in **C**omplex Media: A **E**uropean Network), but then it has been opened to participants who are not directly involved in the SPICE-project.

The general rules of the blind test are as follows:

• the test is based on a fault geometry and station distribution similar to the 2000 western Tottori earthquake, with a denser coverage of stations in the fault vicinity;
• the dimensions of the rupture plane are not known *a priori*, but it is embedded within a rectangular fault area of dimensions L_{max} and W_{max}. The dimension of the earthquake rupture (i.e. source extent), however, is compatible with source-scaling relations;
• the moment tensor (CMT) solution is known, i.e. strike φ, rake angle λ and dip δ of the fault are given. Likewise the final seismic moment M_o, the hypocenter location and the origin time are given;
• Earth's structure is assumed to be a vertically layered medium; the velocity-density model is given;
• any "inverter" is free to choose whatever method he/she desires to use to carry out the source inversion. There are no constraints on the fitness function to be used. The only requirement is that the methodology is clearly documented. In order to test the capabilities of current source-inversion approaches under different conditions, the blind-test exercise will consist of three stages with increasing complexity in the earthquake rupture model:

1. stage I: the slip is heterogeneous, while rupture velocity and rise-time are constant. All those parameters are unknown to the "inverters". The slip-velocity function used for computing the to-be inverted ground-motions is simple. Synthetics are generated without any random noise on the signals;
2. stage II: slip, rupture velocity and rise-time are heterogeneous; additionally a more complex (realistic) slip-velocity may be used. No noise is added to the synthetics signals;
3. stage III: same as in (2), but now random noise is added to the synthetics.

2. Results

In this section we report the results collected for the stage I (see previous section) and presented during the 2007 AGU Fall Meeting, San Francisco (*Mai et al.*, 2007). Nine source-inversion results (J. Burjanek, B. Delouis, M. Causse, A. Cirella, G. Festa, C. Francois-Holden, D. Monelli, T. Uchide, J. Zahradnik) have been submitted (Figure 1):

Model A: multiple point-source model (iterative moment-tensor deconvolution), GF's with AXITRA (fmax = 1 Hz) , [1 x 1] km large subfaults, solving for final slip by some search algorithm;

Model B: Non-linear inversion using a Neighborhood algorithm; GF's with AXITRA (fmax = 1 Hz);[2.5 x 2.7] km large subfaults, solving for final slip and rupture velocity, minimizing L2-norm;

Model C : Isochrone back-projection of high frequency displacements (up to high ÷1Hz); [2 x 2] km subfaults, solving for slip and rupture time, minimizing L2-norm;

Model D: Non-linear inversion by simulated annealing, L2-norm fitness function with minimization of the total seismic moment; GF's with AXITRA, [2 x 2] km large subfaults;

Model E: linearized inversion for slip using Gaussian basis functions, L2-norm minimization (with positivity constraint), [1 x 1] km subfaults, solving for final slip;

Model F: Non-linear inversion with evolutionary algorithm; GF's with COMPSYN; x 3] km subfaults, solving for slip and rupture time;

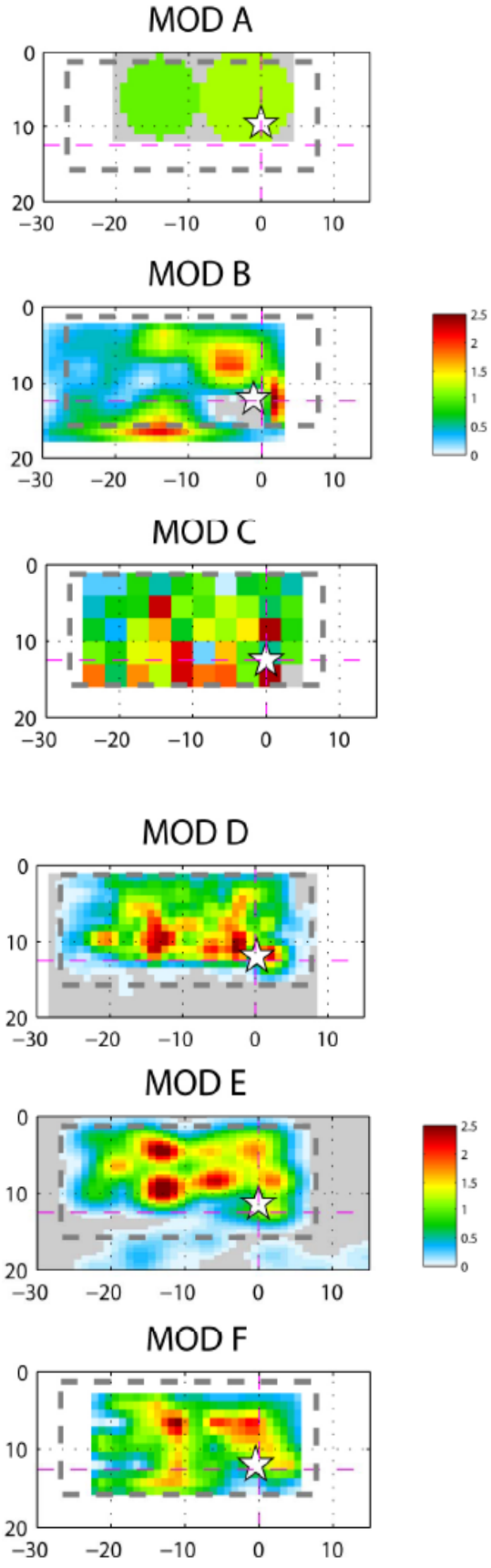

Model G: Frequency-domain inversion on displacement seismogram; GF's with AXITRA; subfault size of 2.5 x 2.5 km;

Model H (this is our model):
non-linear joint inversion of strong motion and GPS data; GF's with COMPSYN;
subfault size [3 x 3] km;
all kinematic parameters are allowed to vary;

Model I: linearized inversion, using linear B-splines as spatial and temporal basis functions, subfault size [2 x 2] km;

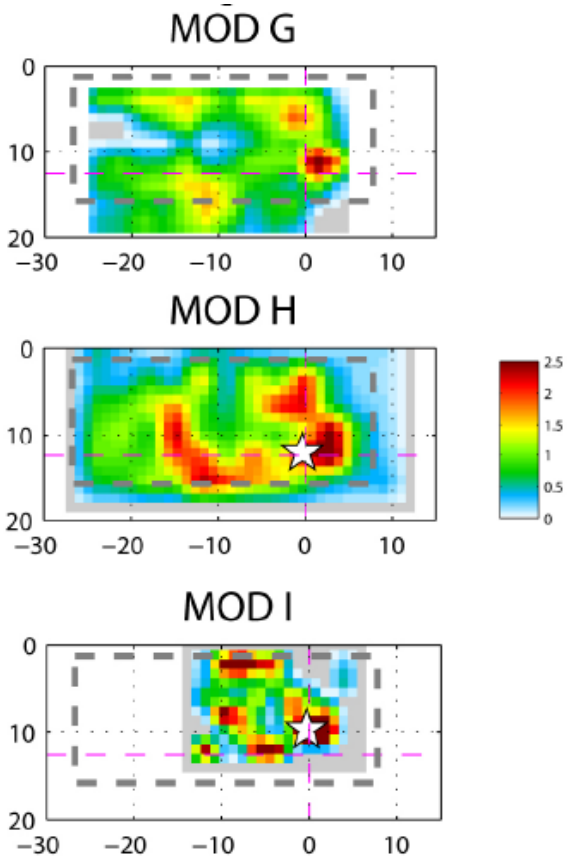

Figure1. Rupture models inferred from the different participants to the Blind Test.

Model H correspond to our model.

The awaited answer is showed in Figure 2.

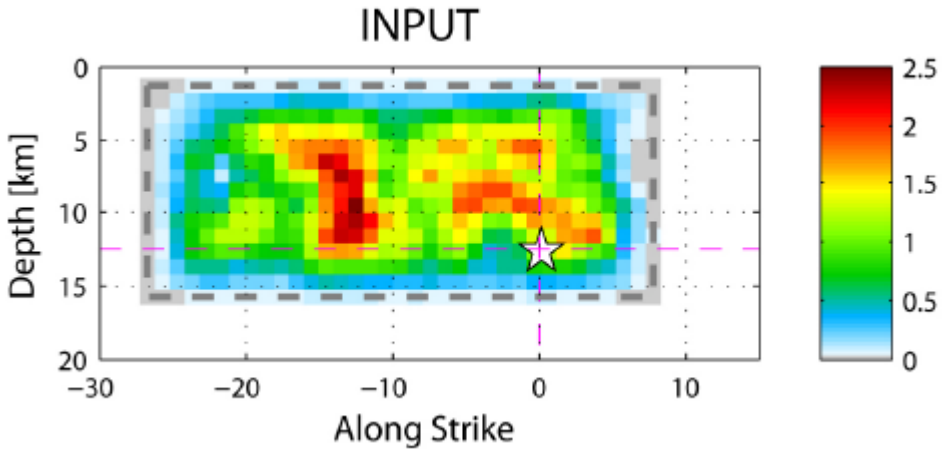

Figure2. Input model used in the Blind Test.

Results 1: Estimated rupture velocity, rise time, overall slip-value distribution

Figure 3 (upper panel) shows the estimates of rupture velocity in the expected range; how we can see two solutions falls off significantly, under- or over-estimating rupture velocity by ~20%. Estimates for rise time (τ_r) are in the expected range, though 2/3 of the models have ~20% longer rise times, perhaps due to waveform filtering at ~1Hz (Figure 3, bottom panel). Our model (model H) shows an excellent agreement with the input model, in terms of inferred rupture velocity and rise time average values.

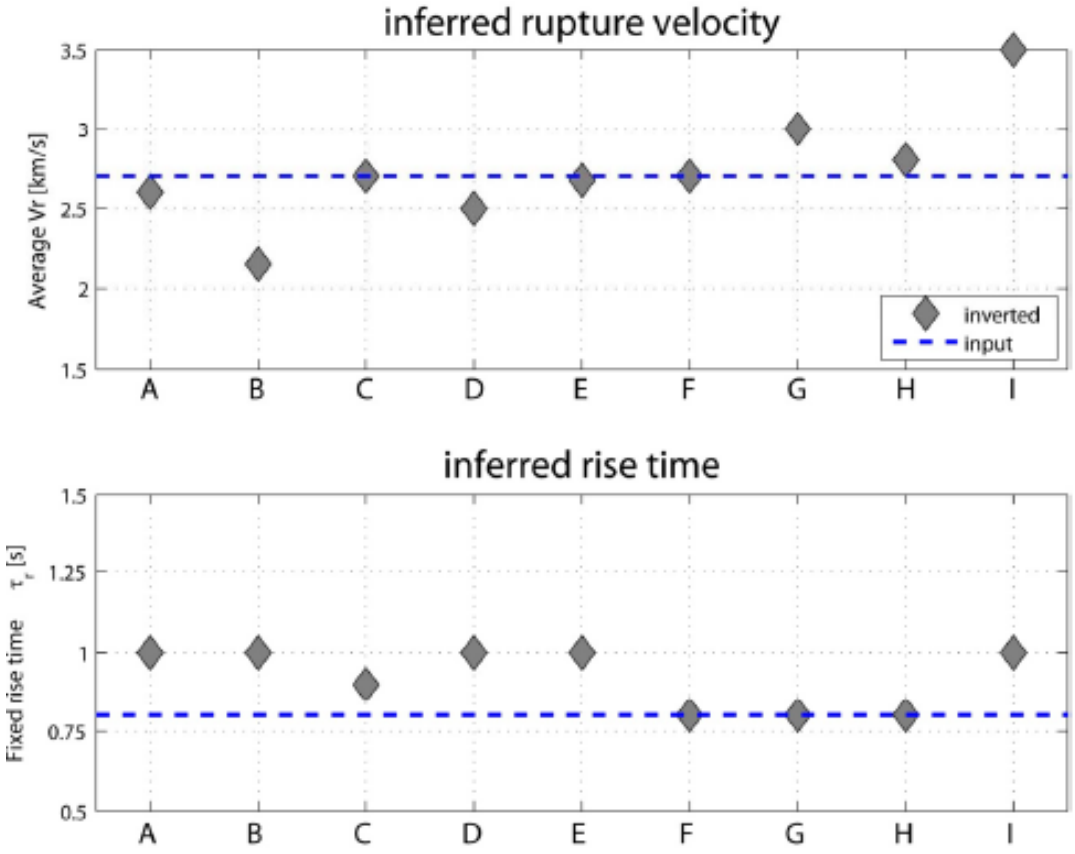

Figure3. Comparison between input model and inverted models. Estimates for rupture velocity (upper panel). Estimates for rise time (bottom panel).

The resulting slip-value distributions are generally quite different amongst each other, and also with respect to the input distribution (Figure 4).

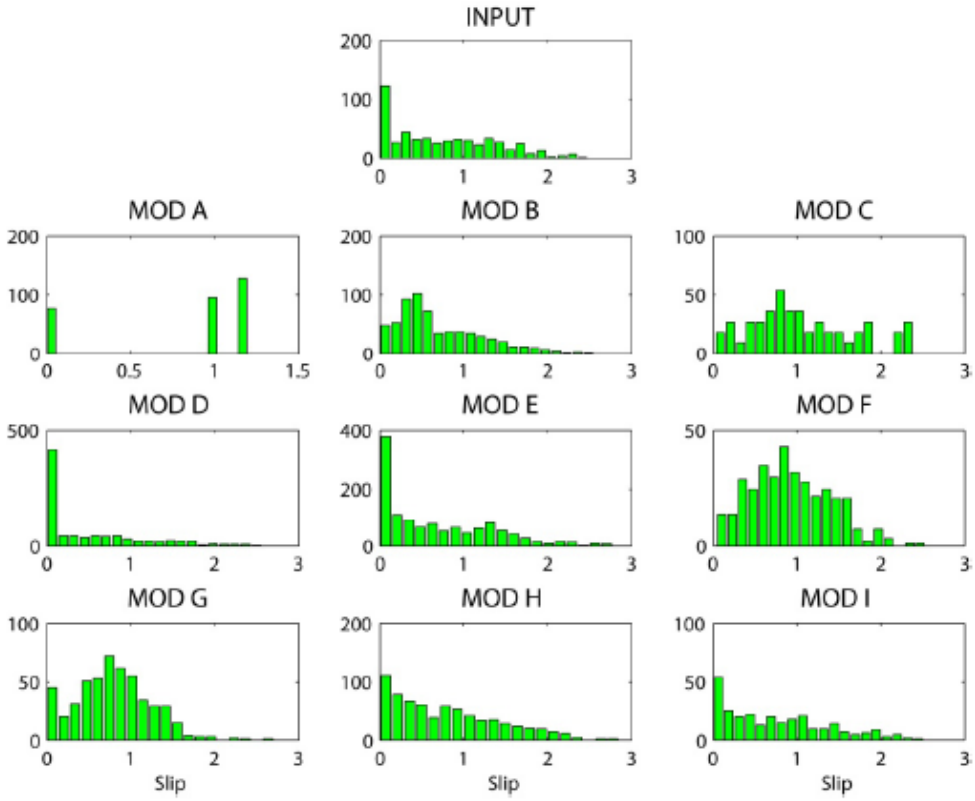

Figure 4. Slip-value distribution for the different retrieved models and for the input model.

Results 2: Slip distributions on the fault plane

The different slip models are quantitatively compared through the analysis of the 2D-cross-correlation (CC) between the input and the inverted models.

To calibrate the results, a purely random field (Figure 5, left side) and a random, but correlated field (Figure 5, right side) are tested.

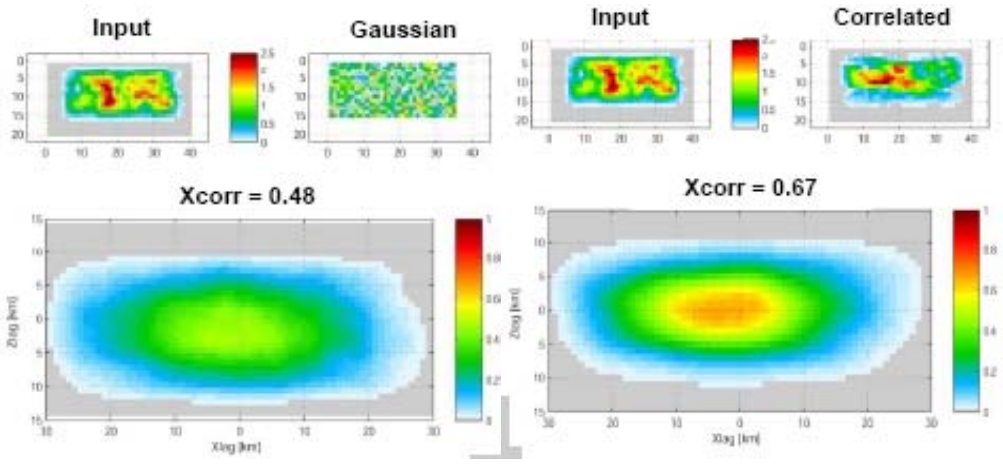

Figure5. 2D-cross correlation calibration. Test with a purely random field is showed on the left side. Test with a random, but correlated field is showed on the right side.

Figure 6 shows that 4 out of 9 inversion results show a CC-coefficient like a random, but correlated model, while 5 out of 9 cases show a correlation coefficient of ~ 0.9, while the lag is small (~ 2 km).

Our model (Model H) is among these latter models.

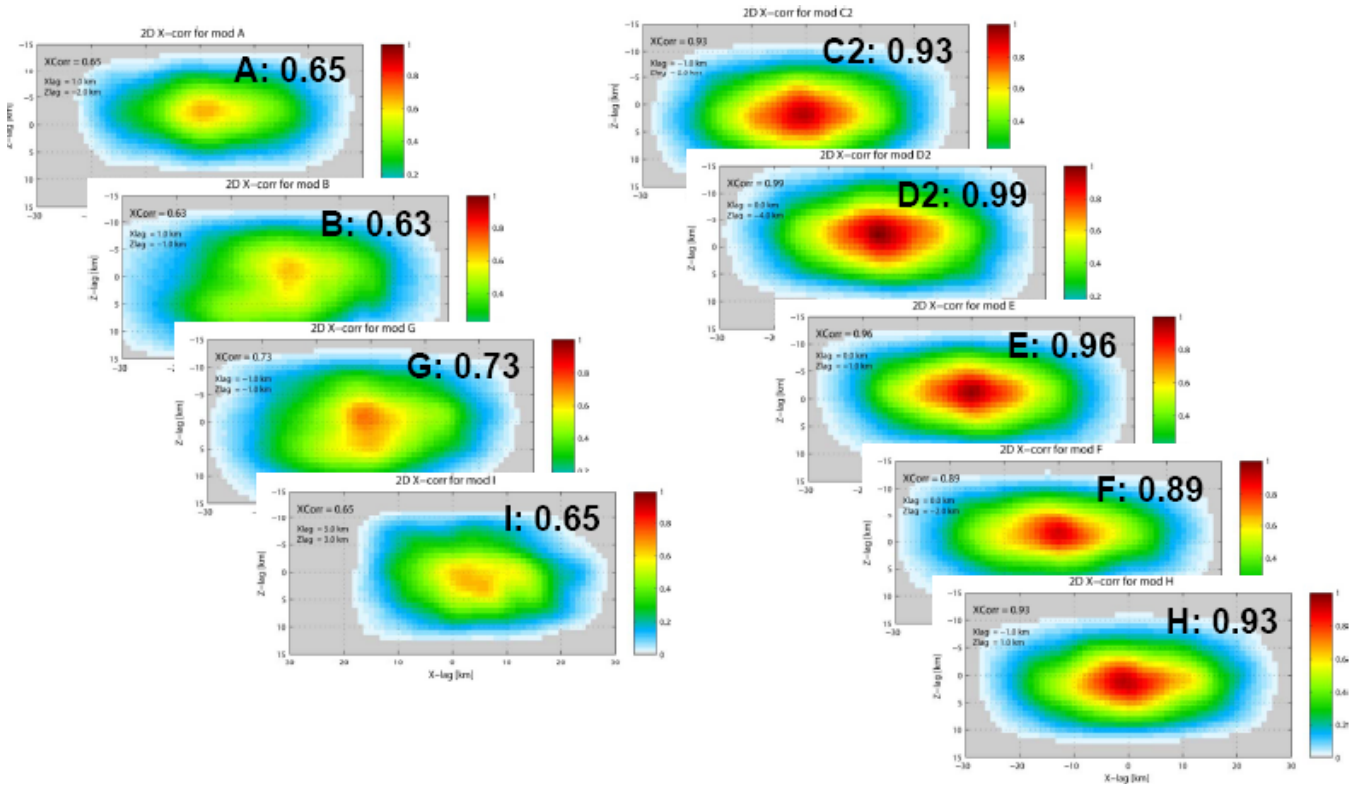

Figure 6. Cross Correlation Coefficient computed for all the retrieved models.

The Blind Test offers us the opportunity to test and validate our earthquake source inversion method; with the aim to assess its weaknesses and strength, and to understand its limits and advantages.

References

Amato, A., and Selvaggi G. (1993), Aftershock location and P-velocity structure in the epicentral region of the 1980 Irpinia earthquake, *Annali di Geofisica*, 36, 3-15.

Ambraseys, N. N., Simpson K. A., Bommer J. J. (1996), Prediction of horizontal response spectra in Europe, *Earthquake Engineering and Structural Dynamics*, 25, 371-400.

Ambraseys, N. N., and Simpson K. A. (1996), Prediction of vertical response spectra in Europe, *Earthquake Engineering and Structural Dynamics*, 25, 401-412.

Ambraseys, N. N., Douglas, J., Sarma, S. K., Smit, P. M. (2005), Equations for the estimation of strong ground motion from shallow crustal earthquakes using data from Europe and the Middle East: Horizontal Peak Ground Acceleration and Spectral Acceleration, *Bulletin of Earthquake Engineering*, 3, 1-53.

Anderson, J. (1974), A dislocation model for the Parkfield earthquake, *Bull. Seismol. Soc. Am.*, 64(3-1), 671– 686.

Andrews, D. J. (1976), Rupture velocity of plane strain shear cracks, *J. Geophys. Res.*, 81, 32, 5679-5687.

Andrews, D. J. (1999), Test of two methods for faulting in finite-difference calculations, *Bull. Seismol. Soc. Am.*, 89(4), 931–937.

Andrews, D. J., and Hanks T. C. (2007), Physical Limits on Ground Motion at Yucca Mountain, *Bull. Seismol. Soc. Am.*, 97, 1771-1792.

Aki, K. (1968), Seismic displacements near a fault, *J. Geophys. Res.* 73, 5359–5376.

Aki, K., and P. G. Richards, (1980), *Quantitative Seismology, Theory and Methods* vol.I, Freeman, San Francisco.

Aki, K., and P. G. Richards (2002), *Quantitative Seismology (second edition).* University Science Books.

Aoi, S., H. Sekiguchi, N. Morikawa, T. Ozawa, T. Kunugi, M. Shirasaka (2007), Source process of the 2007 Niigata-ken Chuetsu-oki earthquake derived from near-fault strong motion data, *Eos, Trans. AGU 87*(52), Fall Meet. Suppl., Abstract S54A-04.

Archuleta, R. J. (1982), Hypocenter for the 1979 Imperial Valley earthquake, *Geophys. Res. Lett.* 9, 625–628.

Archuleta, R. J. (1984), A faulting model for the 1979 Imperial Valley earthquake, *J. Geophys. Res.*, 89, 4559-4585.

Bazzurro, P. and C. A. Cornell (1999), Disaggregation of Seismic Hazard. *Bull. Seismol. Soc. Am*. 89, 2, 501-520.

Belardinelli, M. E., M. Cocco, O. Coutant, and F. Cotton (1999), Redistribution of dynamic stress during coseismic ruptures: Evidence for fault interaction and earthquake triggering, *J. Geophys. Res.,* 104(B7), 14, 925-14, 945.

Belardinelli, M. E., A. Bizzarri, and M. Cocco (2003a), Earthquake triggering by static and dynamic stress changes, *J. Geophys. Res.,* 108(B3), doi:10.1029/2002JB001779.

Belardinelli, M. E., L. Sandri, and P. Baldi (2003b), The major event of the 1997 Umbria-Marche (Italy) sequence: what could we learn from DInSAR and GPS data? *Geophys .J. Int.,* 153, 242-252.

Bender, B. (1986), Modeling source zone boundary uncertainty in seismic hazard analysis, *Bull. Seism. Soc. Am.,* 76: 329-341.

Beresnev, I. A. (2003), Uncertainties in finite-fault slip inversions: to what extent to believe? (A critical review), *Bull. Seismol. Soc. Am.*, 93, 2445-2458.

Bernard, P., and R. Madariaga (1984). A new asymptotic method for the modeling of near-field accelerograms, *Bull. Seismol. Soc. Am.* 74, 539-558.

Beroza, G. C., and P. Spudich (1988), Linearized inversion for fault rupture behaviour: application to the 1984 Morgan Hill, California, earthquake, *J. Geophys. Res.*, 93(B6), 6275-6296.

Beroza, G. C. (1996), Rupture history of the earthquake from high frequency strong motion data, in the Loma Prieta, California, earthquake of October 17, 1989—main shock characteristics, *U.S. Geol. Surv. Profess. Pap. 1550-A, P. Spudich (Editor)*, 9–32.

Bizzarri, A., Cocco M., Andrews D. J., Boschi E., (2001), Solving the dynamic rupture problem with different numerical approaches and constitutive laws, *Geophys. J. Int*. 144, 656-678.

Boatwright, J., and G. L. Choy (1992), Acceleration source spectra anticipated for large earthquakes in northeastern North America, *Bull. Seismol. Soc. Am.* 82, no. 2, 660–682.

Boatwright, J., G. L. Choy, and L. C. Seekins (2002), Regional estimates of radiated seismic energy, *Bull. Seismol. Soc. Am.* 92, 1241–1255.

Boatwright, J., A. Venkataraman, K. Mayeda, G. L. Choy and M. Cocco (2005), Radiated seismic energy and mean square source spectral comparison for large earthquakes, *AGU Fall Meeting 2005*, San Francisco.

Bommer, J. J., J. Douglas, and F. O. Strasser (2003), Style-of-faulting in ground-motion prediction equations, *Bull. Earthquake Eng.* 1, no. 2, 171–203.

Boore, D. M. and M. D. Zoback (1974), Near-field motions from kinematic models of propagating fault, *Bull. Seismol. Soc. Am. 64*, 321-342.

Bouchon, M. (1979), Predictability of ground displacement and velocity near an earthquake fault: the Parkfield earthquake of 1966, *J. Geophys. Res.,* 84, 6149-6156.

Boschi, E., and M. Dragoni (2000), *Sismologia*. Edizioni UTET, Torino.

Bouchon, M. (1982), The rupture mechanism of the Coyote Lake earthquake of 6 August 1979 inferred from near-field data, *Bull. Seismol. Soc. Am.,* 72, 745-759.

Bouchon, M. (1997), The state of stress on some faults of the San Andreas system as inferred from near-field strong motion data, *J. Geophys. Res.* 102, 11,731–11,744.

Bouchon, M., M. Campillo, and F. Cotton (1998), Stress field associated with the rupture of the 1992 Landers, California, earthquake and its implications concerning the fault strength at the onset of the earthquake, *J. Geophys. Res.*, 103(B9), 21, 091– 21, 097.

Bouchon, M., M. P. Bouin, H. Karabulut, M. N. Toksos, M. Dietrich, and A. J. Rosakis (2001), How fast is rupture during an earthquake? New insights from the 1999 Turkey earthquakes, *Geophys. Res. Lett*., 28, no.14, 2723-2726.

Bouchon, M., M. N. Toksо¨z, H. Karabulut, M. P. Bouin, M. Dietrich, M. Aktar, and M. Edie (2002), Space and time evolution of rupture and faulting during the 1999 Izmit (Turkey) earthquake, *Bull. Seismol. Soc. Am.,* 92, 256–266.

Burridge, R., and Knopoff L., (1964), Body force equivalents for seismic dislocations, *Bull. Seismol. Soc. Am.,* 54, 1875–1888.

Campillo, M., and Bouchon, M. (1983), A theoretical study of the radiation from small strikeslip earthquakes at close distances, *Bull. Seismol. Soc. Am.,* 73, 83-96.

Carlson, J. and J. Langer (1989), Mechanical model of an earthquake fault, *Phys. Rev.,* A 40, 6470-6484.

Choy, G. L., and J. L. Boatwright (1995), Global patterns of radiated seismic energy and apparent stress, *J. Geophys. Res.,* 100, 18, 205–18, 228.

Cirella, A., A. Piatanesi, E. Tinti and M. Cocco (2006), Dynamically consistent source time functions to invert kinematic rupture histories, *Eos, Trans. AGU 87*(52), Fall Meet. Suppl., Abstract S41B-1323.

Cochard, A. and R. Madariaga (1994), Dynamic faulting under rate-dependent friction, *Pageoph,* 142, 419-445.

Cohee, B. P. and G. C. Beroza (1994), A comparison of two methods for earthquake source inversion using strong motion seismograms, *Annali di Geofisica,* 37, 6, 1515-1538.

Cornell, C. A., (1968), Engineering seismic hazard analysis, *Bull. Seismol. Soc. Am.,* 59 (5), 1583–1606.

Cotton, F., and M. Campillo (1995), Frequency domain inversion of strong motions: application to the 1992 Landers earthquake, *J. Geophys. Res.,* 100, 3961–3975.

Custodio, S., and R. J. Archuleta (2007), Parkfield earthquakes: Characteristic or complementarity ?, *J. Geophys. Res.*, 112, B05310, doi: 10.1029/2006JB004617.

Dalguer, L. A, Irikura K, Riera J. and Chiu H. C (2001a), Fault dynamic rupture simulation of the hypocenter area of the thrust fault of the 1999 Chi-Chi (Taiwan) earthquake, *Geophys. Res. Lett.*, April 1,vol. 28, no. 7, 1327-1330.

Dalguer, L. A, Irikura K, Riera J. and Chiu H. C (2001b), The importance of the dynamic source effects on strong ground motion during the 1999 Chi-Chi (Taiwan) earthquake: brief interpretation of the damage distribution on buildings, *Bull. Seismol. Soc. Am.*, 95, 1112-1127.

Dalguer, L. A., K. Irikura, W. Zhang, and J. D. Riera (2002), Distribution of dynamic and static stress changes during 2000 Tottori (Japan) earthquake: brief interpretation of the earthquake sequences; foreshocks, mainshock and aftershocks, *Geophys. Res. Lett*., 29(16), 1758, doi:10.1029/2001GL014333.

Das, S. and Aki, K. (1977), A numerical study of two-dimensional spontaneous rupture propagation, *Geophys. J. R. Astr. Soc*., 50, 643-668.

Das, S., and B. V. Kostrov (1990), Inversion for seismic slip rate and distribution with stabilising constraints: application to the 1986 Anreanof Islands earthquake, *J. Geophys. Res.*, 95, 6899–6913.

Das, S., and P. Suhadolc (1996), On the inverse problem for earthquake rupture: the Haskell-type source model, *J. Geophys. Res.,* 101, 5725–5738.

Day, S. (1982), Three-dimensional finite-difference simulation of fault dynamics: rectangular faults with fixed rupture velocity, *Bull. Seismol. Soc. Am.*, 72, 705-727.

Day, S. M., G. Yu, and D. J. Wald (1998), Dynamic stress changes during earthquake rupture, *Bull. Seismol. Soc. Am.*, 88(2), 512– 522.

Delouis, B, Giardini D., Lundgren P. and Salichon J. (2002), Joint inversion of Insar, GPS, teleseismic and strong-motion data for the spatial and temporal distribution of earthquake slip: application to the 1999 Izmit mainshock, *Bull. Seismol. Soc. Am.*, 92(1), 278-299.

Dieterich, J. (1978), Time-dependent friction and the mechanics of stickslip, *Pageoph.*, 116, 790-806.

Douglas, J. (2003), Earthquake ground motion estimation using strong motion records: A review of equations for the estimation of peak ground accelerations and response spectral ordinates, *Earth Sci. Rev.*, 61, 43–104.

Dreger, D., and A. Kaverina (2000), Seismic remote sensing for the earthquake source process and near-source strong shaking: A case study of the October 16, 1999 Hector Mine earthquake, *Geophys. Res. Lett.*, 27, 1941-1944.

Dreger D., Tinti E., and A. Cirella, (2007), Slip velocity parameterization for broadband ground motion simulation, *Seismological Society of America* 2007 Annual Meeting abstract.

Emolo, A. and A. Zollo (2005), Kinematic source parameters for the 1989 Loma Prieta earthquake from the nonlinear inversion of accellerograms, *Bull. Seismol. Soc. Am.*, 95(3), 981-994, doi:10.1785/0120030193.

Festa, G. and Zollo A. (2006), Fault slip and rupture velocity inversion by isochrone backprojection, *Geophys. J. Int.*, 166, 745-756, doi:10.1111/j.1365-246X.2006.03045.x.

Frankel, A. and Wennerberg L., (1989), Rupture process of the Ms 6.6 Superstition Hills, California, earthquake determined from strong-motion recordings: application of tomographic source inversion, *Bull. Seismol. Soc. Am.*, 79, 515-541.

Fukuyama, E., and K. Irikura, (1986), Rupture process of the 1983 Japan Sea (Akita-Oki) earthquake using a waveform inversion method, *Bull. Seismol. Soc. Am.*, 76, 1623-1640.

Fukuyama, E., and T. Mikumo (1993), Dynamic rupture analysis: inversion for the source process of the 1990 Izu-Oshima, Japan, earthquake (*M* _ 6.5), *J. Geophys. Res.*, 98, 6529–6542.

Fukuyama, E., and R. Madariaga (1998), Rupture dynamics of a planar fault in a 3D elastic medium: rate- and slip-weakening friction, *Bull. Seismol. Soc. Am.*, 88, 1–17.

Fukuyama, E., and R. Madariaga (2000), Dynamic propagation and interaction of a rupture front on a planar fault, *Pure Appl. Geophys.*, 157, 1959–1979.

Fukuyama, E., W. L. Ellsworth, F. Waldhauser and A. Kubo (2003), Detailed fault structure of the 200 western Tottori, Japan, earthquake sequence, *Bull. Seismol. Soc. Am.*, 93, 1468-1478.

Fukuyama, E., and T. Mikumo (2007), Slip-weakening distance estimated at near-fault stations, *Geophys. Res. Lett., 34*, L09302, doi:10.1029/2006GL029203.

Gallovic, F. and Brokesova, J. (2007), Hybrid k-squared source model for strong ground motion simulations: Introduction, *Physics .Earth. Planet. Int*., 160, 34-50.

Geman, S., and D. Geman (1984), Stochastic relaxation, Gibbs distribution and the Bayesian restoration of images, *IEEE Trans. Patt. Anal. Mach. Int*., 6, 721-741.

Graves, R. W. and D. J Wald (2001), Resolution analysis of finite source inversion using one- and three-dimensional Green's functions: 1. Strong motions, *J. Geophys. Res.*, 106(B5), 8745-8766.

Guatteri, M., and P. Spudich (2000), What can strong motion data tell us about slip-weakening fault-friction laws? *Bull. Seismol. Soc. Am.*, 90, 98-116.

Guatteri, M., P. M. Mai, G. C. Beroza, and J. Boatwright (2003), Strong ground-motion prediction from stochastic-dynamic Source Models, *Bull. Seismol. Soc. Am.*, 93, no.1, 301-313.

Gutenberg, B., and C. F. Richter (1942), Earthquake magnitude, intensity, energy and acceleration, *Bull. Seismol. Soc. Am.* 32, 163–191.

Gutenberg, B., and C. F. Richter (1956), Earthquake magnitude, intensity, energy, and acceleration, *Bull. Seismol. Soc. Am.* 46, 105–145.

Hammersley, J. M., and D. C. Handscomb, (1964), *Monte Carlo Methods*, Chapman and Hall, New York.

Hartzell, S., and Helmberger, D. (1982), Strong-motion modeling of the Imperial Valley earthquake of 1979 *Bull. Seismol. Soc. Am.*, 72, 571-596.

Hartzell, S. and T. H. Heaton (1983), Inversion of strong ground motion and teleseismic waveform data for the fault rupture history of the 1979 Imperial Valley, California earthquake, *Bull. Seismol. Soc. Am.*, 73, 1553-1583.

Hartzell, S. and T. H. Heaton (1986), Rupture history of the 1984 Morgan Hill, California, earthquake from the inversion of strong motion records, *Bull. Seismol. Soc. Am.*, 76, 649-674.

Hartzell, S. H. (1989), Comparison of seismic waveform inversion results for the rupture history of a finite fault: Application to the 1986 North Palm Springs, California, earthquake, *J. Geophys. Res.*, 94, 7515–7534.

Hartzell, S., and C. Langer (1993), Importance of model parameterization in finite fault inversions: application to the 1974 *M*W 8.0 Peru earthquake, *J. Geophys. Res.*, 98, 22, 123–22, 134.

Hartzell, S, and P. Liu, (1995), Determination of earthquake source paramenters using a Hybrid Global Search Algorithm, *Bull. Seismol. Soc. Am.*, 85, 516 – 524.

Hartzell, S. H., P.-C. Liu, and C. Mendoza (1996), The 1994 Northridge earthquake: investigation of rupture velocity, rise time and high frequency radiation, *J. Geophys. Res*., 101, 20, 091–20, 108.

Haskell, N. A. (1969), Elastic displacements in the near-field of a propagating fault, *Bull Seism. Soc. Am.* 59, 865-908.

Heaton, T. H., and Helmberger, D. V. (1979), Generalized ray models of the San Fernando earthquake, *Bull. Seismol. Soc. Am.*, 69, 1311-1341.

Heaton, T. H. (1982), The 1971 San Fernando earthquake: A double event? *Bull. Seismol. Soc. Am.*, 72, 2037-2062.

Heaton, T. H. (1990), Evidence for and implications of self-healing pulses of slip in earthquake rupture, *Phys. Earth Planet, Inter.* 64, 1–29.

Herrero, A. and P. Bernard (1994), A kinematic self-similar rupture process for earthquakes, *Bull. Seismol. Soc. Am.*, 84, 1216-1228.

Hisada, Y. (2000)., A theoretical omega-square model considering the spatial variation in slip and rupture velocity, *Bull. Seismol. Soc. Am.*, 90, 387– 400.

Hisada, Y. (2001), A theoretical omega-square model considering the spatial variation in slip and rupture velocity. II. Case for a twodimensional source model, *Bull. Seismol. Soc. Am.* 91, 651–666.

Houston, H., and H. Kanamori (1990), Comparison of strong motion spectra with teleseismic spectra for three magnitude 8 subduction-zone earthquakes, *Bull. Seismol. Soc. Am.*, 80, 913– 934.

Hudnut, K. W., Y. Bock, M. Cline, P. Fang, J. Freymuller, K. Gross, D. Jackson, S. Larson, M. Lisowski, Z. Shen and J. Svarc (1996), Coseismic displacements of the 1994 Northridge, California earthquake, *Geol. Soc. Am. Bull.*, 86, no. 1B, S19-S36.

Ichikawa M. (1971), Reanalyses of mechanism of earthquakes which occurred in and near Japan, and statistical studies on the nodal plane solutions obtained, 1926–1968, *Geophys. Mag. Tokyo*, 35, 207–274.

Ida Y. (1972), Cohesive force across the tip of a longitudinal shear crack and Griffith' specific surface energy, *J. Geophys. Res.*, 77, 3796–3805.

Ide, S., M. Takeo, and Y. Yoshida (1996), Source process of the 1995 Kobe earthquake: determination of spatio-temporal slip distribution by Bayesian modeling, *Bull. Seismol. Soc. Am.*, 86, 547–566.

Ide, S. and M. Takeo (1997), Determination of constitutive relations of fault slip based on seismic wave analysis, *J. Geophys. Res.*, 102(B12), 27379-27391.

Irikura, K., H. Miyake, T. Iwata, K. Kamae, H. Kawabe, and L. A. Dalguer (2004), Recipe for predicting strong ground motion from future earthquakes, No. 1371, *Proceedings of the 13th World Conference on Earthquake Engineering.*

Irikura, K., T. Kagawa, K. Miyakoshi, S. Kurahashi (2007), Rupture process and strong motions of the 2007 Niigata-ken Chuetsu-Oki earthquake –Directivity pulses striking the Kashiwazaki-Kariwa Nuclear Power Plant, *Eos, Trans. AGU 87*(52), Fall Meet. Suppl., Abstract S31B-0441.

Iwata, T and H. Sekiguchi (2002), Source process and near-source ground motion during the 2002 Tottori-ken-Seibu earthquake, *Proc. 11th Japan Erthq. Eng. Symp*, 125-128, (in japanease with english abstract).

Ji, C., D. J. Wald, and D. V. Helmberger (2002), Source description of the 1999 Hector Mine, California, earthquake, Part I: Wavelet domain inversion theory and resolution analysis, *Bull. Seismol. Soc. Am.*, 92 (4), 1192-1207.

Kagawa, T., K. Irikura, and P. G. Somerville (2004), Differences in ground motion and fault rupture process between the surface and buried rupture earthquakes, *Earth Planets Space*, 56(1), 3 – 14.

Kanamori, H., J. Mori, E. Hauksson, T. H. Heaton, L. K. Hutton, and L. M. Jones (1993), Determination of earthquake energy release and M_L using Terrascope, *Bull. Seismol. Soc. Am.*, 83, 330–346.

Kato, A., E. Kurashimo, N. Hirata, S. Sakai, T. Iwasaki and T. Kanazawa (2005), Imaging the source region of the 2004 mid-Niigata prefecture earthquake and the evolution of a seismogenic thrust-related fold, *Geophys. Res. Lett*., 32, L07307, doi:10.1029/2005GL022366.

Kaverina, A., D. Dreger, and E. Price (2002), The combined inversion of seismic and geodetic data for the source process of the 16, October, 1999, Mw_7.1, Hector Mine, California earthquake, *Bull. Seismol. Soc. Am.*, Special issue on Hector Mine earthquake, 92, no. 4, 1266–1280.

Kennett, B. L. N. (1998), On the density distribution within the Earth, *Geophysics. J. Int*., 132, 374-382.

Kennett, B. L. N. (2004), Consistency regions in non-linear inversion, *Geophys. J. Int.*, 157, 583-588.

Kikuchi, M., and Y. Fukao (1988), Seismic wave energy inferred from long-period body wave inversion, *Bull. Seismol. Soc. Am.*, 78, 1707–1724.

Kirkpatrick, S.C., D. Gelatt, and M. P. Vecchi (1983), Optimization by simulated annealing, *Science*, 220, 671-680.

Koketsu, K., H. Miyake, K. Hikima (2007), Source inversion for the 2007 Chuetsu-oki, Japan, earthquake: A case of difficulty determining the source fault plane, *Eos, Trans. AGU 87*(52), Fall Meet. Suppl., Abstract S54A-05.

Kostrov, B. V., and S. Das (1988), *Principles of earthquake source mechanics*, Cambridge University Press.

Liu, H. L., and Helmberger, D. V. (1983),The near-source ground motion of the 6 August 1979 Coyote Lake, California, earthquake, *Bull. Seismol. Soc. Am.*, 73, 201-218.

Liu, P., and R. Archuleta (2004), A new nonlinear finite fault inversion with three-dimensional Green's functions: application to the 1989 Loma Prieta, California, earthquake, *J.Geophys. Res.*, 109, B02318, doi:10.1029/2003JB002625.

Liu, P., S. Custodio and R. J. Archuleta (2006a), Kinematic inversion of the 2004 M 6.0 Parkfield earthquake including an approximation to site effects, *Bull. Seismol. Soc. Am.*, 96, 4B, S143-S158, doi:10.1785/0120050826.

Liu, P., R. J. Archuleta, and S. H. Hartzell (2006b), Prediction of broadband round-motion time histories: Hybrid Low/High-frequency method with correlated random source parameters, *Bull. Seismol. Soc. Am.* 96, no.6, 2118-2130.

Ma, K. F., Song, T. R., Lee, S. J. and Wu, H. I. (2000), Spatial slip distribution of the September 20, 1999, Chi-Chi, Taiwan earthquake Mw = 7.6 - inverted from teleseismic data, *Geophys. Res. Lett*., 27, 3417-3420.

Ma, S., and R. J. Archuleta (2006), Radiated seismic energy based on dynamic rupture models of faulting, *J. Geophys. Res.*, 111, B05315,doi:10.1029/2005JB004055.

Mai, P. M., and G. C. Beroza (2002), A spatial random field model to characterize complexity in earthquake slip, *J. Geophys. Res.* 107, B11, 2308, doi:10.1029/2001JB000588.

Mai P. M., P. Spudich e J. Boatwright (2005), Hypocenter locations in finite-source rupture models, *Bull. Seismol. Soc. Am.*, 95, 965-980.

Mai P. M., J. Burjianek, B. Delouis, M. Causse, A. Cirella, G. Festa, C. Francois-Holden, D. Monelli, T. Uchide, J. Zahradnik (2007), Earthquake source inversion blind test: Initial results and further developments, 2007 AGU Fall Meeting, San Francisco, session S11 ("*Earthquake Source Inversion Under Scrutiny: Validation, Resolution, Robustness"*), abstact SC53-8.

Manighetti I., G. King, Y. Gaudemer, C. Scholz, and C. Doubre (2001), Slip accumulation and lateral propagation of active normal fault in Afar, *J. Geophys. Res*., 106,13667-13696.

Manighetti I., M. Campillo, C. Sammis, P. M. Mai, and G. King (2005), Evidence for self-similar, triangular slip distributions on earthquakes: Implications for earthquake and fault mechanics, *J. Geophys. Res*., 110, B05302, doi:10.1029/2004JB003174.

Menke, W. (1989), *Geophysical Data Analysis: Discrete Inverse Theory*, rev. ed., Academic, San Diego, Calif.

Metropolis, N., M. N. Rosenbluth, A. W. Rosenbluth, A. H. Teller, and E. Teller (1953), Equation of state calculations by fast compute machines, *J. Chem. Phys*., 21, 1087-1092.

Mikumo, T., and T. Miyatake (1995), Heterogeneous distribution of dynamic stress drop and relative fault strength recovered from the results of wave-form inversion-the 1984 Morgan-Hill, California earthquake, *Bull. Seismol. Soc. Am*., 85(1), 178– 193.

Mikumo, T., K. B. Olsen, E. Fukuyama, and Y. Yagi (2002), Stress-breakdown time and slip-weakening distance inferred from slip-velocity functions on earthquake faults, *Bull. Seismol. Soc. Am.*, 93, 264–282.

Mosegaard, K., and A. Tarantola (1995), Monte Carlo sampling of solutions to inverse problem, *J. Geophys. Res.*, 100(B7), 12431-12447.

Mosegaard, K. and M. Sambridge (2002), Monte Carlo methods in geophysical inverse problem, *Rev. Geophys.*, 40(3), 1-29.

Nakajima, J., and A. Hasegawa (2007), Deep crustal structure along the Niigata-Kobe Tectonic Zone, Japan: Its origin and segmentation, *Earth Planets Space*, 59, e5-e8.

Nielsen, S., and R. Madariaga (2003), On the self-healing fracture mode, *Bull. Seismol. Soc. Am.*, 93, 2375–2388.

Nolte, B., and L. N. Frazer (1994), Vertical seismic profile inversion with genetic algorithms, *Geophys. J. Int.*, 117, 162-179.

Oglesby, D. D, R. J. Archuleta and S. B. Nielsen (2000), The three-dimensional dynamics of dipping faults, *Bull. Seismol. Soc. Am.*, 90, 616-628.

Oglesby, D. D., D. S. Dreger, R. A. Harris, N. Ratchkovski and R. Hansen (2004), Inverse kinematic and forward dynamic models of the 2002 Denali fault earthquake, Alaska, *Bull. Seismol. Soc. Am.*, 94, S214-S233.

Ohnaka, M., and T. Yamashita (1989), A cohesive zone model for dynamic shear faulting based on experimentally inferred constitutive relation and strong motion source parameters, *J. Geophys. Res.*, 94, 4089–4104.

Ohnaka, M., and Y. Kuwahara (1990), Characteristic features of local breakdown near a crack-tip in the transition zone from nucleation to unstable rupture during stick-slip shear failure, *Tectonophysics*, 175, 197–220.

Ohnaka, M., and L. F. Shen (1999), Scaling of the shear rupture process from nucleation to dynamic propagation: Implication of geometric irregularity of the rupturing surfaces, *J. Geophys. Res.*, 104, 817–844.

Okubo, P. G. (1989), Dynamic rupture modelling with laboratory-derived constitutive relations, *J. Geophys. Res*., 94, 12, 321– 12,335.

Olsen, K. B. and R. J. Archuleta (1996), Three-dimensional simulation of earthquakes on the Los Angeles fault system, *Bull. Seismol. Soc. Am.*, 86, 575-596.

Olsen, K. B., R. Madariaga, and R. J. Archuleta (1997), Three-dimensional dynamic simulation of the 1992 Landers earthquake, *Science,* 278, 834–838.

Olson A. H. and R. J. Apsel (1982), Finite fault and inversion theory with application to 1979 Imperial Valley earthquake, *Bull. Seismol. Soc. Am.*, 72, 1969-2001.

Olson, A. H., J. A. Orcutt, and G. A. Frasier (1984), The discrete wavenumber / finite element method for synthetic seismograms, *Geophys. J. R. Astr. Soc.*, 77, 421-460.

Olson, A. H., and J. G. Anderson (1988), Implications of frequency-domain inversion of earthquake ground motions for resolving the space-time dependence of slip on an extended fault, *Geophys. J.*, 94, 443–455.

Papageorgiou, A. S., and K. Aki (1983), A specific barrier model for the quantitative description of inhomogeneous faulting and the prediction of strong-ground motion. II. Applications of the model, *Bull. Seismol. Soc. Am.*, 73, 953–978.

Peyrat, S., K. Olsen, and R. Madariaga (2001), Dynamic modeling of the Landers earthquake, *J. Geophys. Res*., 106(B11), 26,467– 26,482.

Peyrat, S., and K. B. Olsen (2004), Nonlinear dynamic rupture inversion of the 2000 Western Tottori, Japan, earthquake, *Geophys. Res. Lett.*, 31, L05604, doi:10.1029/2003GL019058.

Pe´rez-Campos, X., and G. C. Beroza (2001), An apparent mechanism dependence of radiated seismic energy, *J. Geophys. Res.* 106, 11,127–11,136.

Piatanesi, A., E. Tinti, M. Cocco, and E. Fukuyama (2004), The dependence of traction evolution on the earthquake source time function adopted in kinematic rupture models, *Geophys. Res. Lett.* 31, L04609, doi: 10.1029/2003GL019225.

Piatanesi, A., A. Cirella, P. Spudich and M. Cocco (2007), A global search inversion for earthquake kinematic rupture history: Application to the 2000 western Tottori, Japan earthquake, *J. Geophys. Res*., 112, B07314, doi:10.1029/2006JB004821.

Press, F., (1968), Earth models obtained by Monte Carlo inversion, *J. Geophys. Res*., 73, 5223-5234.

Press, F., (1970a), Earth models consistent with geophysical data, *Phys. Earth Planet. Inter.*, 3, 3-22.

Pulido, N., and K. Irikura (2000), Estimation of dynamic rupture parameters from the radiated seismic energy and apparent stress, *Geophys. Res. Lett*., 27(23), 3945–3948.

Pulido, N. and T. Kubo (2004), Near-fault strong motion complexity of the 2000 Tottori earthquake (Japan) from a broadband source asperity model, *Tectonophysics*, 390, 177-192.

Reid, H. F. (1910), *The Mechanics of the Earthquake*, Vol. 2 in *The California Earthquake of April 18, 1906*. Report of the State Investigation Commission, Carnegie Institution of Washington.

Rosakis, A. J., Samudrala O. and D. Coker (1999), Cracks faster than the shear wave speed, *Science*, 5418, 1337-1339.

Rothman, D. (1985), Nonlinear inversion statistical mechanics, and residual statics corrections, *Geophysiscs*, 50, 2784-2796.

Rothman, D. (1986), Automatic estimation of large residual statics corrections, *Geophysiscs*, 51, 332-346.

Rice, J. R., and M. Cocco, (2006), Seismic fault rheology and earthquake dynamics, Dahlem Workshop on /The Dynamics of Fault Zones/, pp.99-137, edited by M. R. Handy, MIT Press, Cambridge, Mass.

Ruiz, J. A. (2007), Modélisation d'accélérogrammes synthétiques large-bande par modélisation de la cinématique de la rupture sismique, Ph.D thesis Institut de Physique du Globe de Paris, France.

Sabetta, F., and Pugliese, A. (1996), Estimation of response spectra and simulation of non-stationary earthquake ground motion, *Bull. Seismol. Soc. Am.*, 86, 337-352.

Sagiya, T., T. Nishimura, Y. Hatanaka, E. Fukuyama and W. L. Ellsworth (2002), Crustal movements associated with the 2000 western Tottori earthquake and its fault models, *ZiSin (J. Seismol. Soc. Jpn.)* 54, 523-534 (in Japanese with English abstract).

Salichon, J., P. Lundgren, B. Delouis, and D. Giardini (2004), Slip history of the 16 October 1999 Mw 7.1 Hector Mine earthquake (California) from the inversion of InSar, GPS, and teleseismic data, *Bull. Seismol. Soc. Am.*, 94, 2015-2027.

Sambridge, M. (1999a), Geophysical inversion with a neighbourhood algorithm-I. Searching a parameter space, *Geophys. J. Int*,. 138, 479–494.

Sambridge, M. (1999b), Geophysical inversion with a neighbourhood algorithm-II. Appraising the ensemble, *Geophys. J. Int.* 138, 727-746.

Sambridge, M. (2001), Finding acceptable models in nonlinear inverse problems using a neighbourhood algorithm, *Inverse Problems*, 17, 387-403.

Sambridge, M., and Mosegaard, K. (2002), Monte Carlo Methods in Geophysical Inverse Problems, *Reviews of Geophysics*, 20, 1009, doi:10.1029/2000RG000089.

Sarao`, A., S. Das, and P. Suhadolc (1998), Effect of non-uniform station coverage on the inversion for earthquake rupture history for a Haskell type source model, *J. Seism.*, 2, 1–25.

Scherbaum, F., J. Schmedes, and F. Cotton (2004), On the conversion of source-to-site distance measured for extended source models, *Bull. Seismol. Soc. Am.*, 94, no. 3, 1053-1069.

Sekiguchi, H., K. Irikura, and T. Iwata (2000), Fault geometry at the rupture termination of the 1995 Hyogo-ken Nanbu earthquake, *Bull. Seismol. Soc. Am.*, 90, 974-1002.

Semmane, F., F. Cotton and M. Campillo (2005), The 2000 Tottori earthquake: a shallow earthquake with no surface rupture and slip properties controlled by depth, *J. Geophys. Res.*, 110, B03306, doi:10.1029/2004JB003194.

Sen, M. and Stoffa P. L. (1991), Nonlinear one-dimensional seismic waveform inversion using simulated annealing, *Geophysics*, 56,1624-1638.

Sen, M. K., B. B., Bhattacharya, and P. L. Stoffa (1993), Nonlinear inversion of resistivity sounding data, *Geophysiscs*, 58, 496-507.

Sen, M. and Stoffa P. L. (1995), *Global Optimization Methods in Geophysical Inversion*, Adv. Explor. Geophys., vol. 4, Elsevier Sci., New York.

Shakal, A., V. Graizer, M. Huang, H. Haddadi, and K. Lin (2005), Strong-motion data from the M6.0 Parkfield earthquake of September 28, 2004, *Proceedings of SMIP05 Seminar on Utilization of Strong Motion Data, Los Angeles, CA*, 1-18.

Shibutani, T., M. Sambridge and B. Kennett (1996), Genetic algorithm inversion for receiver functions with application to crust and uppermost mantle structure beneath Eastern Australia, *Geophys. Res. Lett.*, 23(14), 1829-1832.

Shibutani, T., S. Nakao, R. Nishida, F. Takeuchi, K. Watanabe, and Y. Umeda, (2002), Swarm-like seismic activity in 1989, 1990 and 1997 preceding the 2000 western Tottori earthquake, *Earth Planets Space*, 54, 831–845.

Simons, M., Y. Fialko, and L. Rivera (2002), Coseismic deformation from the 1999, Mw_7.1, Hector Mine earthquake as inferred from InSAR and GPS observations, *Bull. Seismol. Soc. Am.*, Special issue on Hector Mine earthquake, 92, no. 4, 1390–1402.

Singh, S. K., and M. Ordaz (1994), Seismic energy release in Mexican subduction zone earthquakes, *Bull. Seismol. Soc. Am.*, 84, 1533–1550.

Sørensen, B., M., Pulido, N., and Atakan, K. (2007), Sensitivity of ground-motion simulations to earthquake source parameters: A case study for Istanbul, Turkey, *Bull. Seismol. Soc. Am.*, 97, no. 3, 881–900, doi: 10.1785/0120060044.

Somerville, P. G., N. F. Smith, R. W. Graves, and N. A. Abrahamson (1997), Modification of empirical strong ground motion attenuation relations to include the amplitude and duration effects of rupture directivity, *Seism. Res. Lett.*, 68, 199–222.

Somerville, P., Irikura, K. Graves, R. Sawada, S. Wald, D. Abrahamson, N. Iwasaki, Kagawa,Y., T. Smith, N. Kowada, A. (1999), Characterizing crustal earthquake slip models for the prediction of strong ground motion, *Seism. Res. Lett.*, 70, 1, 59-80.

Song, S. and Beroza, G. (2004), A simple dynamic model for the 1995 Kobe, Japan earthquake, *Geophys. Res. Lett.*, 31(18),: doi: 10.1029/2004GL020557, issn: 0094-8276.

Spudich, P. (1980), The DeHoop-Knopoff representation theorem as a linear inversion problem, *Geophys. Res. Lett.*, 9, 717-720.

Spudich, P., and Frazer, L. N. (1984), Use of ray theory to calculate high-frequency radiation from earthquake sources having spatially variable rupture velocity and stress drop, *Bull. Seismol. Soc. Am.*, 74, 2061-2082.

Spudich, P., and Archuleta, R. (1987), Techniques for earthquake ground motion calculation with applications to source parameterization of finite faults, in Bolt, B.A. ed., SEISMIC STRONG MOTION SYNTHETICS: Orlando, Florida, Academic Press, p.205-265.

Spudich, P., and D. P. Miller (1990), Seismic site effects and the spatial interpolation of earthquake seismograms: Results using aftershocks of the 1986 North Palm Springs, California, earthquake, *Bull. Seismol. Soc. Am.*, 80(6), 1504-1532.

Spudich, P. and L. Xu (2003), Software for calculating earthquake ground motions from finite faults in vertically varying media, in *International Handbook of Earthquake and Engineering Seismology*, Academic Press.

Spudich, P., and M. Guatteri (2004), The effect of bandwidth limitations on the inference of earthquake slip-weakening distance from seismograms, *Bull. Seismol. Soc. Am.*, 94, 2028–2036.

Spudich, P., and Chiou, B.S-J., (2008), Directivity in NGA earthquake ground motions: Analysis using isochrone theory, accepted, *Earthquake Spectra*.

Steidl, J. H., R. J. Archuleta, and S. H. Hartzell (1991), Rupture history of the 1989 Loma Prieta, California, earthquake, *Bull. Seismol. Soc. Am.*, 81, 1573–1602.

Sugiyama, Y. (2007), 16 July 2007 Niigata-ken Chuetsu-Oki earthquake; its characteristics, tectonic background and significance for active fault evaluation, 2007 AGU Fall Meeting, San Francisco, *T31G-01* abstract.

Tarantola, A. (1987), *Inverse Problem Theory*, Elsevier Sci., New York.

Taylor S. L., M. E. Payton and W. R. Raun (1999), Relationship between mean, coefficient of variation, mean square error and plot size in wheat field experiments. *Contribution from the Okla.* Agric. Exp. Sta., Department of Plant and Soil Sciences, 044 North Agricultural Hall, and Department of Statistics, 301 Math Sciences, Oklahoma State University, Stillwater, OK 74078.

Thio, H. K., R. W. Graves, P. G. Somerville, T. Sato, and T. Ishii (2004), A multiple time window rupture model for the 1999 Chi-Chi earthquake from a combined inversion of teleseismic, surface wave, strong motion, and GPS data, *J. Geophys. Res.*, 109, B08309, doi:10.1029/2002JB002381.

Tinti, E., E. Fukuyama, A. Piatanesi and M. Cocco (2005a), A kinematic source time function compatible with earthquake dynamics, *Bull. Seismol. Soc. Am.*, 95(4), 1211-1223, doi:10.1785/0120040177.

Tinti, E., P. Spudich and M. Cocco (2005b), Earthquake fracture energy inferred from kinematic rupture models on extended faults, *J. Geophys. Res.*, 110, B12303, doi:10.1029/2005JB003644.

Toda S. (2007), Mw=6.6 Niigata Chuetsu-Oki earthquake ruptured on a fault strongly unclamped by the 2004 Mw=6.6 Niigata Chuetsu shock, *Eos, Trans. AGU 87*(52), Fall Meet. Suppl., Abstract S13B-1031.

Trifunac, M. D. (1974), A three-dimensional dislocation model for the San Fernando, California, earthquake of February 9, 1971, *Bull. Seismol. Soc. Am.,* 64, 149–172.

Tsukahara, H., and Y. Kobayashi (1991), Crustal stress in the central and western parts of Honshu, Japan. *Zisin,* 44, 221–231 (in Japanese with English abstract).

Uhrhammer, R. A. and B. A. Bolt (1991), The seismic magnitude of the 1989 Loma Prieta mainshock determined from strong motion records, *Bull. Seismol. Soc. Am.*, 81, 1511-1517.

Vasco, D. W., L. R. Johnson, and E. L. Majer (1993), Ensemble inference in geophysical inverse problems, *Geophys. J. Int.*, 117, 711-728.

Venkataraman, A., L. Rivera, and H. Kanamori (2002), Radiated energy from the 16 October 1999 Hector Mine earthquake: regional and teleseismic estimates, *Bull. Seismol. Soc. Am.*, 92, 1256–1265.

Venkataraman, A. and Kanamori, H. (2004), Effect of directivity on estimates of radiated seismic energy, *J. Geophys. Res.*, 109, B04301.

Ventsel., E. S. (1983), *Teoria delle Probabilità*. Edizioni Mir, Mosca.

Wald, D. J., D. V. Helmberger and S. H. Hartzell (1990), Rupture process of the 1987 Superstition Hills earthquake from the inversion of strong motion data, *Bull. Seismol. Soc. Am.*, 80, 1079-1098.

Wald, D. J., D. V. Helmberger, and T. H. Heaton (1991), Rupture model of the 1989 Loma Prieta earthquake from the inversion of strong motion and broadband teleseismic data, *Bull. Seismol. Soc. Am.*, 81, 1540–1572.

Wald, D. J. and T. H. Heaton (1994), Spatial and temporal distribution of slip for the 1992 Landers, California earthquake, *Bull. Seismol. Soc. Am.*, 84, 668-691.

Wald, D. J., and Sommerville, P. G.(1995), Variable-slip rupture model of the Great 1923 Kanto, Japan Earthquake: Geodetic and body-waveform analysis, *Bull. Seismol. Soc. Am.*, 85, 159–177.

Wald, D. J., T. H. Heaton, and K. W. Hudnut (1996), The slip history of the 1994 Northridge, California earthquake determined from strong motion, teleseismic, GPS, and leveling data, *Bull. Seismol. Soc. Am.*, 86, 49–70.

Wald, D. J. and R. W. Graves (2001), Resolution analysis of finite source inversion using one- and three-dimensional Green's functions: 2. Combining seismic and geodetic data, *J. Geophys. Res.*, 106(B5), 8767-8788.

Wessel, P. and W. H. F. Smith (1998), New, improved version of the Generic Mapping Tools released, *EOS Trans. AGU*, 79, 579.

Winslow, N. W., and L. J. Ruff (1999), A hybrid method for calculating the radiated wave energy of deep earthquakes, *Phys. Earth Planet. Inter*., 116, 181– 190.

Wyss, M., and J. Brune (1971), Regional variations of source properties in southern California estimated from the ratio of short- to long-period amplitudes, *Bull. Seismol. Soc. Am.*, 61, 1153–1168.

Yagi, Y., and M. Kikuchi (2000), Source rupture process of the Kocaeli, Turkey, earthquake of August 17, 1999, obtained by joint inversion of near-field data and teleseismic data, *Geophys. Res. Lett.*, 27, 1969–1972.

Yasuda, T., Y. Yagi, T. Mikumo, and T. Miyatake (2005), A comparison between *D*c_-values obtained from a dynamic rupture model and waveform inversion, *Geophys. Res. Lett.*, 32, L14316, doi 10.1029/2005GRL023114.

Yoffe, E. (1951), The moving Griffith crack, *Phil. Mag.*, 42, 739–750.

Yoshida, S., K. Koketsu, B. Shibazaki, T. Sagiya, T. Kato, and Y. Yoshida (1996), Joint inversion of near- and far-field waveforms and geodetic data for the rupture process of the 1995 Kobe earthquake, *J. Phys.Earth*, 44, 437–454.

Zeng, Y., and J. G. Anderson (1996), A composite source model of the 1994 Northridge earthquake using genetic algorithms, *Bull. Seismol. Soc. Am.*, 86, S71–S83.

Zeng, Y., and C. H. Chen (2001), Fault rupture process of the 20 September 1999 Chi-Chi, Taiwan, earthquake, *Bull. Seismol. Soc. Am.*, 91, 1088-1098.

Zhang, W., T. Iwata, K. Irikura, H. Sekiguchi, and M. Bouchon (2003), Heterogeneous distribution of the dynamic source parameters of the 1999 Chi-Chi, Taiwan, earthquake, *J. Geophys. Res*., 108(B5), 2232, doi:10.1029/2002JB001889.

Zhou S., K. Irikura, and X. Chen (2004), Analysis of the reliability and resolution of the earthquake source history inferred from waveforms, taking the Chi-chi earthquake as an example, *Geophys. J. Int.*, 157, 1217-1232.